University of Illinois at Urbana-Champaign

ACRC

Air Conditioning and Refrigeration Center A National Science Foundation/University Cooperative Research Center

Investigation of Adiabatic Refrigerant Pressure Drop and Flow Visualization in Flat Plate Evaporators

E. W. Jassim, T. A. Newell, and J. C. Chato

ACRC TR-187 July 2001

For additional information:

Air Conditioning and Refrigeration Center
University of Illinois
Mechanical & Industrial Engineering Dept.
1206 West Green Street
Urbana, IL 61801

(217) 333-3115

Prepared as part of ACRC Project #120
Investigation of Refrigerant/Oil Mixtures in Horizontal Tubes and Flat Plate Condensers and Evaporators
T. A. Newell, and J. C. Chato, Principal Investigators

The Air Conditioning and Refrigeration Center was founded in 1988 with a grant from the estate of Richard W. Kritzer, the founder of Peerless of America Inc. A State of Illinois Technology Challenge Grant helped build the laboratory facilities. The ACRC receives continuing support from the Richard W. Kritzer Endowment and the National Science Foundation. The following organizations have also become sponsors of the Center.

Amana Refrigeration, Inc.
Arçelik A. S.
Brazeway, Inc.
Carrier Corporation
Copeland Corporation
Dacor
Daikin Industries, Ltd.
DaimlerChrysler Corporation
Delphi Harrison Thermal Systems
Frigidaire Company
General Electric Company
General Motors Corporation
Hill PHOENIX
Honeywell, Inc.
Hussmann Corporation
Hydro Aluminum Adrian, Inc.
Indiana Tube Corporation
Invensys Climate Controls
Kelon Electrical Holdings Co., Ltd.
Lennox International, Inc.
LG Electronics, Inc.
Modine Manufacturing Co.
Parker Hannifin Corporation
Peerless of America, Inc.
Samsung Electronics Co., Ltd.
Tecumseh Products Company
The Trane Company
Thermo King Corporation
Valeo, Inc.
Visteon Automotive Systems
Wolverine Tube, Inc.
York International, Inc.

For additional information:

Air Conditioning & Refrigeration Center
Mechanical & Industrial Engineering Dept.
University of Illinois
1206 West Green Street
Urbana, IL 61801

217 333 3115

Abstract

Adiabatic pressure drop and flow visualization in chevron plate, 1:1 aspect ratio bumpy plate, and 2:1 aspect ratio bumpy plate heat exchangers were investigated for vertical upward flow with R134a. Qualities ranging from sub-cooled liquid to superheated vapor were investigated. Mass fluxes ranged from 16 kg/m^2-s (for superheated vapor) to approximately 300 kg/m^2-s (for sub-cooled liquid). The pressure drop experiments were conducted for 10^o C and 20^o C inlet temperatures. The flow visualization experiments were conducted at a 10^o C inlet temperature.

The following is the order of highest to lowest pressure drop geometries on both a mass flux and mass flow bases: chevron plate, 1:1 aspect ratio bumpy plate, and 2:1 aspect ratio bumpy plate. These trends are more pronounced on a mass flow basis.

Four flow regimes were observed for the flat plate geometries investigated and are mapped out on a mass flux versus quality basis for each geometry. The chevron geometry was seen to undergo flow transitions at lower qualities and mass fluxes than the bumpy plate geometries.

The kinetic energy per unit volume of the flow was found to have a strong linear relationship with pressure drop for both single-phase and two-phase flow, suggesting that inertial effects are the dominant mode of pressure drop in flat plate heat exchangers. Vapor pressure drop prediction models based on the kinetic energy of the flow are presented, which predict pressure drop within 20%. A two-phase pressure drop model is developed, also based on kinetic energy per unit volume of the flow. A pseudo void fraction is defined in order to correlate the two-phase pressure drop to the single-phase pressure drop. The two-phase pressure drop model predicts two-phase pressure drop to within 15% of experimental measurements.

A description of and modifications to the experimental test facilities are provided. In addition, the geometries and construction of the plates are provided.

Table of Contents

List of Figures

Page

List of Tables

Nomenclature

A_m	Mean Cross Sectional Area (m^2)
A_o	Cross - Sectional Open Area of Channel (m^2)
A_w	Wetted Area of Test Section, Excluding the Headers (m^2)
A_{wc}	Wetted Area of Channel and Fin Walls, Excluding Fin Ends (m^2)
C	Arbitrary Constant
D_h	Hydrolic Diameter (m)
dP/dx	Pressure Differential Per Unit Length (kPa/m)
f	Friction Factor
G	Mass Flux (kg/m^2 - s)
g	Gravitational Acceleration (9.81 m/s^2)
h	Vertical Distance Between Test Section Pressure Taps (m)
KE	Kinetic Energy (J)
L	Test Section Length, Excluding the Headers (m)
m	Slope of Curve x 1000
$\dot{m}$	Mass Flow Rate (kg/s)
n	Number of Integration Points
P	Pressure (kPa)
Pc	Chevron Pitch (mm)
R	Ideal Gas Constant for R134a (81.5 J/kgK)
Re	Reynolds Number
S	Slip Ratio, Velocity of Vapor/Velocity of Liquid
T	Temperature (^oC)
U	Wetted Perimeter That Bounds A_m (m)
v	Velocity (m/s)
V_{ts}	Volume of Test Section Excluding the Headers (m^3)
x	Quality
X_{tt}	Lockhart - Martinelli Parameter

Greek Symbols

a	Void Fraction
ß	Pseudo Void Fraction/ Homogenous Void Fraction
ßc	Chevron Angle From Flow Direction (^{o})
$?P$	Pressure Drop (kPa)
$?x$	Integration Length (m)
$?$	Density (kg/m^3)
μ	Viscosity (kPa - s)
F	Two - Phase Multiplier

Subscripts

a	Accelerational
D	Darcy
f	Fanning
fi	Frictional and Inertial
g	Gravitatio nal
i	Test Section Inlet
l	Liquid
p	Pseudo
sp	Single - Phase
tp	Two - Phase
hom	Homogenous
v	Vapor

Chapter 1: Introduction

Flat plate heat exchangers have been in commercial use since 1923 according to Raju and Chand (1981). They are widely used in the liquid-to-liquid configuration for food processing, dairy, and other industrial applications. Their compact size presents a clear advantage over shell and tube style heat exchangers in some applications. Since the single-phase flow configuration in flat plate heat exchangers has been used for a long period of time, there is a lot of single-phase flat plate literature available. Currently, flat plate heat exchangers are being used in two-phase configurations for applications such as automotive evaporators, oil coolers, and other industrial applications. Chevron-style flat plate heat exchangers are used for industrial refrigeration while bumpy-style flat plate heat exchangers are commonly used for automotive air conditioners. There is limited information in the literature about two-phase flow in flat plate heat exchangers, especially with new refrigerants such as R134a. Furthermore, the relationship between "chevron" and "bumpy" style flat plate heat exchangers have yet to be identified in literature.

This report will focus on the pressure drop and flow visualization of R134a in "chevron" style and two types of "bumpy" style flat plate evaporators: a 1:1 aspect ratio bumpy plate and a 2:1 aspect ratio bumpy plate. Flat plate heat exchangers generally consist of complex passageways for the two-phase refrigerant flow. Chevron flat plate heat exchangers consist of passageways that have limited groove-to-groove access while bumpy plate heat exchangers have a more direct connection across groove (bump) rows. The 2:1 aspect ratio bumpy plate has less of a direct connection across groove (bump) rows than the 1:1 aspect ratio plate geometry. Consequently, the 2:1 aspect ratio bumpy plate represents an intermediate step between the chevron and 1:1 aspect ratio geometries. The three plate designs investigated in this paper, perhaps, do not exactly resemble any particular geometry found in industry. The rationale behind the plate designs was to provide a means of comparing chevron plates to dimpled plates. The comparison is done on a pressure drop basis and through flow visualization experiments. Furthermore, analysis of fundamental parameters, such as kinetic energy of the flow fields, can help identify similarities and differences among the plate designs, and provide a method to predict pressure drop in flat plates.

A summary of the available pressure drop and flow visualization literature and background for single and two-phase flow in flat plates is presented in Chapter 2 of this paper. The description and modifications of the experimental test facilities can be found in Chapter 3. Chapter 4 describes the test section geometries and construction. Chapter 5 presents experimental single and two-phase pressure drop data obtained for the three flat plate geometries.

The flow visualization techniques and observations are discussed in Chapter 6. Chapter 7 investigates methods of predicting pressure drop in flat plates. The results of the study and suggestions for future work are summarized in Chapter 8.

Chapter 2: Literature Review

This chapter summarizes the pressure drop information available for single-phase and two-phase flow in flat plate heat exchangers. In addition, it discusses three types of void fraction models.

2.1 Single-Phase Flat Plate Pressure Drop Literature

There is a large amount of single-phase literature for flat plate heat exchangers mainly because flat plate heat exchangers have been in commercial use in the single-phase configuration since 1923. Moreover, the majority of the single-phase literature observed for flat plates specifically discuss single-phase liquid flow. The pressure drop in flat plates is composed of the sum of the pressure drop due to viscous and inertial effects, gravitational effects, and accelerational effects. The expression for total pressure drop is given in equation 2.1.

$$\Delta P = \Delta P_{fi} + \Delta P_a + \Delta P_g \tag{2.1}$$

All of the single-phase flat plate pressure drop papers found use Reynolds number and friction factor correlations to characterize the frictional and inertial pressure drop. The following references use Reynolds number and friction factor correlations to characterize single-phase flow in flat plate heat exchangers: Muley and Manglik (1999), Wang et al. (1999), Manglik (1996), Talik et al. (1995), Thonon et al. (1995), Shah and Focke (1988), Luo and Yu (1988), Mandrusiak and Carey (1988), Luo and Zhang (1986), Raju and Bansal (1981). All of the aforementioned papers use chevron style heat exchangers except Mandrusiak and Carey (1988), who studied a channel with offset strip fins. Furthermore, all of the aforementioned sources report friction factors that are orders of magnitude higher that friction factors commonly found in round tubes, with the exception of Mandrusiak and Carey who used a low pressure drop geometry. The only paper found using single-phase vapor was Wang et al. (1999), where they investigated superheated steam pressure drop in chevron plates.

Although, all of the single-phase papers used the friction factor versus Reynolds number to characterize the pressure drop in the flat plates, the definition of these quantities differed. Some of the papers such as Wang et al. (1999), Luo and Yu (1988), and Luo and Zhang (1986) utilize the Darcy friction factor which is defined in equation 2.2.

$$f_D = 2D_h \rho \frac{(\Delta P - \rho g h)}{LG^2} \tag{2.2}$$

Other papers utilize the Fanning friction factor such as Muley and Manglik (1999), and Mandrusiak and Carey (1988), which differs by a factor of 4 and is expressed in equation 2.3.

$$f_f = D_h \rho \frac{(\Delta P - \rho g h)}{2LG^2} \tag{2.3}$$

All of the papers investigated agree on the definition of the Reynolds number as given in equation 2.4.

$$\mathrm{Re} = \frac{GD_h}{\mu} \tag{2.4}$$

The papers define the mass flux as the mass flow rate divided by the mean cross sectional area as seen in equation 2.5.

$$G = \frac{\dot{m}}{A_m} \tag{2.5}$$

The papers, however, differ in their definition of the hydraulic diameter. Muley and Manglik (1999), and Wang et al. (1999) define the hydraulic diameter as twice the plate groove depth. Whereas, Luo and Yu (1988) and Luo and Zhang (1986) define the hydraulic diameter as 4 times the mean cross sectional area divided by the wetted perimeter that bounds the mean cross sectional area as shown equation 2.6.

$$D_h = \frac{4A_m}{U} \tag{2.6}$$

Mandrusiak and Carey (1988) define the hydraulic diameter according to equation 2.7.

$$D_h = \frac{4A_o L}{A_{wc}} \tag{2.7}$$

Luo and Yu (1988) and Luo and Zhang (1986) used chevron geometry heat exchangers similar to the chevron geometry tested in this thesis. They both used a 60^o C chevron angle, which is the angle between the corrugated channel and the flow direction. The geometry of Luo and Yu (1988) differed slightly from that of Luo and Zhang (1986). Luo and Yu (1988) rounded the tops of the grooves where the plates come in contact, and found that this resulted in a significant pressure drop reduction. The friction factor curve fits for Luo and Yu (1988) and Luo and Zhang (1986) are given in equations 2.8 and 2.9, respectively.

$$f = 5.94\,\mathrm{Re}^{-0.062} \tag{2.8}$$

$$f = 7.70\,\mathrm{Re}^{-0.067} \tag{2.9}$$

2.2 Two-Phase Flat Plate Pressure Drop and Flow Visualization Literature

Until recently, flat plates were primarily used for single-phase flow. Flat plate heat exchangers have recently been used for two-phase flow applications. Consequently, there is not a significant amount of two-phase literature available. Wang et al. (1999), Yan and Lin (1999), Yan et al. (1999), Thonon et al. (1995), and Mandrusiak and Carey (1988) all present two-phase pressure drop data for flat plate heat exchangers. All of the geometries investigated are chevron style heat exchangers except for Mandrusiak and Carey (1988) who investigated two-phase R113 pressure drop in a channel with offset strip fins. Wang et al. (1999) investigate steam condensation in chevron heat exchangers. Yan and Lin (1999) and Yan et al. (1999) investigated R134a evaporation and condensation, respectively, in chevron style heat exchangers. Thonon et al. (1995) investigated two–phase pressure drop of R22 in condensation and evaporation in chevron style heat exchangers.

2.2.1 Two-Phase Pressure Drop in Flat Plates

The two-phase pressure drop in flat plates, like the single-phase pressure drop, is composed of the sum of the pressure drop due to viscous and inertial effects, gravitational effects, and accelerational effects. The expression for total pressure drop is given in equation 2.1. The accelerational effects in two-phase flow under evaporation and condensation were found to be very small according to Yan and Lin (1999) and Yan et al. (1999), respectively. The accelerational and gravitational effects accounted for 1 to 4% of the total pressure drop.

All of the two-phase pressure drop papers investigated predict the two-phase pressure drop differently. Wang et al. (1999), Thonon et al. (1995), Mandrusiak and Carey (1988) all utilize the Lockhart-Martinelli parameter (1949) to predict pressure drop. The expression for the Lockhart-Martinelli parameter (X_{tt}) used in Thonon et al. (1995) is given in equation 2.10.

$$X_{tt} = \left(\frac{1-x}{x}\right)^{0.9}\left(\frac{r_v}{r_l}\right)^{0.5}\left(\frac{m_l}{m_v}\right)^{0.1} \tag{2.10}$$

Wang et al. (1999) and Mandrusiak and Carey (1988) define the Lockhart-Martinelli parameter according to equation 2.11.

$$X_{tt}^2 = \frac{\Delta P_l}{\Delta P_v} = \frac{f_l \frac{L}{D_h}\frac{G^2(1-x)^2}{2r_l}}{f_v \frac{L}{D_h}\frac{G^2 x^2}{2r_v}} \tag{2.11}$$

Thonon et al. (1995) also utilized the Chisholm correlation, a two-phase multiplier, to predict pressure drop with a value of C equal to 8. The Chisholm correlation is given in equation 2.12.

$$\Phi_l^2 = \frac{\Delta P_{tp}}{\Delta P_l} = 1 + \frac{C}{X_{tt}} + \frac{1}{X_{tt}^2} \tag{2.12}$$

Wang et al. (1999) used the Chisholm correlation given in equation 2.12 with a C value of 16 to predict the pressure drop. Mandrusiak and Carey (1988) use the Chisholm correlation given in equation 2.12 with a C value of 12 for laminar flow and 20 for turbulent flow to predict the pressure drop.

Yan and Lin (1999) and Yan et al. (1999) utilize a homogenous model to predict two-phase flat plate pressure drop. The homogenous void fraction model assumes that the two-phase flow is a homogenous mixture where the liquid and vapor phases are traveling at the same velocity. The homogenous void fraction is found using equation 2.13.

$$a = \frac{1}{1 + \left(\frac{1-x}{x}\right)\left(\frac{r_v}{r_l}\right)} \tag{2.13}$$

The homogenous density is then computed using equation 2.14.

$$r = (1-a)r_l + a\,r_v \tag{2.14}$$

The two-phase pressure drop is then obtained from equation 2.15.

$$f_{tp} = \frac{\Delta P D_h r}{2G^2 L} \tag{2.15}$$

2.2.2 Additional Void Fraction Models

Void fraction models have often been developed with the Lockhart-Martinelli parameter. The Wallis (1969) void fraction model was developed for round tubes and utilizes the void fraction given in equation 2.16.

$$a = (1 + X_{tt}^{0.80})^{-0.378} \tag{2.16}$$

Mandrusiak and Carey (1988) found that the Wallis void fraction model over-predicted the experimental void fraction measurements. Consequently, they developed their own void fraction model from their experimentally determined void fraction measurements and is given in equation 2.17.

$$a = (1 + 0.25 X_{tt})^{-2.0} \tag{2.17}$$

2.2.3 Two-Phase Flow Visualization

There are very few sources with flow visualization information on flat plate heat exchangers with refrigerant. Mandrusiak and Carey (1988) preformed flow visualization experiments on a vertical channel with offset strip fins with R113. Three different flow regimes were observed: bubbly-slug flow, churn flow, and annular flow. The bubbly-slug flow was found to occur at low qualities (around 6%). Churn flow occurred at qualities around 16% where the refrigerant periodically surges upward and then falls down due to gravity. Annular flow, defined as a liquid boundary layer covering all surfaces, occurred at higher qualities (around 40%).

2.2.4 Flat Plate Heat Exchanger Orientation

The optimal plate heat exchanger inclination for evaporation and condensation have been investigated by Kedzierski (1997). He found that the optimal inclination for evaporative heat transfer in flat plates was the vertical upward flow configuration. Gravity induces stratified flow in the horizontal flow configuration, which decreases the heat transfer. If the evaporator was horizontal, it was found to have 60-75% of the vertical position heat transfer. For condensation, however, it was found that the horizontal position was the optimal position for heat transfer. The condensate film thickness becomes thinner in the horizontal flow configuration, which increases the heat transfer. The horizontal position provided heat transfer 17-30% higher than the vertical downward flow configuration.

Chapter 3: Evaporator Test Loop Development and Operation

The evaporator test loop, which was completed in the Spring of 2000, required numerous modifications in order to improve the loop and allow for the testing of flat plate evaporators. This chapter details how the loop design was modified in order to allow proper functioning and increase the loop's thermal response, the calibration of instruments in the loop, and the methods for proper operation of the test loop. Details of the loop before modification are presented in the thesis of Tran (2000).

3.1 Evaporator Test Loop Modifications

A few obstacles were encountered with implementation of the new loop design. In the new loop, the liquid pump and the compressor draw refrigerant from the same receiver tank. Subsequently, the suction head of the refrigerant pump was too low to allow liquid flow without causing pump cavitation. This problem was solved by adding a sub-cooler at the inlet of the pump (see Figure 3.1). The heat exchanger used to sub-cool the liquid is a 1.25 ton unit (Alpha Laval CB14-28H S02), measuring 20.7 x 7.7 x 7.2 cm. This heat exchanger is operated in a refrigerant to refrigerant configuration. A 1 ton compressor operates a R22 chiller which sub-cools the refrigerant in the test loop. A schematic of the sub-cooler chiller system is depicted in Figure 3.2. The sub-cooler loop utilizes building chilled water to condense the refrigerant in a shell and tube style 1.25 ton condenser (Standard Refrigeration Company TNT150). This sub-cooling loop has the ability to rapidly modulate temperature and capacity. A needle valve is utilized to expand the refrigerant at the inlet of the sub-cooler so that the capacity and evaporation temperature can be modulated. Additional control over the R22 chiller loop temperature is obtained by modulating the needle valve on the chilled water loop. Furthermore, a hot gas bypass with a needle valve is utilized between the entrance and the exit of the compressor so that the capacity can be modulated by changing the aperture of the needle valve.

The condenser after the test section, currently used for the sub-cooler, was replaced by a 3¼ ton Alfa Laval (CB26-44H C29) brazed plate heat exchanger. The previous condenser and compressor vapor cooler operated from a glycol loop, which utilized a 1.5 ton R22 compressor. This glycol loop had a large thermal mass associated with it. Consequently, it took a long time to bring the loop to steady state temperatures and it was difficult to modulate the loop capacity in a timely manner. As a result, the condenser was changed to a refrigerant-to-refrigerant configuration identical to the configuration implemented for the sub-cooler (see Figure 3.2). This change allowed for rapid loop temperature and capacity modulation. It should be noted that the nominal capacity of both the sub-cooler and the condenser heat exchangers exceed the demands of the loop because they are operated in an atypical configuration. The refrigerant flow is downward for both of the refrigerant streams in each heat exchanger so that there is no excessive oil holdup. In order to allow for proper heat transfer for this configuration, heat exchangers with large capacities were used.

The vapor cooler at the exit of the compressor was also switched from utilizing the glycol loop to using chilled water. This allows for greater control of cooling temperatures so that the vapor does not condense. In addition, the capacity of the R22 compressors is not used since the cooling is derived from the chilled water.

3.2 Test Loop Calibration

This section describes the additional calibration of instruments that was required to ensure accurate results. Some of the pressure transducers and all of the thermocouples were re-calibrated because of observed discrepancies in their readings. In addition, the power transducer calibrations were checked.

3.2.1 Pressure Transducers

The pressure transducer used at the test section inlet (Omega PX215-300AI) was calibrated by determining the output current at atmospheric pressure and at the saturation pressures of different refrigerants.

The Sensotec (Z/1309-12-01) differential pressure transducer was calibrated using a water manometer. The pressure drop measurements have a $\pm$ 0.09 kPa error associated with them. In addition, the range of linearity was tested and found to be very linear up to 70 kPa, with a measured R^2 value of 0.9996.

3.2.2 Thermocouples

The thermocouples in the loop were all checked against a reference temperature. All of the thermocouples were placed in an agitated ice bath and measured within $\pm 0.35^{o}$ C of the actual temperature (0^{o} C). Calibration factors, the difference between the actual and measured temperatures, were added to the output of each thermocouple so that the thermocouples read within $\pm$ 0.1^{o} C of the actual temperature. The accuracy of the thermocouples was then checked again by measuring the 2-phase temperature of the refrigerant in the loop that had been standing at room temperature (22^{o} C) for 24 hrs. All of the temperature readings were again found to be within $\pm 0.1^{o}$ C.

3.2.3 Power Transducers

The calibrations of the pre-heater watt transducers were checked by performing an energy balance on sub-cooled liquid refrigerant. The power measured by the watt transducers was compared with specific heat times the temperature difference across times the mass flow rate though the pre-heater section, and was found to agree within $\pm$2.5%.

3.2.4 Summary of Measurement Uncertainties

The uncertainties of temperature, differential pressure, and absolute pressure measurements are summarized in Table 3.1.

Table 3.1 Temperature and Pressure Uncertainties

Measurement	Uncertainty
All Temperatures	0.1^{o} C
Differential Pressure	0.09 kPa
Test Section Inlet Pressure	5.2 kPa
Compressor Discharge Pressure	13.8 kPa
Pre-heater Inlet Pressure	15.5 kPa

The liquid mass flow rate uncertainty associated with the liquid mass flow meter is calculated using equation 3.1.

$$\%\text{Uncertainty} = \pm\frac{3.78 * 10^{-5}\, kg/s}{\text{MassFlow Rate}} * 100 \pm .15 \qquad (3.1)$$

The vapor mass flow rate uncertainty associated with the vapor mass flow meter is calculated using equation 3.2.

$$\%\text{Uncertainty} = \pm\frac{1.51*10^{-5}\,kg/s}{\text{Mass Flow Rate}}*100 \pm .5 \qquad (3.2)$$

The uncertainty of inlet quality varied. The uncertainty of the inlet quality was found to be minimum at a quality of 0.9 (±1.0%) and maximum at a quality of 0.1 (±5.2%). The quality drops from inlet to exit by a maximum of 0.02 for the highest pressure drop ranges.

3.3 Evaporator Test Loop Operation Procedures

This section details the evaporator test loop operating procedures including: sub-cooler and condenser chiller loop operation, test loop charging, test loop startup, test section temperature modulation, and control of test section flow rate and quality.

3.3.1 Sub-cooler and Condenser Chiller Loop Operation

The refrigerant test loop's sub-cooler and condenser R22 chiller loops are identical in operation (see Figure 3.2). The chilled water supply and return valves to the chiller loop condenser must be opened during operation. The chilled water flow rate is adjusted with a needle valve on the return line. Consequently, chiller condensation temperature can be adjusted with this valve. The needle valve on the hot gas compressor bypass is used to modulate the capacity of the chiller system. The needle valve on the inlet of the chiller evaporator is used to modulate the evaporation temperature. An on/off toggle switch is used to turn on the compressor once all of the valves are at their appropriate positions.

3.3.2 Test Loop Charging

The loop requires approximately 5.5 kg of R134a for proper operation. The charge is added to the refrigerant test loop through a Schrader valve (after the loop is evacuated) by operating the sub-cooler chiller loop so that it brings the temperature of the chiller evaporator well below room temperature.

3.3.3 Test Loop Startup

When the loop has been standing at room temperature for a period of time, the refrigerant leaves the receiver tank and wanders through the loop seeking the location with the lowest temperature. The sub-cooler chiller must be used in order to move the refrigerant in the loop back to the receiver tank. All of the valves in the loop should be opened so that all of the liquid refrigerant can flow back to the receiver tank. After approximately 2 minutes the needle valve on the exit line of the compressor should be closed to prevent liquid refrigerant from entering. Next, the refrigerant pump is turned on in order to achieve liquid flow. Liquid is sent through the loop with the refrigerant pump and the liquid temperature is regulated with the sub-cooler chiller. The loop temperature should be brought to approximately 5^{o} to 10^{o} C below the desired test saturation temperature for two-phase tests. Once this is achieved, the test loop compressor bypass valve is opened approximately 3 turns, and all other valves entering and leaving the compressor should be open except the needle valve on the exit line of the compressor. The compressor is turned on and the needle valve on the exit line of the compressor is opened a few turns to allow mixing of the vapor and liquid

streams. The chilled water needle valve to the vapor cooler is opened after the compressor has run for a few minutes. For single-phase tests, the compressor is not turned on.

3.3.4 Test Section Temperature Modulation

The test section temperature is controlled by the two chiller loops and the chilled water loop entering the vapor cooler. The liquid temperature at the inlet of the refrigerant pump should always be maintained by the chiller loops at a temperature below the test section temperature for two-phase tests in order to avoid pump cavitation. The vapor comes out of the compressor as super heated vapor, which must be cooled down by the vapor cooler. The vapor temperature before mixing with the liquid, in two-phase tests, should be maintained at a temperature above the temperature of the test section so that the vapor refrigerant does not condense in the vapor cooler. If the chilled water flow rate to the vapor cooler is too high, the vapor will condense in the vapor cooler, and the refrigerant in the loop will migrate to the damping tank at the exit of the compressor. Consequently, the liquid pump will not have enough refrigerant to operate. It should be noted that for the flat plate testing analyzed in this thesis, the test loop condenser chiller was not used because the capacity of the sub-cooler chiller was sufficient. It should also be noted that for single-phase vapor tests, refrigerant can migrate to the damping tank on the exit of the compressor because liquid flow is not required. Dry ice was placed on top of the tank in order to obtain a 10^{o} C test section inlet temperature for single-phase vapor flow since the chilled water temperature is not low enough.

3.4 Control of Test Section Flow Rate and Quality

The test section flow rate and quality is adjusted by varying the mass flow rates of the vapor and liquid streams. The mass flow rate of the vapor stream is controlled by varying the aperture of the needle valve on the exit line of the compressor. It should be noted that the aperture of this needle valve is also modulated in order to dampen pressure oscillations of the compressor. The mass flow rate can also be modulated by varying the aperture of the needle valve on the compressor bypass line. Increasing the aperture of the needle valve decreases the vapor mass flow rate. The liquid mass flow rate is adjusted by varying the pump controller dial. The test section quality is controlled by varying the flow rates of the vapor and liquid streams. For single-phase liquid tests, the aperture of the needle valve entering the receiver tank was restricted to ensure that the liquid is below the saturation temperature.

The compressor does not have a high enough capacity for high qualities and high mass fluxes. In these situations, the pre-heater can be used to boil off some of the liquid stream from the pump in order to achieve higher qualities. The quality at the exit of the pre-heater is found through an energy balance. For the data taken on flat plates, the mass flow rate of the compressor was sufficiently high to reach the desired qualities and mass fluxes of interest without the use of the pre-heater.

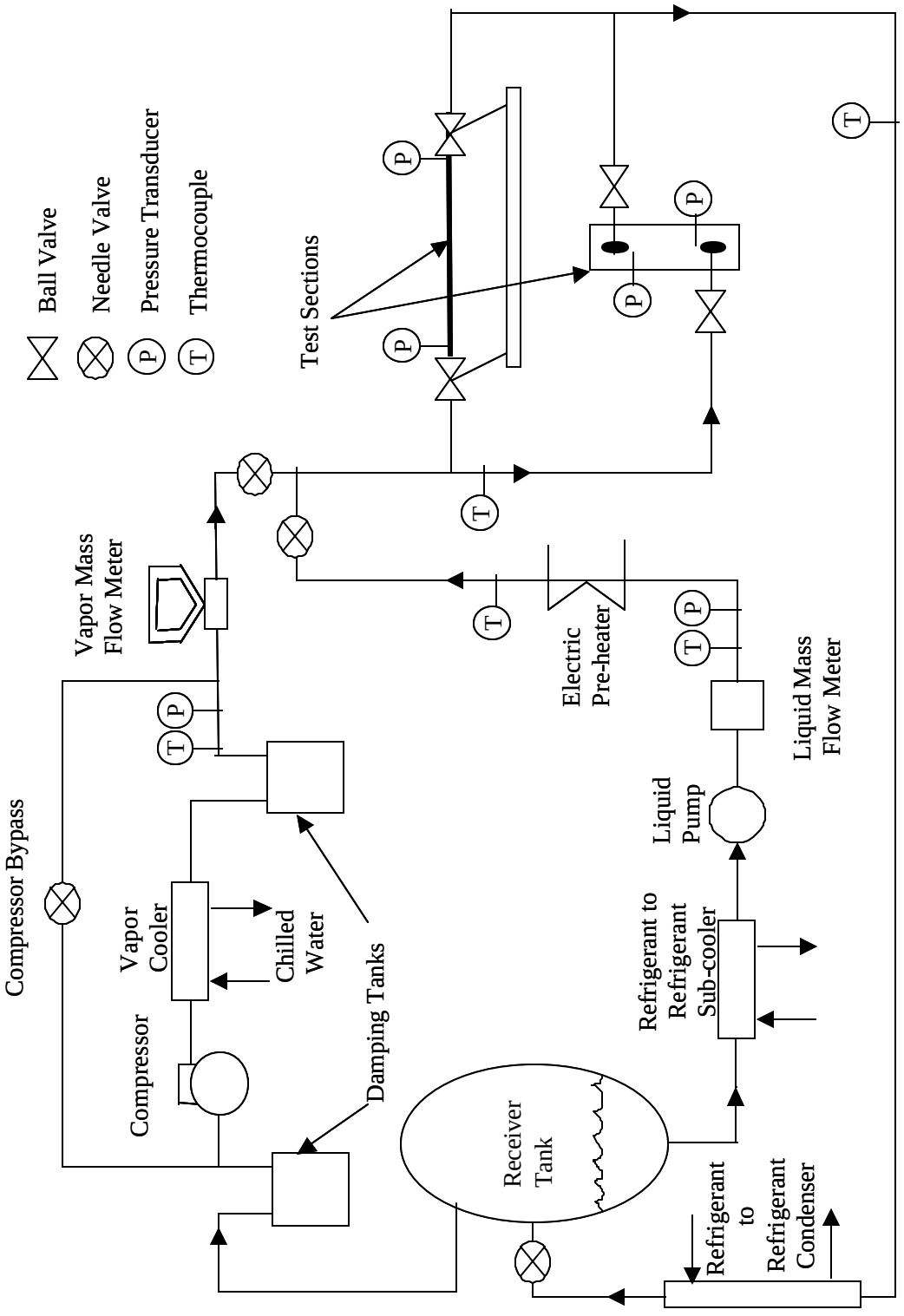

Figure 3.1 Evaporator Test Loop Schematic

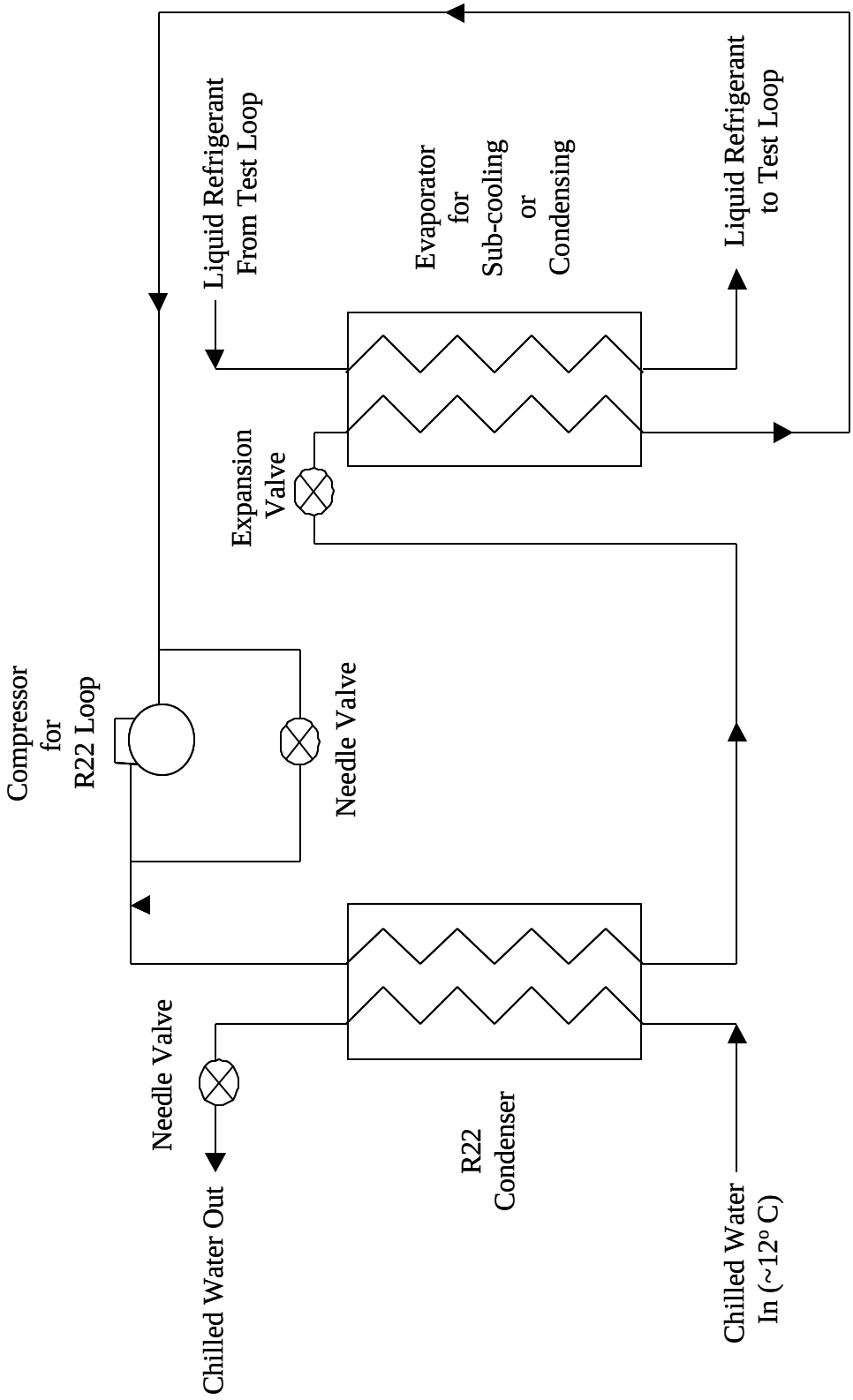

Figure 3.2 Sub-Cooler and Condenser Chiller Loops

Chapter 4: Construction of the Evaporator Test Sections

Three different flat plate geometries were constructed in both brass and clear PVC. This chapter describes the flat plate geometries chosen. In addition, the Pro/Engineer® based modeling and computer numerically controlled (CNC) machining of the flat plate test sections are described.

4.1 Flat Plate Test Section Geometries

Three styles of flat plate evaporator test sections were constructed: a "chevron", a "bumpy" plate with a 2:1 bump aspect ratio, and a "bumpy" plate with a 1:1 bump aspect ratio. The chevron plate is a "half chevron" and has a chevron angle of 60^{o} from the flow direction, a pitch of 9.525 mm (3/8"), a width of 50.8mm (2"), and a 1.59 mm (1/16") half depth as seen in Figure 4.1. The chevron plate grooves also have a quasi-sinusoidal profile with a 3.175mm (1/8") radius of cut as seen in Figure 4.2.

The 1:1 aspect ratio bumpy plate geometry is identical to the chevron geometry except that a mirror image of the chevron pattern was machined into the plate as shown in Figure 4.3. The 2:1 aspect ratio bumpy plate geometry is identical to the 1:1 aspect ratio geometry except narrower grooves were machined over the chevron geometry (see Figure 4.4). The 2:1 aspect ratio bumpy plate additional grooves have a quasi-sinusoidal profile with a 1.59mm (1/16") depth, and a 1.59mm (1/16") radius of cut as depicted in Figure 4.5.

Additional information about the three test section geometries is provided in Table 4.1.

Table 4.1 Test Section Geometry Information

Test Section Plate Geometry	Chevron	1:1 Aspect Ratio Dimpled Plate	2:1 Aspect Ratio Dimpled Plate
Average Cross Sectional Area (m^2)	5.258E-05	7.658E-05	6.769E-05
Minimum Cross Sectional Area (m^2)	4.951E-05	4.951E-05	4.951E-05
Wetted Surface Area (m^2)	2.550E-02	2.532E-02	2.673E-02
Volume (m^3 excluding entrance and exit)	1.828E-05	2.662E-05	2.353E-05

The mean cross sectional area is computed using equation 4.1.

$$A_m = \frac{V_{ts}}{L} \tag{4.1}$$

4.2 Flat Plate Test Section Modeling

The flat plate test sections were modeled using Pro/Engineer® solid modeling. A Pro/Engineer® solid model image of the chevron geometry plate is shown in Figure 4.6. Pro/Manufacture® was used to virtually machine the heat exchangers. First a work-piece is created, which is a virtual piece of bar stock. This work-piece is superimposed over the Pro/Engineer® solid model. Tool geometries, spindle speeds, feed rates, and depths of cut for each pass are specified. The virtual tools are used to virtually machine the work-piece in a series of machining operations. Pro/Engineer® solid model is used as a pattern to guide the tool paths. The tool path can be displayed for each machining operation, which depicts virtual machining of the part. A file is created from the Pro/Manufacture® file which can be converted to the "g-code" that is recognized by the CNC milling center.

4.3 Test Section Machining

An Arrow 2000, CNC three axis milling center, was used to machine the test sections. The brass or clear PVC bar stock is fastened in the machine with clamps and the part is referenced. The part is then machined using the "g-code" loaded into the CNC milling center. The parts are replicated with great precision and consistency, which is desirable for comparing geometries and ensuring that the brass test section geometries used for pressure drop are identical to the clear PVC test sections used for flow visualization. The basic plate geometry is shown in Figure 4.7 for a chevron plate. The entrance and exit sections are identical for all three geometries. The only difference between the three flat plate geometries is the center section containing the chevron or bump features. The clear PVC test sections were machined from larger bar stock in order to reduce stress concentrations, but have the same internal geometry as the brass test sections.

4.4 Test Section Construction

Inlet and outlet fittings were placed on the test sections after the header plates were machined. For the brass test sections, 9.525mm (3/8") headers were drilled in one of the plates and 9.525mm (3/8") copper tube was soldered into each header hole. Teflon tube inserts were placed inside of the 9.525mm (3/8") copper pipe in order to take away some of the header volume for future void fraction experiments. The 3.175mm (1/8") pressure taps were also drilled in the brass test sections into the entrance and exit header sections. Copper tubes, 3.175mm (1/8"), were soldered into each pressure tap. The entrance and exit header geometries are identical. The header geometry used in all the brass flat plate test sections is depicted in Figure 4.8. Finally, ball valves were fastened to the headers and pressure taps, and spring lock quick disconnects were fastened to the other end of the 9.525mm (3/8") ball valves on the headers. The final assembly can be seen in Figure 4.9.

Headers, but no pressure taps, were placed on the clear PVC test sections. 6.35mm (1/4") holes were drilled for the clear PVC headers. The headers were connected to 6.35mm (1/4") copper pipe by bolting a brass plate with a seal groove machined in it to allow for a 1.59mm (1/16") neoprene o-ring (14.3mm OD) which is pressed against the clear PVC by 3.175mm (1/8") bolts that go through the brass plate and are tightened into taped holes in the clear PVC. The clear PVC header plates are depicted in Figure 4.10 and the picture of the entire clear PVC test section assembly is shown in Figure 4.11.

Both the brass and clear PVC test sections utilize a 2.38mm (3/32”) neoprene o-ring seal made from neoprene cord and joined with CA adhesive. The seal is placed in a seal groove and the test section halves are bolted together with 6.35mm (1/4”) bolts. The brass test sections also required a thin layer of RTV silicone sealant in and around the seal grooves in order to ensure proper sealing.

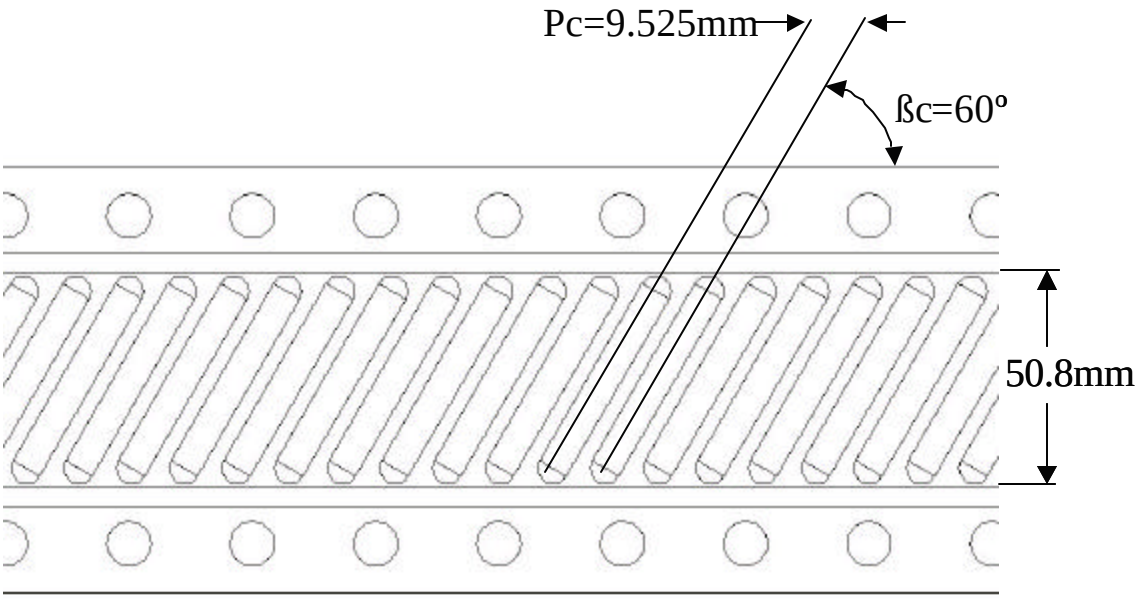

Figure 4.1 Chevron Plate Test Section Geometry

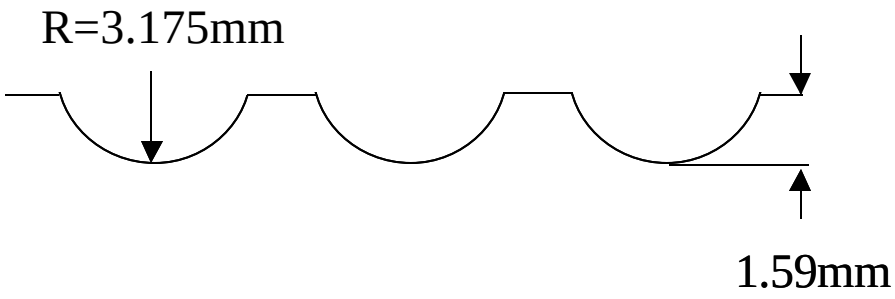

Figure 4.2 Chevron Plate Test Section Groove Geometry (Edge View)

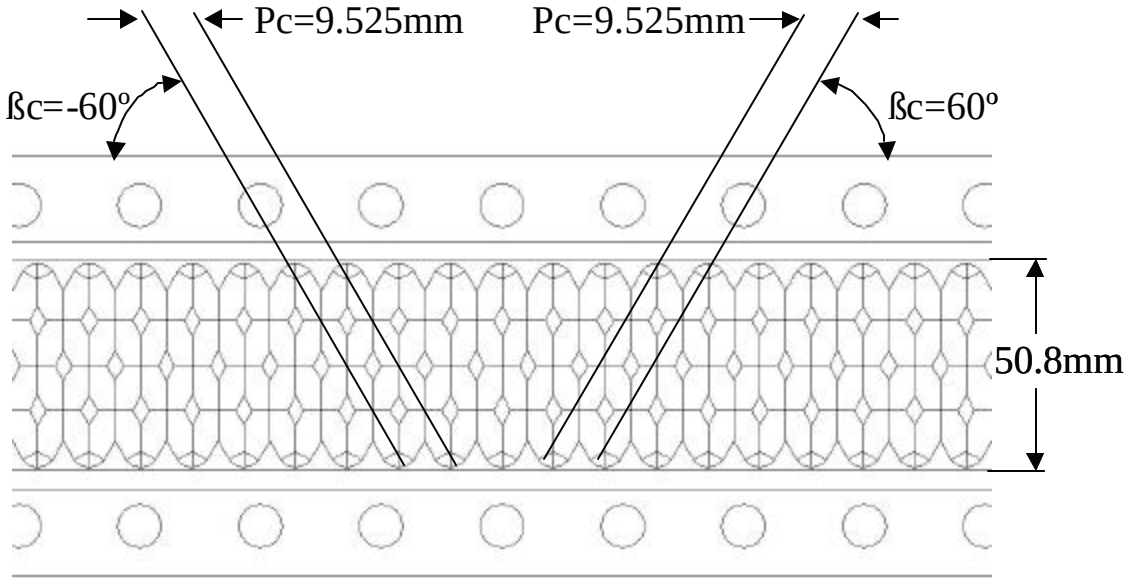

Figure 4.3 1:1 Aspect Ratio Bumpy Plate Test Section Geometry

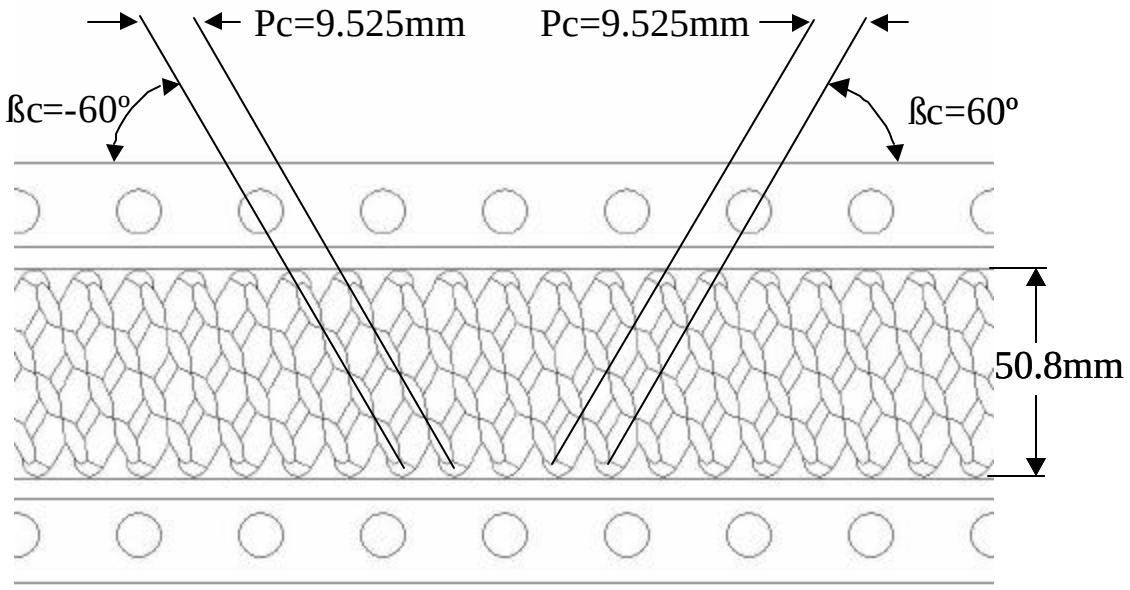

Figure 4.4 2:1 Aspect Ratio Bumpy Plate Test Section Geometry

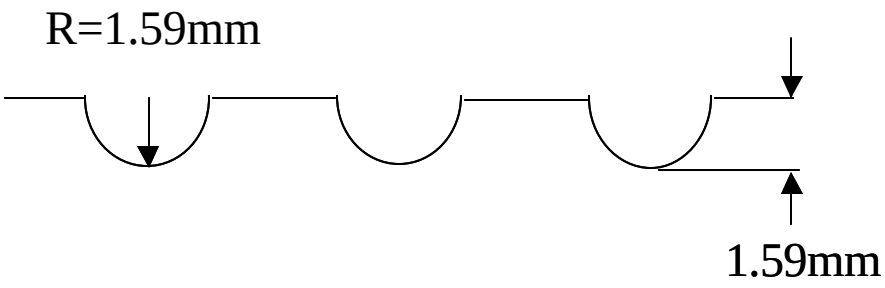

Figure 4.5 2:1 Aspect Ratio Bumpy Plate Test Section Additional Groove Geometry (Edge View)

Figure 4.6 Pro/Engineer® Solid Model of the Chevron Plate

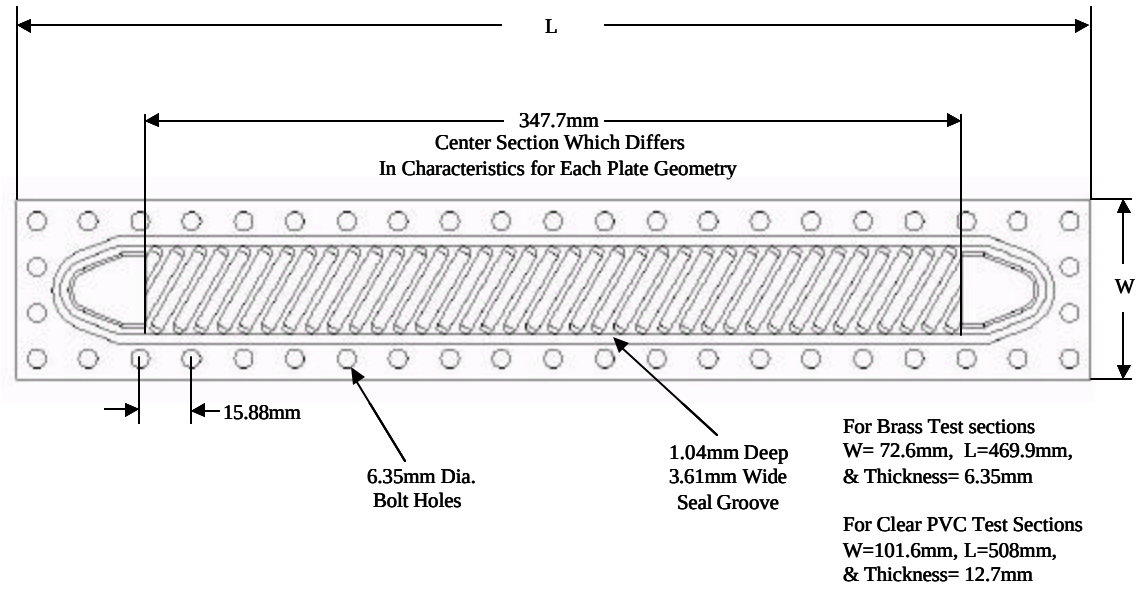

Figure 4.7 Test Section Geometry

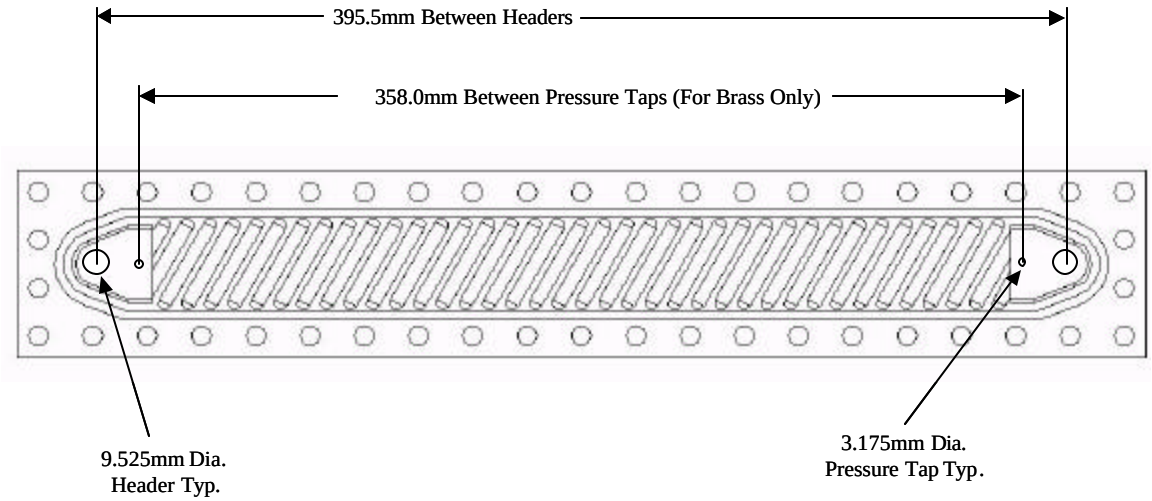

Figure 4.8 Brass Test Section Header Details

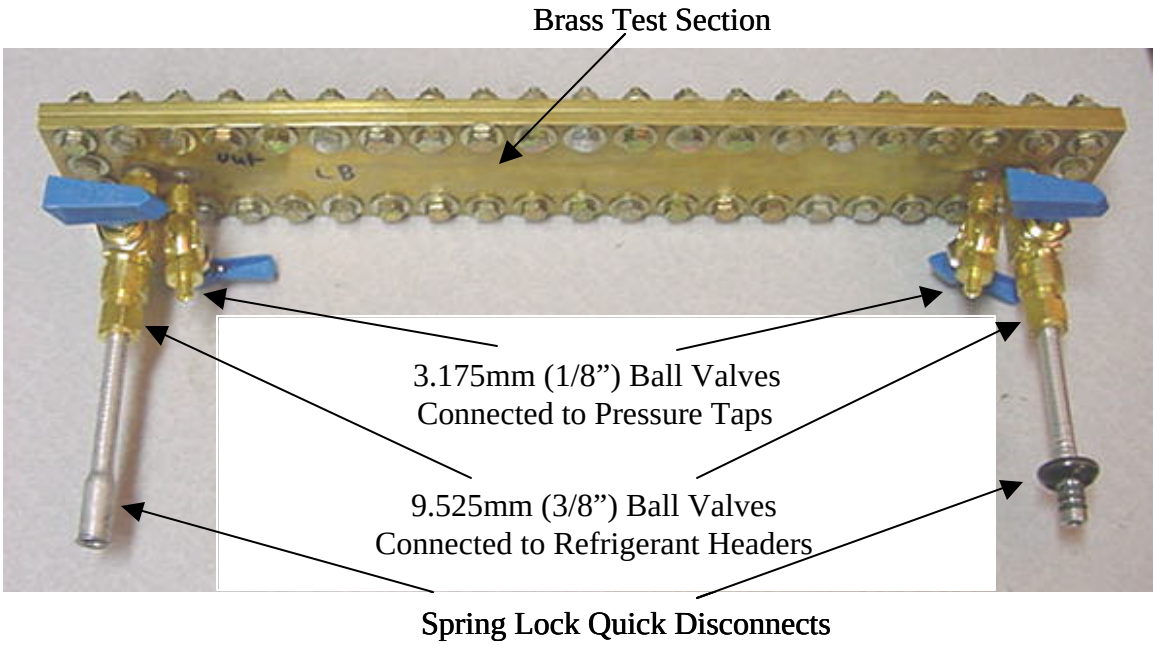

Figure 4.9 Picture of a Brass Test Section

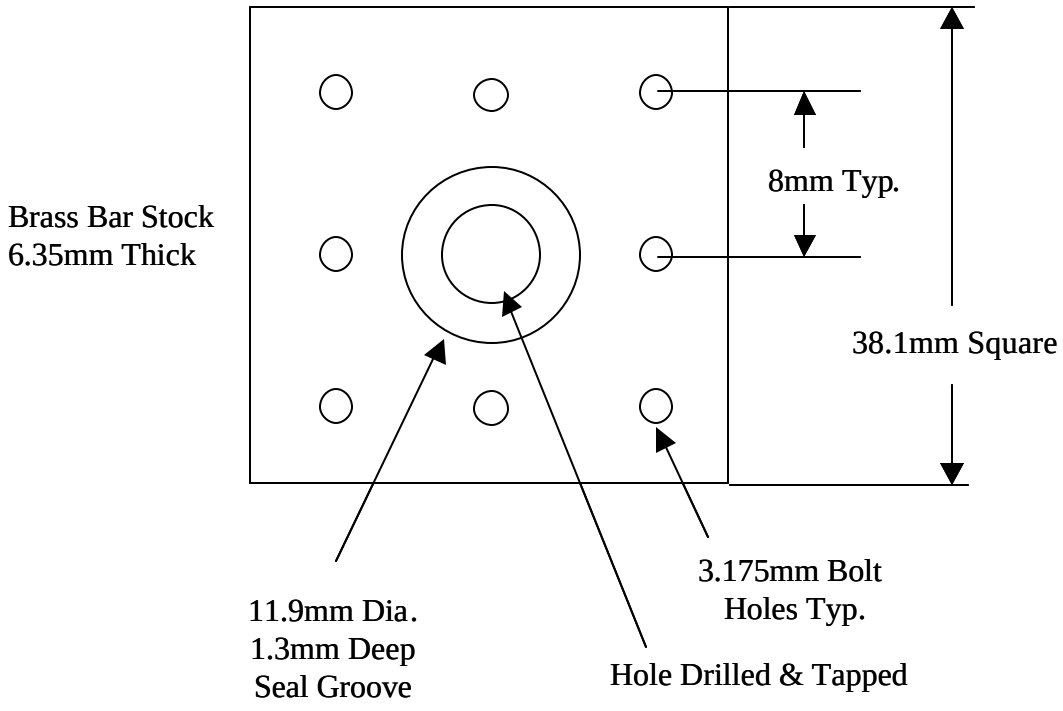

Figure 4.10 Brass Plate for Fastening Headers to Clear PVC Test Sections

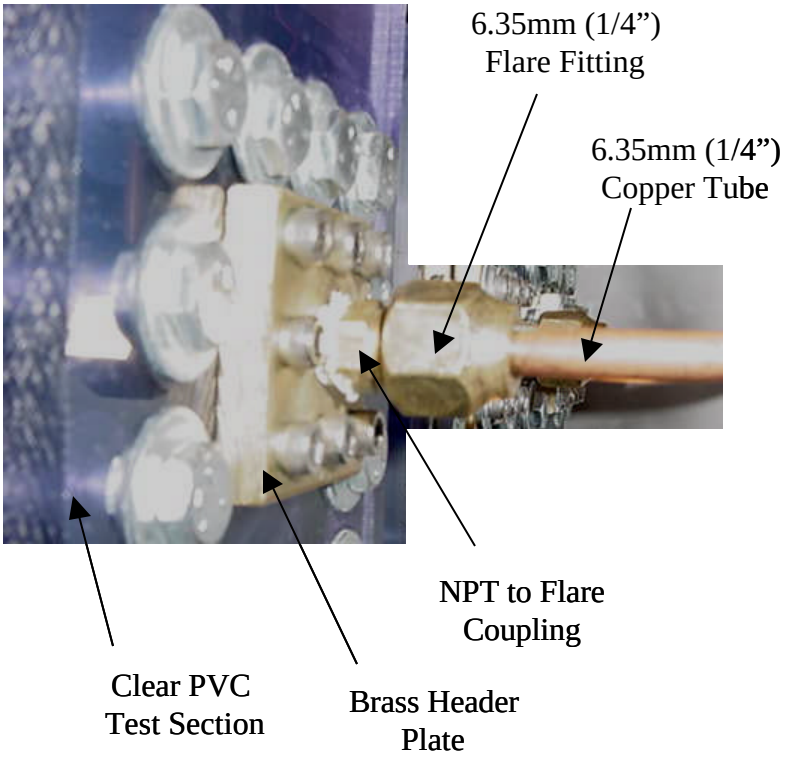

Figure 4.11 Clear PVC Header Details

Chapter 5: Flat Plate Pressure Drop Data

The results of pressure drop tests on the chevron plate, the 1:1 aspect ratio bumpy plate, and the 2:1 aspect ratio bumpy plate heat exchangers are presented in this chapter. The pressure drop data is compared on mass flux and mass flow rate bases.

5.1 Flat Plate Pressure Drop Tests

The tests were performed under adiabatic conditions, upward flow, with R134a. Pressure drops at both 10^{o} C and 20^{o} C test section inlet saturation temperatures were investigated. The pressure drop data was obtained for a wide range of qualities including sub-cooled liquid and superheated vapor, and a variation of mass fluxes. The sub-cooled liquid is sub-cooled to a temperature within approximately 1^{o} C below the saturation temperature. The amount of vapor superheat was difficult to control, so the values are not the same for each data point. The sub-cooled liquid is referred to as liquid and the super-heated vapor is referred to as vapor in the legends of the pressure drop plots in Figures 5.1 through 5.12. The pressure drop measurements include the gravitational head of the fluid column because the tests were performed with vertical upward flow. Each pressure drop data point represents an average of approximately 30 pressure drop and mass flux readings. The averaged pressure drop data for all three heat exchangers, at 10^{o} C and 20^{o} C test section inlet saturation temperatures, can be seen in the tables in Appendix A. The saturation temperature represents the inlet saturation temperature; consequently there is a decrease in refrigerant temperature and increase in quality across the test sections due to the pressure drop.

5.2 Chevron Plate Pressure Drop Data

The pressure drop versus mass flux data is depicted for the chevron test section at a 10^{o} C saturation temperature in Figure 5.1 and at a 20^{o} C saturation temperature in Figure 5.2. It is evident that the increase of the saturation temperature results in a decrease in pressure drop. This decrease in pressure drop can be attributed to the increase in vapor density associated with a higher saturation pressure. An increase in vapor density will result in a lower vapor velocity at a given mass flux and quality. A lower vapor velocity, in turn, results in a lower pressure drop.

The pressure drop for the chevron plate was found to be the highest of the three plate geometries tested at a given quality, mass flux, and saturation temperature. When the data is compared on a mass flow rate basis, the pressure drop associated with the chevron is significantly higher, because the chevron geometry has the smallest mean cross sectional area ($0.0000526 m^2$). The plots of pressure drop versus mass flow rate for the chevron geometry can be seen in Figures 5.3 and 5.4 for 10^{o} C and 20^{o} C saturation temperatures, respectively.

5.3 1:1 Aspect Ratio Bumpy Plate Pressure Drop Data

Figures 5.5 and 5.6 show the pressure drop versus mass flux data for the 1:1 aspect ratio bumpy plate at 10^{o} C and 20^{o} C saturation temperatures, respectively. As seen in the chevron plates, the increase in saturation temperature decreases the pressure drop due to the higher associated vapor density.

The pressure drop associated with the 1:1 aspect ratio bumpy plate had the lowest pressure drop of the three flat plates tested at a given quality, mass flux, and saturation temperature. On a mass flow rate basis, the 1:1 aspect ratio bumpy plate had a significantly lower pressure drop associated with it, because it had the largest mean test section area ($0.0000766 m^2$). The plots of pressure drop versus mass flow rate for the 1:1 aspect ratio bumpy plate geometry can be seen in Figures 5.7 and 5.8 for 10^o C and 20^o C saturation temperatures, respectively.

5.4 2:1 Aspect Ratio Bumpy Plate Pressure Drop Data

Figures 5.9 and 5.10 show the pressure drop versus mass flux data for the 2:1 aspect ratio bumpy plate at 10^o C and 20^o C saturation temperatures, respectively. From inspection of these plots, an increase in saturation temperature was found to decrease the pressure drop, as was found in the chevron and 1:1 aspect ratio bumpy plates.

The pressure drop values for the 2:1 aspect ratio bumpy plate were found to be between the pressure drop of the chevron and the 1:1 aspect ratio bumpy plates at a given quality, mass flux, and saturation temperature. On a mass flow rate basis, the same trend is more pronounced because the 2:1 aspect ratio plate has a different mean cross sectional area ($0.0000677 m^2$). The plots of pressure drop versus mass flow rate for the 2:1 aspect ratio bumpy plate geometry can be seen in Figures 5.11 and 5.12 for 10^o C and 20^o C saturation temperatures, respectively.

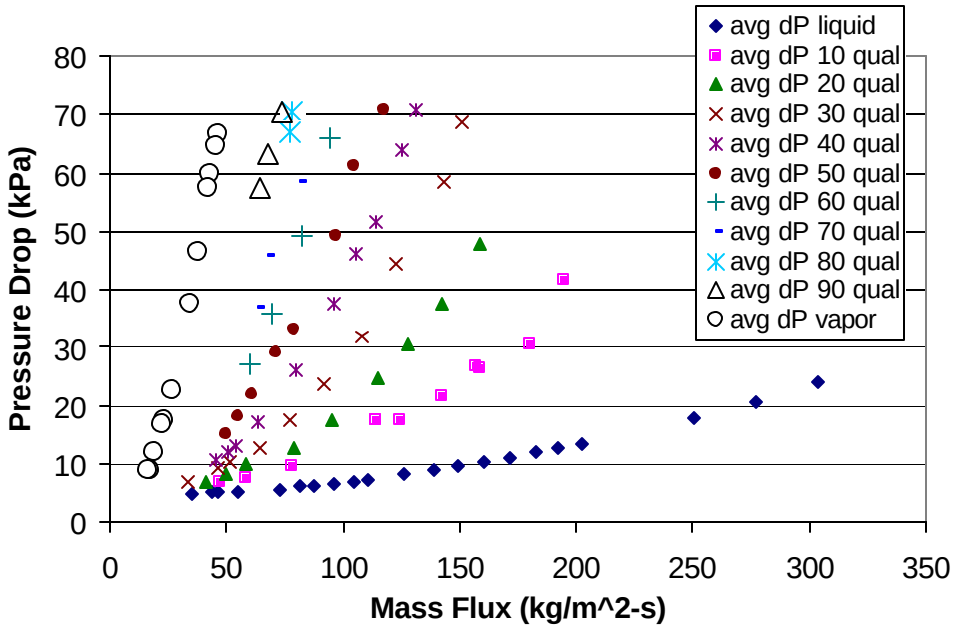

Figure 5.1 Pressure Drop Versus Mass Flux for Chevron Plate at 10^o C Inlet (Adiabatic, Upward Flow, R134a)

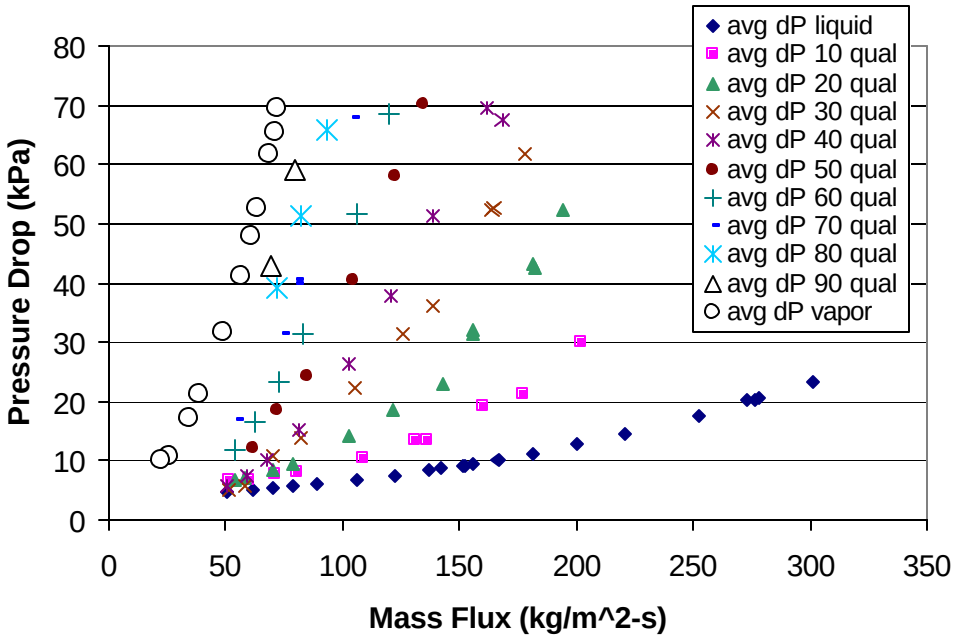

Figure 5.2 Pressure Drop Versus Mass Flux for Chevron Plate at 20° C Inlet (Adiabatic, Upward Flow, R134a)

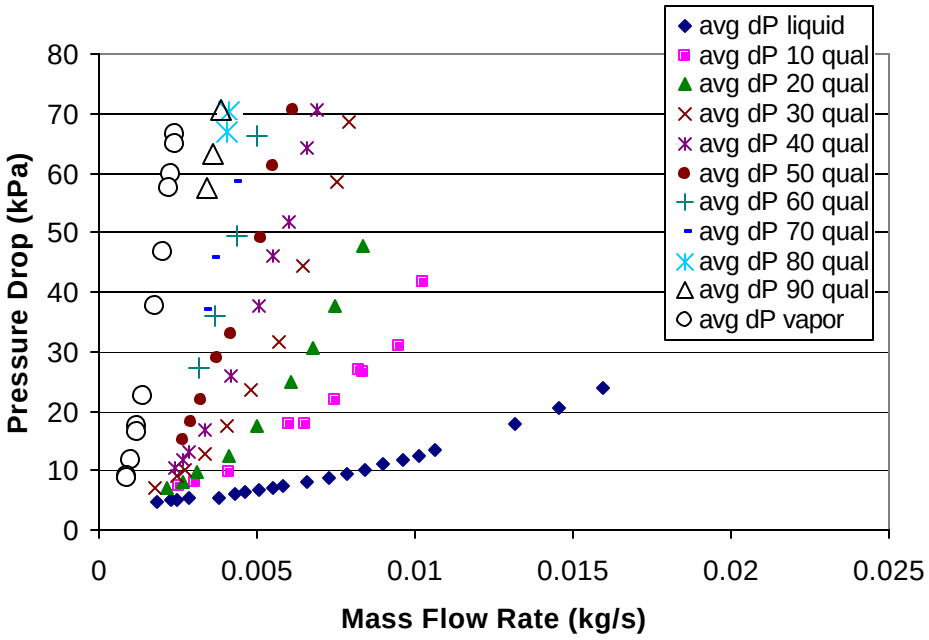

Figure 5.3 Pressure Drop Versus Mass Flow Rate for Chevron Plate at 10° C Inlet (Adiabatic, Upward Flow, R134a)

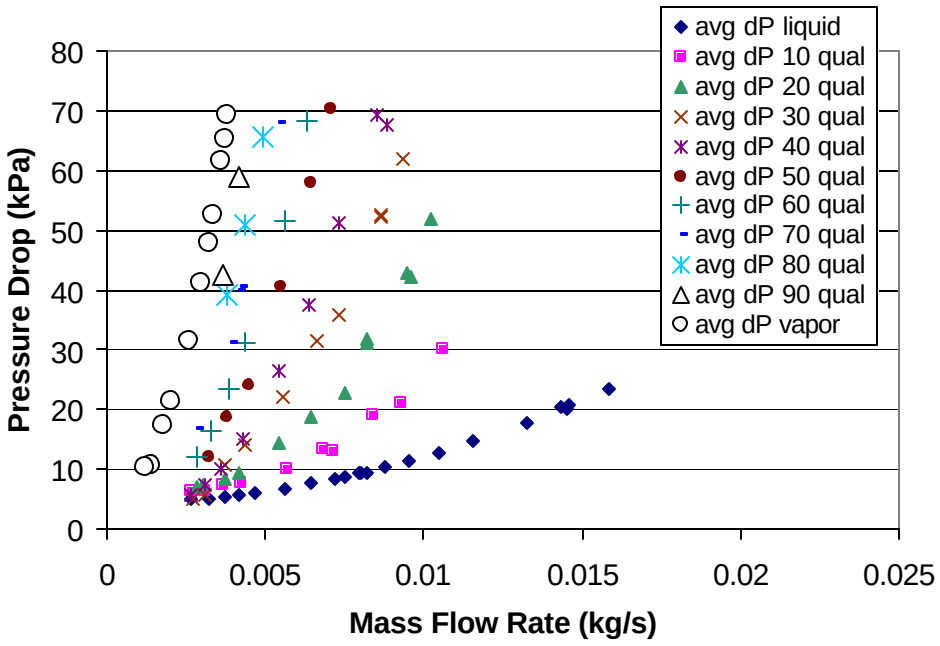

Figure 5.4 Pressure Drop Versus Mass Flow Rate for Chevron Plate at 20° C Inlet (Adiabatic, Upward Flow, R134a)

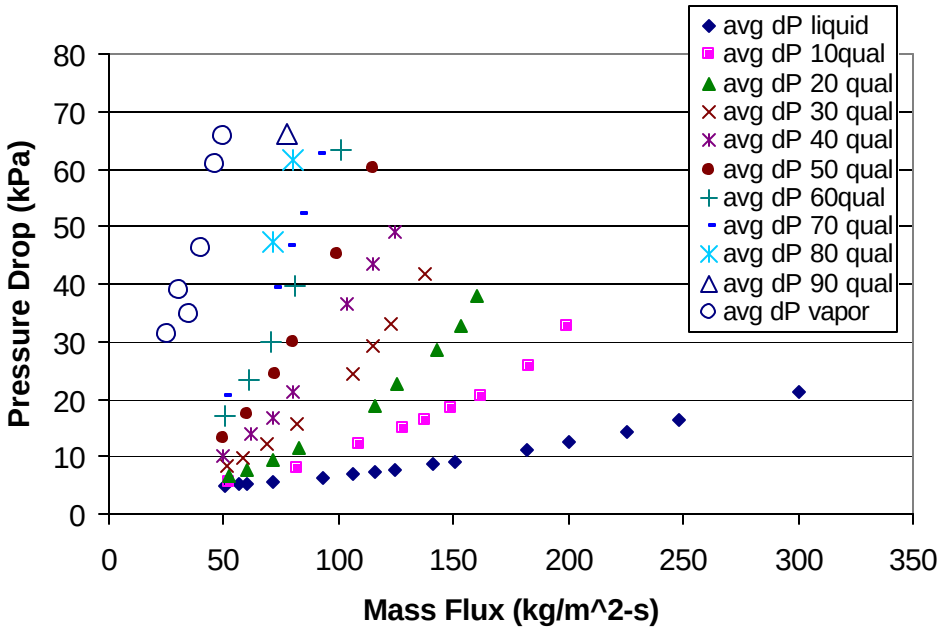

Figure 5.5 Pressure Drop Versus Mass Flux for 1:1 Aspect Ratio Bumpy Plate at 10° C Inlet (Adiabatic, Upward Flow, R134a)

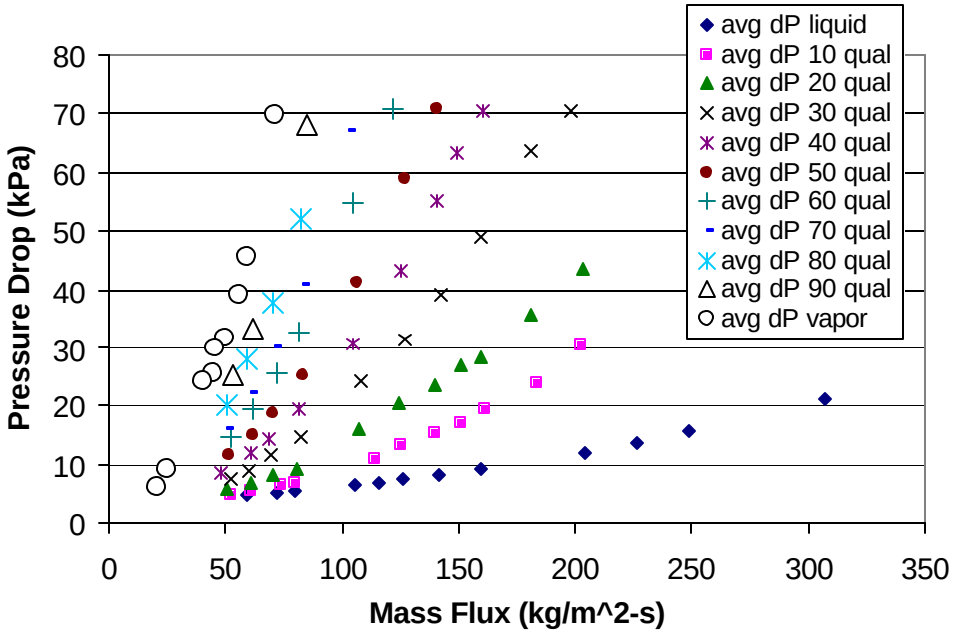

Figure 5.6 Pressure Drop Versus Mass Flux for 1:1 Aspect Ratio Bumpy Plate at 20° C Inlet (Adiabatic, Upward Flow, R134a)

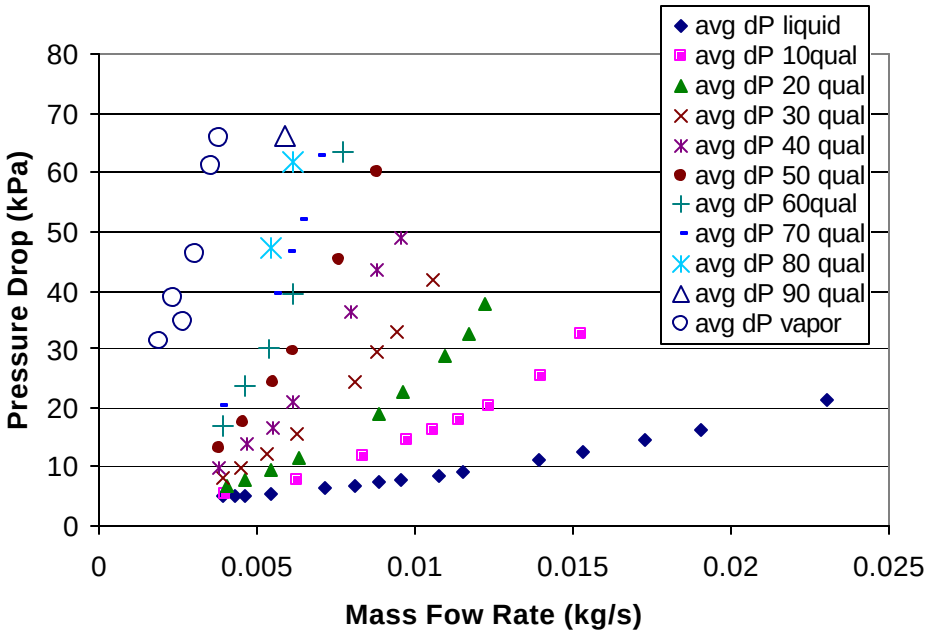

Figure 5.7 Pressure Drop Versus Mass Flow Rate for 1:1 Aspect Ratio Bumpy Plate at 10° C Inlet (Adiabatic, Upward Flow, R134a)

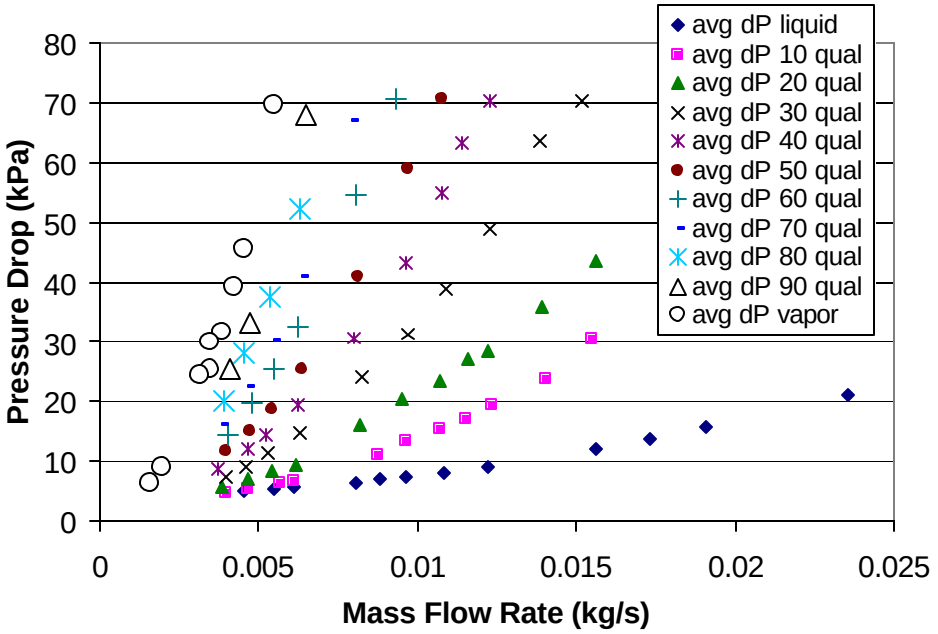

Figure 5.8 Pressure Drop Versus Mass Flow Rate for 1:1 Aspect Ratio Bumpy Plate at 20° C Inlet (Adiabatic, Upward Flow, R134a)

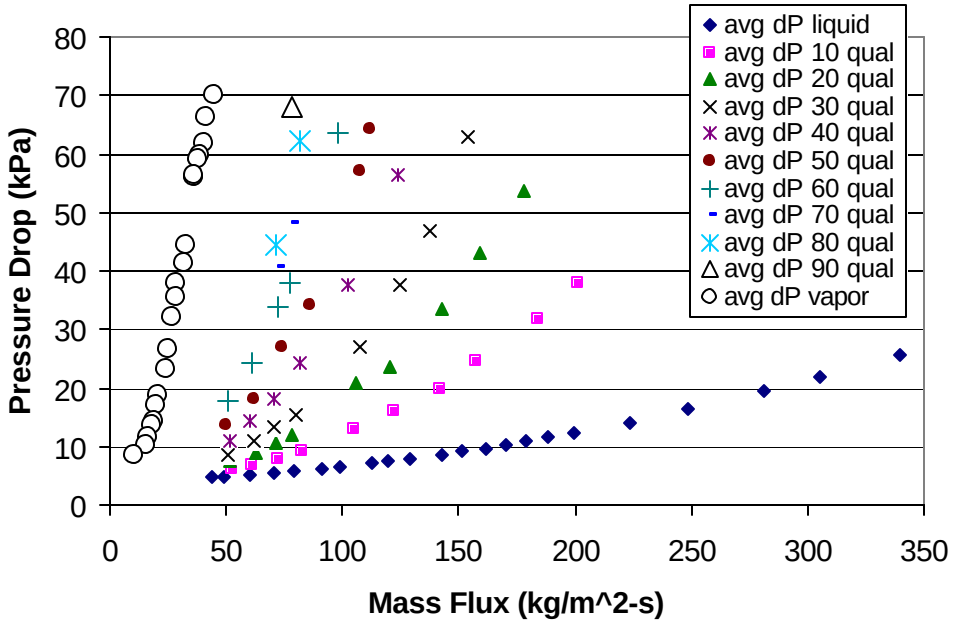

Figure 5.9 Pressure Drop Versus Mass Flux for 2:1 Aspect Ratio Bumpy Plate at 10° C Inlet (Adiabatic, Upward Flow, R134a)

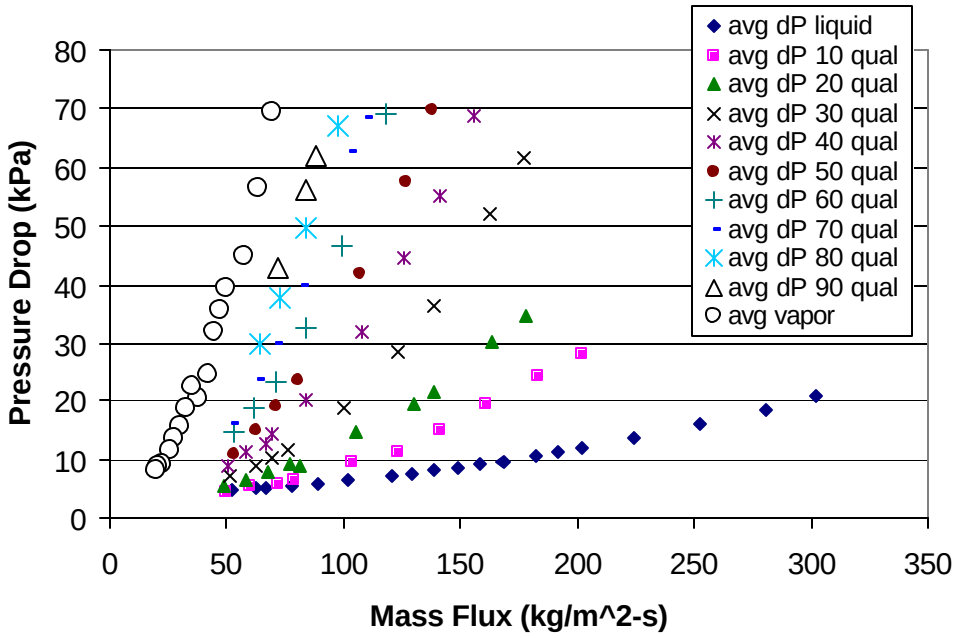

Figure 5.10 Pressure Drop Versus Mass Flux for 2:1 Aspect Ratio Bumpy Plate at 20° C Inlet (Adiabatic, Upward Flow, R134a)

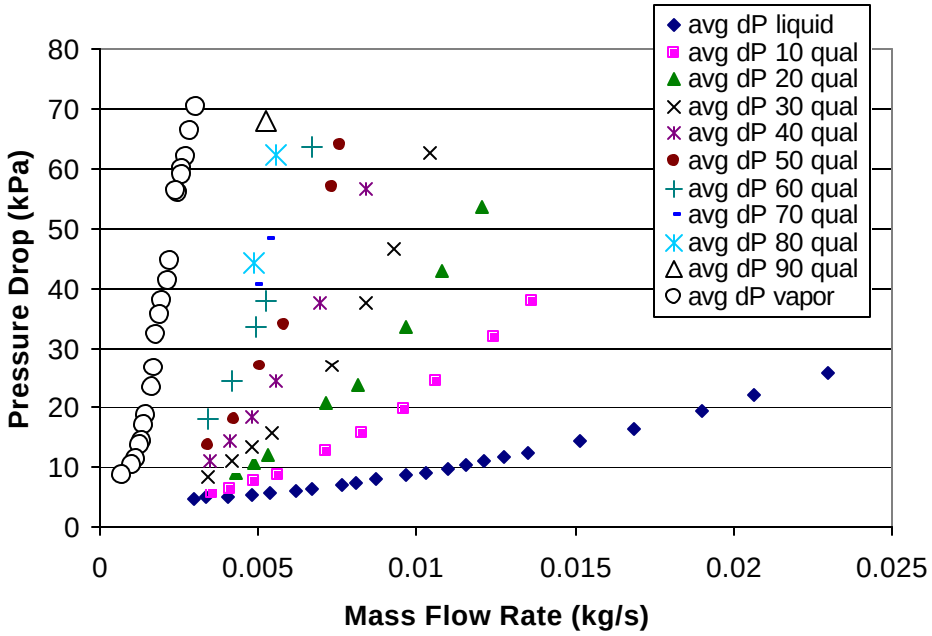

Figure 5.11 Pressure Drop Versus Mass Flow Rate for 2:1 Aspect Ratio Bumpy Plate at 10° C Inlet (Adiabatic, Upward Flow, R134a)

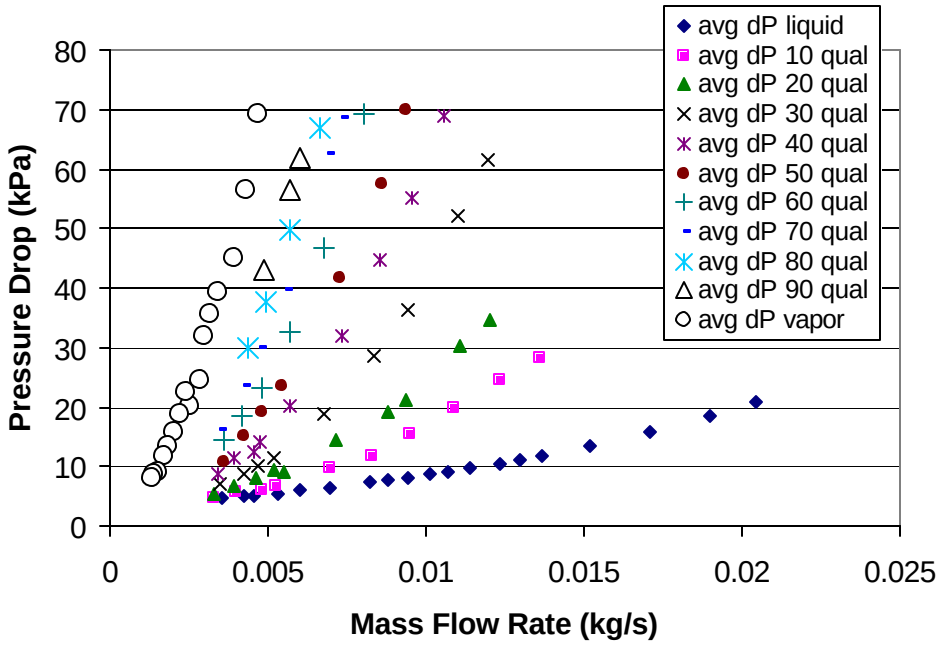

Figure 5.12 Pressure Drop Versus Mass Flow Rate for 2:1 Aspect Ratio Bumpy Plate at 20° C Inlet (Adiabatic, Upward Flow, R134a)

Chapter 6: Flat Plate Flow Visualization

The observations from flow visualization experiments conducted on the chevron plate, the 1:1 aspect ratio bumpy plate, and the 2:1 aspect ratio bumpy plate heat exchangers are presented in this chapter. The flow regimes present in the three geometries of flat plate heat exchangers and the differences in flow patterns and flow regime transitions between the heat exchangers are identified. In addition, qualitative heat transfer rate predictions are made for the three geometries.

6.1 Flat Plate Flow Visualization Experiments

The flow visualization was performed under adiabatic conditions, upward flow, with R134a at 10^{o} C saturation temperature. The flow characteristics of the three heat exchangers have been examined for three different mass fluxes: 60, 90 and 125 kg/m^2-s over a range of qualities. A Hi8 digital video camera was used to take video images of the flow. A 4x magnification lens was used on the camera to magnify the image. In addition, a stroboscope was placed behind the test section (on the opposite side of the test section as the camera) and reflected light off of a white background behind the test section as shown in Figure 6.1. The optimal frequency to allow proper exposure was found to be 4800 flashes per minute. The pictures were taken at a point 9.5 mm from the entrance of the flat plate geometry. The clear PVC test section mounting configuration can be observed in Figure 6.2.

6.2 Observed Flow Regimes

Four different types of two-phase flow configurations were found in all three of the flat plate geometries tested. "Bubbly" flow, observed in Figures 6.3, 6.4, and 6.5 (pictures of flow in 1:1 aspect ratio, 2:1 aspect ratio, and chevron plates, respectively) exists at low quality ranges where vapor bubbles are moving within the fluid. The bubbles tend to merge together as the quality increases. Annular flow exists when the vapor bubbles have fully merged. In annular flow, the liquid refrigerant is confined to a film on the walls of the heat exchanger so that the vapor has an unobstructed path throughout the heat exchanger. At low quality ranges, the flow is characterized as rough annular flow where the liquid film is thick and the boundary between the liquid and the vapor is rough as seen in Figures 6.6, 6.7, and 6.8 (pictures of flow in 1:1 aspect ratio, 2:1 aspect ratio, and chevron plates, respectively). As the quality increases, the flow regime can be characterized as smooth annular flow where the liquid film becomes thinner and the liquid vapor interface becomes smoother as seen in Figures 6.9,6.10, and 6.11 (pictures of flow in 1:1 aspect ratio, 2:1 aspect ratio, and chevron plates, respectively). Finally, a mist flow regime develops where fine liquid particles are ripped off the walls and carried in the vapor stream. Mist flow occurs in combination with annular flow in the flat plate heat exchangers investigated and can be observed in Figures 6.9, 6.10, and 6.11.

Flow regime maps for the 1:1 aspect ratio bumpy plate, 2:1 aspect ratio bumpy plate, and the chevron plate geometries are depicted in Figures 6.12, 6.13, and 6.14, respectively. These maps show all of the observed points plotted on a mass flux versus quality basis. Lines are drawn where the flow regime boundaries are observed.

6.3 Factors Influencing Flow Regime

The flow regime that exists in the flat plate heat exchanger depends not only on quality, but was found to depend on the plate geometry, and mass flux as well. The chevron geometry was seen to exhibit annular flow at lower qualities than the bumpy plate geometries at the same mass flux. The 1:1 aspect ratio bumpy plate transitioned to rough annular flow at a quality of 15% for a mass flux of 60kg/m^2-s, but the chevron geometry transitions to rough annular flow at a quality of 10% with the same mass flux. The 2:1 aspect ratio bumpy plate transitioned to rough annular flow at quality levels between that of the chevron and the 1:1 aspect ratio bumpy plate, between 10 and 15% quality. The increase of mass flux also was observed to cause the transition from bubbly flow to rough annular flow at lower qualities for a given geometry. For example, at a mass flux of 125 kg/m^2-s, in the 1:1 aspect ratio bumpy plate, this transition occurs at a quality of 10%, whereas at a mass flux of 60kg/m^2-s the transition is seen to occur at 15% quality.

6.4 Additional Flow Observations and Comparisons

All three heat exchanger geometries were found to induce liquid entrainment. The liquid entrainment is most clearly pronounced in the rough annular flow regime. In Figure 6.6, liquid entrainment exists downstream of the 1:1 aspect ratio bumps and appears to be symmetric with respect to the flow direction. Liquid entrainment exists downstream of the 2:1 aspect ratio bumps as seen in Figure 6.7. However, the liquid entrainment is not symmetric with respect to the flow direction. The liquid is found to be entrained more on the left side of the top plate bumps, and the liquid is similarly entrained more on the right side of the bottom plate bumps (this is difficult to see in the pictures because it is on the other side of the plate). Liquid entrainment can be observed in the chevron plate in Figure 6.8. Here, it can be seen that the liquid is entrained downstream of the locations where the top and bottom plates come into contact.

The flow direction was found to be distinctly different between the chevron style and bumpy style geometries tested. The flow in the 1:1 aspect ratio bumpy style plate was seen to travel through 4 different "zigzagging" channels. The fluid did not appear to communicate between the channels for the observed quality ranges. The 2:1 aspect ratio bumpy plate appeared to have a more complicated "zigzagging" flow. It seems that part of the flow zigzags like the 1:1 aspect ratio bumpy plate but some of the flow must travel between the top and bottom plates in order to maintain a constant cross sectional area. The chevron plate was seen to have a more complex mixing action. The fluid was observed not only to follow the grooves but also flowed over the interconnecting groove passages.

6.5 Heat Transfer Predictions

Factors such as flow regime present and the surface area to volume ratio of a heat exchanger can affect the heat transfer rates. The flow maps of the heat exchangers are noticeably different. The chevron geometry appears to develop rough annular and smooth annular flow at lower qualities and mass fluxes than the other heat exchanger geometries. The 1:1 aspect ratio bumpy plate transitions to rough and smooth annular flow at the highest qualities and mass fluxes. The 2:1 aspect ratio bumpy plate transitions to rough and smooth annular flow at mass fluxes and qualities between the other two geometries. If flow regime conditions are dominant in the determination of the heat

transfer rates, the chevron plate can be expected to have the highest heat transfer rate associated with it and the round dimpled plate can be expected to have the lowest heat transfer rate.

Investigation of the differences in the surface area to volume ratios of the three different heat exchanger geometries also suggests that the chevron would have the highest and the 1:1 aspect ratio dimpled plate would have the lowest heat transfer rates associated with them. The chevron plate has the largest surface area to volume ratio ($1395 m^{-1}$), which could help facilitate heat transfer. The 1:1 aspect bumpy plate was found to have the lowest surface area to volume ratio ($951 m^{-1}$). The 2:1 aspect ratio bumpy plate has a surface area to volume ratio between the values of other two geometries ($1136\ m^{-1}$).

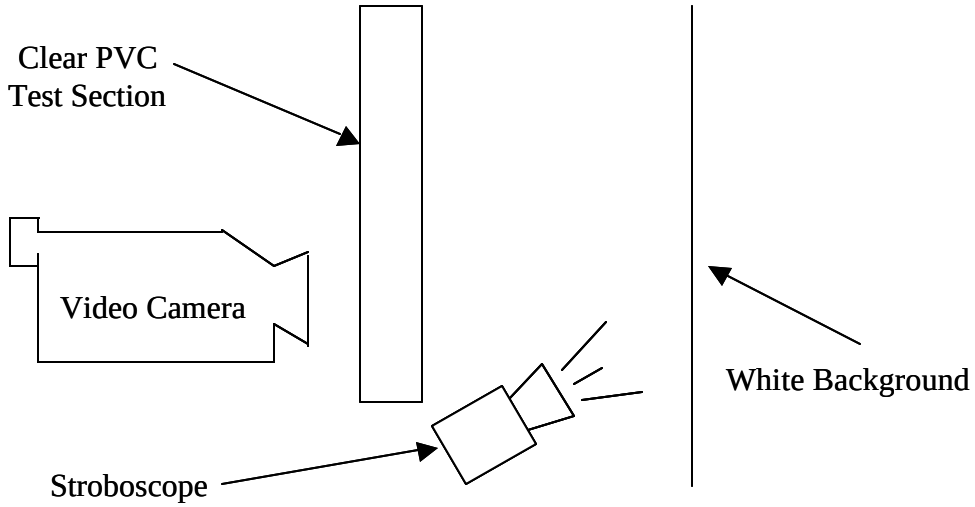

Figure 6.1 Flow Visualization Setup Schematic

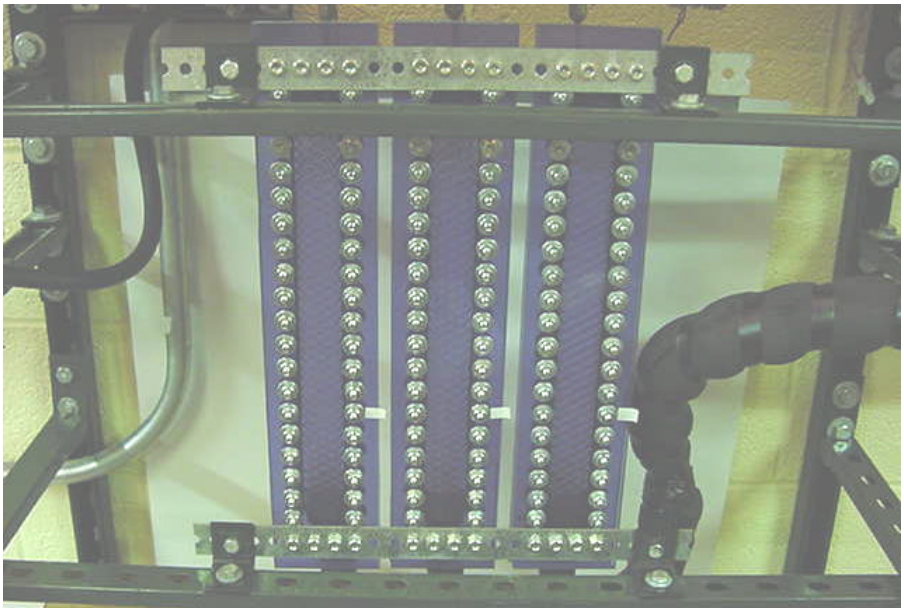

Figure 6.2 Clear PVC Test Section Mounting

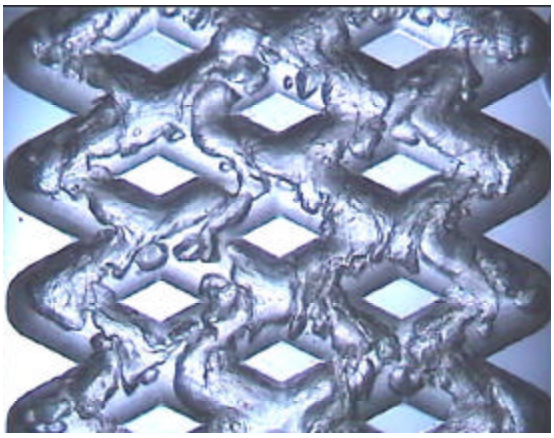

Figure 6.3 Bubbly Flow in the 1:1 Aspect Ratio Bumpy Plate at a Quality of 5% and Mass Flux of 60 kg/m^2-s (Adiabatic, Upward Flow, R134a, 10^o C)

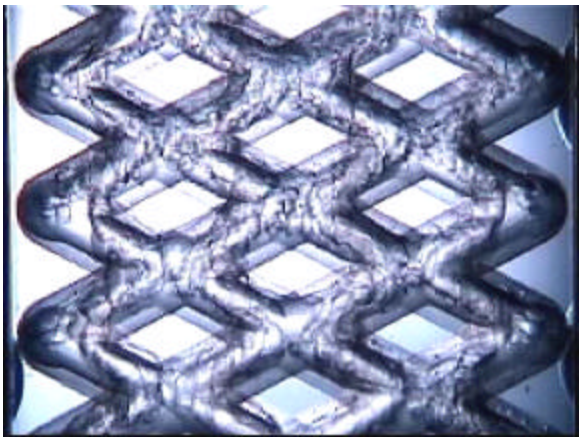

Figure 6.4 Bubbly Flow in the 2:1 Aspect Ratio Bumpy Plate at a Quality of 5% and Mass Flux of 60kg/ m^2-s (Adiabatic, Upward Flow, R134a, 10^o C)

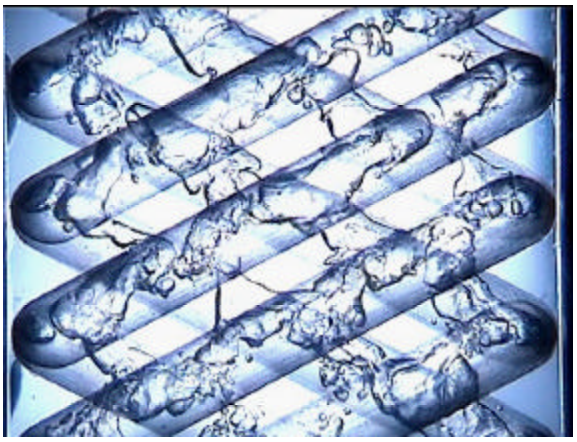

Figure 6.5 Bubbly Flow in the Chevron Plate at a Quality of 5% and Mass Flux of 90 kg/m^2-s (Adiabatic, Upward Flow, R134a, 10^o C)

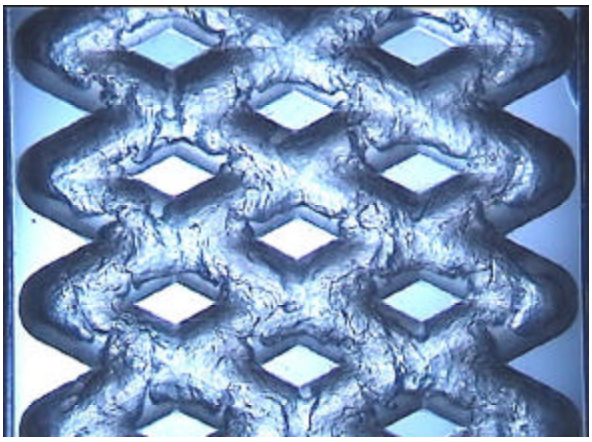

Figure 6.6 Rough Annular Flow in the 1:1 Aspect Ratio Bump y Plate at a Quality of 15% and Mass Flux of 60 kg/m^2-s (Adiadabatic, Upward Flow, R134a, 10^o C)

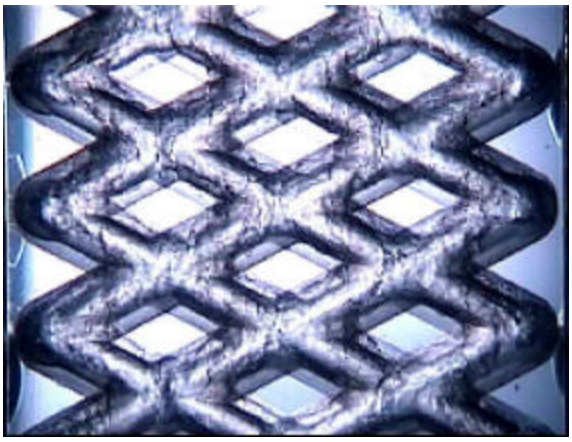

Figure 6.7 Rough Annular Flow in the 2:1 Aspect Ratio Bumpy Plate at a Quality of 15% and Mass Flux of 60 kg/m^2-s (Adiabatic, Upward Flow, R134a, 10^o C)

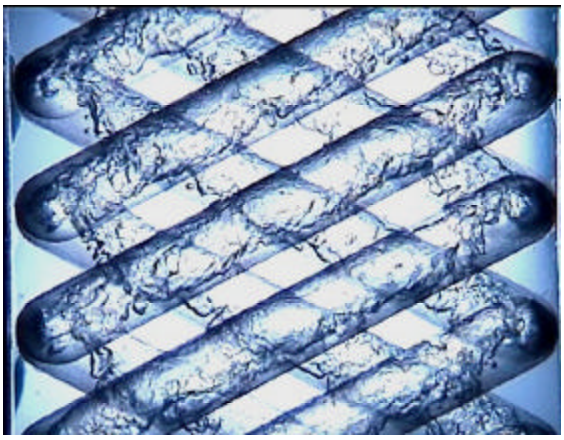

Figure 6.8 Rough Annular Flow in the Chevron Plate at a Quality of 10% and a Mass Flux of 90kg/m^2-s (Adiabatic, Upward Flow, R134a, 10^o C)

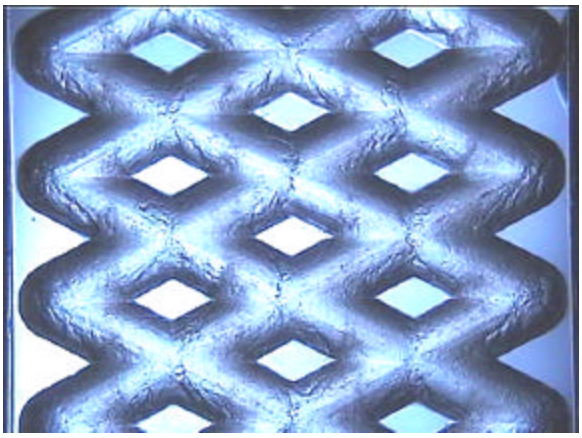

Figure 6.9 Smooth Annular/Mist Flow in the 1:1 Aspect Ratio Bumpy Plate at a Quality of 70% and Mass Flux of 60 kg/m^2-s (Adiabatic, Upward Flow, R134a, 10^o C)

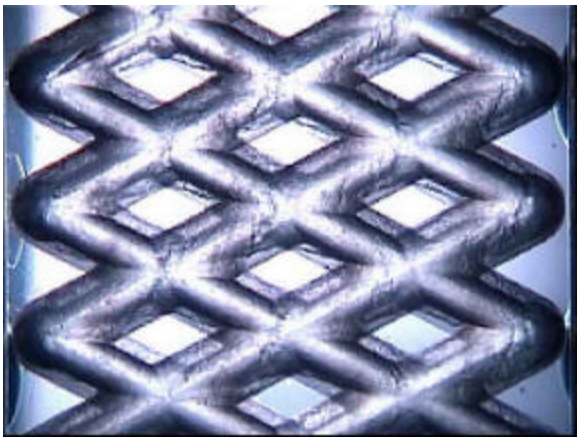

Figure 6.10 Smooth Annular/Mist Flow in the 2:1 Aspect Ratio Bumpy Plate at a Quality of 60% and Mass Flux of 60 kg/m^2-s (Adiabatic, Upward Flow, R134a, 10^o C)

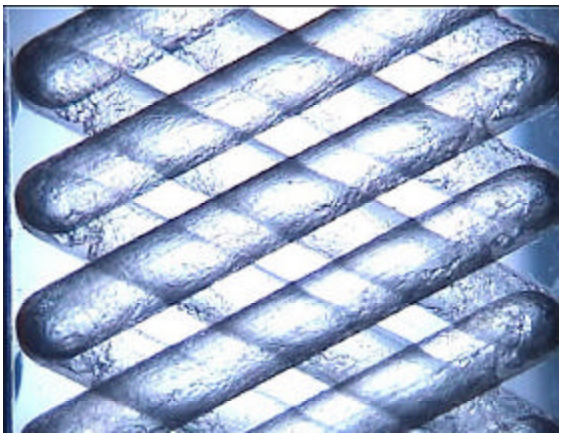

Figure 6.11 Smooth Annular/Mist Flow in the Chevron Plate at a Quality of 50% and a Mass Flux of 90kg/m^2-s (Adiabatic, Upward Flow, R134a, 10^o C)

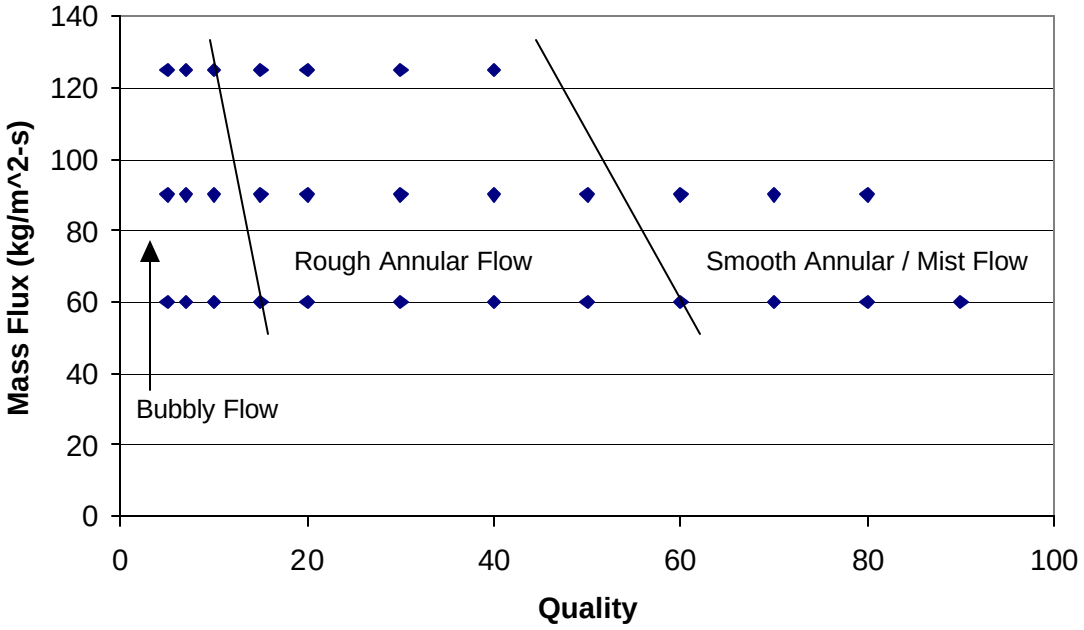

Figure 6.12 Mass Flux Versus Quality Flow Regime Map for the 1:1 Aspect Ratio Bumpy Plate (Adiabatic, Upward Flow, R134a, 10^{o} C)

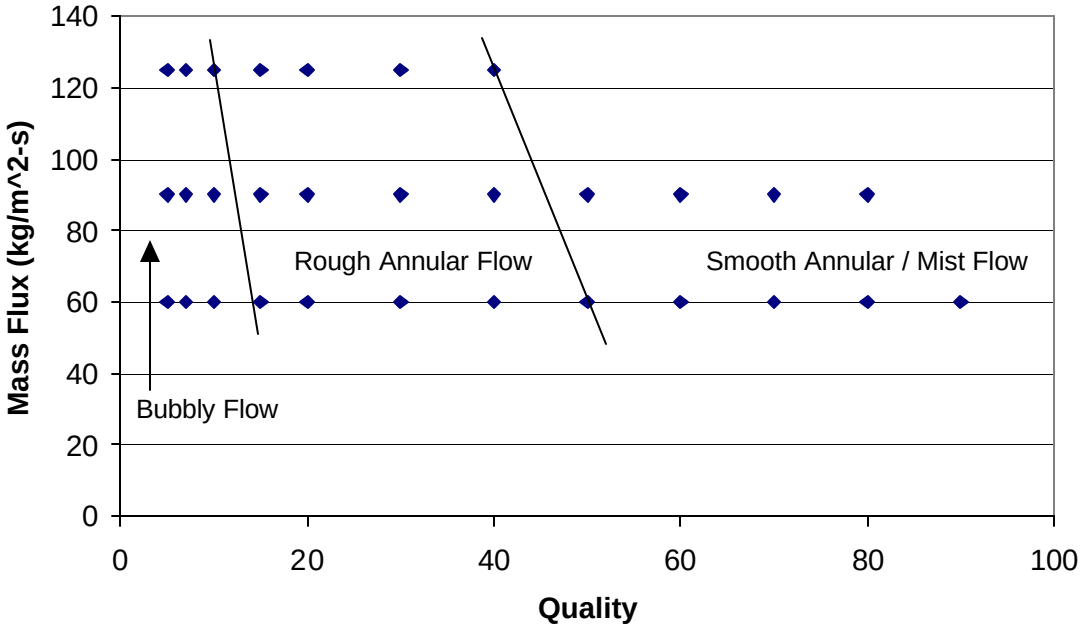

Figure 6.13 Mass Flux Versus Quality Flow Regime Map for the 2:1 Aspect Ratio Bumpy Plate (Adiabatic, Upward Flow, R134a, 10^{o} C)

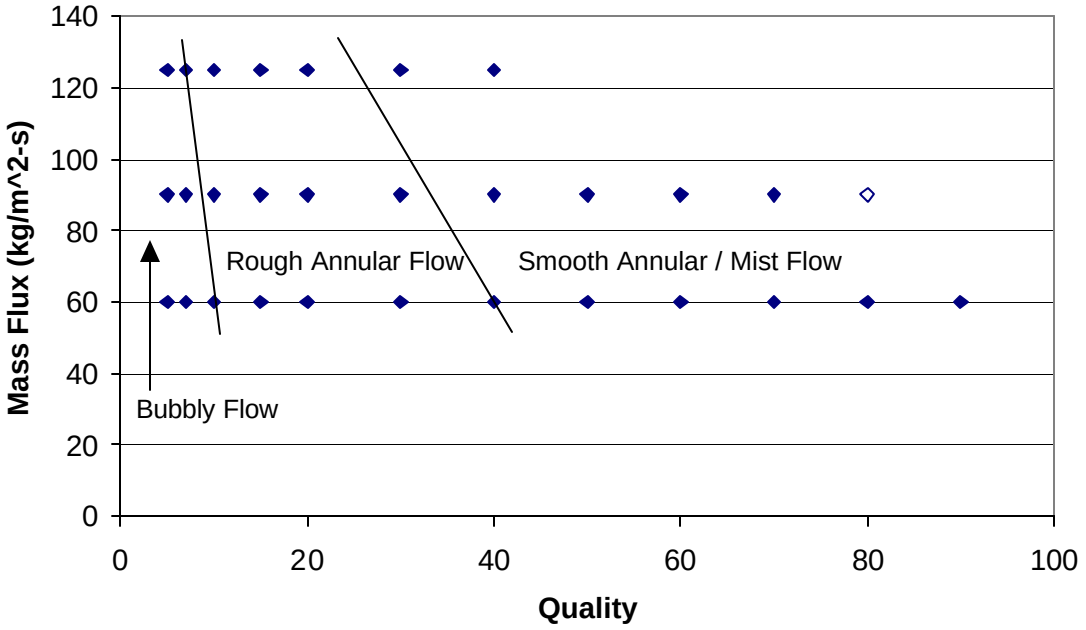

Figure 6.14 Mass Flux Versus Quality Flow Regime Map for the Chevron Plate (Adiabatic, Upward Flow, R134a, 10^{o} C)

Chapter 7: Pressure Drop Predictions

Pressure drop correlations and predictions are investigated in this chapter. The pressure drop data presented in chapter 5 is used to develop and test different single and two-phase pressure drop relations. The friction factor versus Reynolds number relation and pressure drop versus kinetic energy per unit volume relations are used to correlate the single-phase pressure drop data. Furthermore, a numerical and ideal gas model is used to predict pressure drop of vapor refrigerant through the heat exchangers. The Wallis, Carey, and Homogenous void fraction models are tested to see if they can relate the two-phase data to the single-phase data. Modifications to the homogenous model are made in order to obtain a pseudo void fraction that relates the two-phase pressure drop data to the single-phase data for the tested heat exchanger geometries.

7.1 Single-Phase Pressure Drop Correlations

The friction factor versus Reynolds number correlations and pressure drop versus kinetic energy per unit volume were tested to see how well they correlate the single-phase pressure drop data.

7.1.1 Friction Factor Versus Reynolds Number Correlation

Friction factor versus Reynolds number plots were made with the single-phase liquid and vapor data in order to provide a relationship between pressure drop and flow rate for single-phase flow. Figures 7.1 through 7.6 depict the Darcy friction factor versus the Reynolds number for the chevron plate at 10^o C and 20^o C, the 1:1 aspect ratio bumpy plate at 10^o C and 20^o C, and the 2:1 aspect ratio bumpy plate at 10^o C and 20^o C, respectively. The least squares curve fits are seen on each plot. Equations 2.2 and 2.4 define the Darcy friction factor and Reynolds number equations used, respectively. The hydraulic diameter is defined, similar to Mandrusiak and Carey (1988), as four times the test section volume (excluding the headers) divided by the wetted surface area (excluding the headers) and is given in equation 7.1.

$$D_h = \frac{4V_{ts}}{A_w} \tag{7.1}$$

The mass flux is computed using equation 2.5.

$$G = \frac{\dot{m}}{A_m} \tag{2.5}$$

In Figures 7.1 through 7.6, the vapor curves are plotted using the density calculated from the inlet and the exit pressures. The exit pressure curve can be expected to be closer to the true curve because the fluid velocity is the highest at the exit. Therefore, the exit region will dominate in the total pressure drop. It is observed in Figures 7.1 and 7.2 that the single-phase liquid data for the chevron plate geometry falls very close to the experimental data presented by Luo and Zhang (1986) for a similar geometry. The friction factor curve presented by Luo and Yu (1988) show lower values than the ones calculated in this thesis. This can be attributed to the fact that the geometry of the chevron plates presented in Luo and Zhang (1986) is closer to the geometry used in this project. Luo and Yu (1988) rounded the peaks of the chevron grooves which led to a lower pressure drop and hence a lower friction factor. It

can be noted that the liquid and vapor curves in Figures 7.1 through 7.6 do not coincide regardless of whether the inlet or exit pressure is used to define the density in the friction factor definition. Furthermore, the friction factors are orders of magnitude greater than friction factors in round tubes. In addition, the small exponents of the curve fits indicate that there does not seem to be a very strong relation between friction factor and Reynolds number. These factors seem to indicate that wall friction is not the dominant cause of pressure drop in chevron and bumpy style flat plate heat exchangers.

7.1.2 Pressure Drop Versus Kinetic Energy Correlation

The pressure drop of the single-phase liquid and vapor flow is plotted against the kinetic energy per unit volume of the flow in Figures 7.7 through 7.12 for the chevron plate at 10^o C and 20^o C, the1:1 aspect ratio bumpy plate at 10^o C and 20^o C, and the 2:1 aspect ratio bumpy plate at 10^o C and 20^o C, respectively. The gravitational head was subtracted from the pressure drop data. The accelerational effect due to pressure drop was found to be negligible. The kinetic energy per unit volume is defined in equation 7.2.

$$\frac{KE}{Volume} = \frac{G^2}{2r} \tag{7.2}$$

From Figures 7.7 through 7.12 it can be seen that there is a strong linear relationship between the pressure drop and the kinetic energy per unit volume of the flow (all of the R^2 values are above 0.97). Furthermore, it can be observed from these figures that the vapor line which was calculated using the exit density coincide very closely with the liquid curve. This is most likely due to the fact that the velocity is the highest at the exit of the heat exchangers due to the decrease in density resulting from the pressure drop across the plate. This high velocity flow region dominates the pressure drop in the heat exchanger. The least squares curve fits for the 10^o and 20^o C inlet temperatures are, also, very similar for a given geometry. This suggests that inertial effects are the dominant mode of pressure drop in the chevron and bumpy flat plates. The kinetic energy of the flow is decreased when the flow hits the bumps, grooves, and groove ends in the plates.

Single-phase liquid and vapor pressure drop versus kinetic energy per unit volume plots, including 10^o and 20^o C inlet temperatures, can be seen for the chevron plate, the 1:1 aspect ratio bumpy plate, and the 2:1 aspect ratio bumpy plate in Figures 7.13 through 7.15, respectively. The gravitational head was subtracted from the pressure drop data. The exit vapor pressure was used to calculate the density used in the kinetic energy equation. A least squares curve fit, curve fit equation, and the corresponding R^2 value is shown on each plot. These curve fits are later used to predict the two-phase pressure drop.

7.1.2 Vapor Pressure Drop Ideal Gas Model

It is more convenient, at times, to know the pressure drop of a gas based on the inlet pressure instead of the exit pressure. Consequently, two gas models were developed in order to predict the pressure drop of the gas based on the slope of the pressure drop versus kinetic energy curve of the single-phase liquid flow and the inlet pressure. One model utilizes the ideal gas equation of state to approximate the change in density due to pressure drop over the length of the heat exchanger. The other model utilizes numerical integration to account for the change in vapor

density over the length of the heat exchanger. The single-phase liquid pressure drop is plotted versus kinetic energy per unit volume at 10° and 20 ° C inlet temperatures in Figures 7.16 through 7.18 for the chevron, the 1:1 aspect ratio bumpy, and the 2:1 aspect ratio bumpy plates, respectively. The gravitational head was subtracted from the pressure drop data. Least squares curve fits are depicted in each of the plots. The density change is assumed to be negligible for the single-phase liquid flow, therefore, the pressure drop is given by equation 7.3 where the slopes, m, are the slopes of the curve fits in Figures 7.16 through 7.18.

$$\frac{dP}{dx} = \frac{mG^2}{2rL} \tag{7.3}$$

The change in kinetic energy of the gas flow was found to be negligible, and the heat exchangers are insulated. Consequently, the gas models developed assume that the flow has negligible change in kinetic energy, and the flow is adiabatic. As a result, the enthalpy is assumed to be constant, yielding a constant temperature for an ideal gas.

The ideal gas vapor pressure drop model replaces the density in equation 7.3 with the ideal gas approximation given by equation 7.4.

$$r = \frac{P}{RT} \tag{7.4}$$

This yields equation 7.5, an expression for pressure drop per unit length which can be integrated over the length of the heat exchanger.

$$-\frac{dP}{dx} = \frac{mG^2}{2L}\left(\frac{RT}{P}\right) \tag{7.5}$$

Integrating both sides yields equation 7.6, an expression for predicted pressure drop over the entire length of the heat exchanger.

$$\Delta P = P_i - \sqrt{P_i^2 - mRTG^2} \tag{7.6}$$

In the second model, a 100 point (n=100) numerical integration was used to integrate equation 7.3 over the entire length of the heat exchanger. Length increments of, Δx, 1/100th of heat exchanger were used. The density at each integration point was calculated using a constant temperature vapor density versus pressure curve fit derived from Engineering Equation Solver® (EES) (see Figure B.1 for the 10° and 20° C curve fits). Equation 7.7 is the expression used to numerically solve for the total pressure drop.

$$\Delta P = \sum_{i=1}^{n} \frac{mG^2 \Delta x}{2Lr} \tag{7.7}$$

Graphs of the predicted vapor pressure drop versus actual vapor pressure drop for both the ideal gas and the numerical model can be seen in Figures 7.19 through 7.21 for the chevron plate, the 1:1 aspect ratio bumpy plate, and the 2:1 aspect ratio bumpy plate, respectively (10° and 20 ° C inlet temperature conditions are included). From the plots it can be seen that both the ideal gas and the numerical model tend to under-predict the pressure drop. The

greatest under-prediction of pressure drop occurred in the 2:1 aspect ratio bumpy plate, probably because the vapor and liquid pressure drop versus kinetic energy lines did not overlap as well as was found for the other two heat exchangers. The pressure drop predictions for the chevron and the 1:1 aspect ratio bumpy plates were within approximately 20% of the measured pressure drop values. The ideal gas pressure drop predictions are systematically higher than the numerical predictions. These observations can be attributed to the fact that the ideal gas model under-predicts the density of real gases because it does not take into account molecular interactions such as Van der Waal interactions. The lower, predicted, vapor density results in a higher, predicted, kinetic energy and therefore a higher, predicted, pressure drop. The models, perhaps, need to be refined in the future in order to take into account viscous effects to yield more accurate predictions.

7.2 Two-Phase Pressure Drop Predictions

In this section different two-phase pressure drop prediction models, and a new pressure drop model are presented and evaluated for the flat plate heat exchanger geometries tested. The exit density of the liquid and vapor were computed from the two-phase heat exchanger exit pressure using EES curve fits for near 10^o and near 20^o C saturation temperatures shown in Figures B.2 and B.3, respectively.

7.2.1 Wallis and Carey Void Fraction Models

The Wallis and Carey void fraction models (equations 2.16 and 2.17, respectively) were used to compute the kinetic energy of the two-phase flow. The Lockhart-Martinelli parameter was calculated using equation 2.10. The density of the flow can be computed from the void fraction prediction using equation 2.14.

The kinetic energy per unit volume of the flow is then computed using equation 7.2. Figures 7.22 and 7.23 depict the measured pressure drop versus the kinetic energy per unit volume of the flow for the chevron plate at a 10^o C inlet temperature for the Wallis and Carey models, respectively. The gravitational head is subtracted from the measured pressure drop with the corresponding two-phase model density. From these figures it can be seen that both of the models do not collapse the data along the single-phase lines. Both models under-predict the two-phase pressure drop, which means that they both under-predict the void fraction. The plot with the Carey void fraction model prediction, Figure 7.23, collapses the two-phase data well but not along the single-phase line. The Wallis model plot is more widely scattered. The Carey model most likely collapsed the data better than the Wallis model because the Carey model was experimentally determined from a finned plate geometry, similar to the flat plates tested in the experiments presented in this thesis.

7.2.2 Homogenous Void Fraction Model

The homogenous void fraction model was used to compute the kinetic energy of the two-phase flow. This model assumes that the two-phase flow is a homogenous mixture where the liquid and vapor phases are traveling at the same velocity. The homogenous void fraction is found using equation 2.13. The density of the flow is computed from the void fraction prediction using equation 2.14. Equation 7.2 was used to predict the homogenous kinetic energy per unit volume of the flow. Figures 7.24 trough 7.29 depict measured pressure drop versus kinetic energy per unit volume for the chevron plate at 10^o C and 20^o C, the 1:1 aspect ratio bumpy plate at 10^o C and 20^o C, and the 2:1 aspect ratio bumpy plate at 10^o C and 20^o C, respectively. The gravitational head was subtracted from the

measured pressure drop using the homogenous density approximation. From these figures, the homogenous model over-predicts the two-phase pressure drop, which means that it over-predicts the void fraction. Also, it can be seen from these figures that a linear relationship between pressure drop and homogeneous kinetic energy exists in the two-phase flow at a given quality. This further suggests that inertial effects, instead of viscous effects, are the dominant mode of pressure drop in flat plates. Moreover, the two-phase data in Figures 7.24 through 7.29 systematically deviate from the single-phase results based upon quality.

7.2.3 Pseudo Void Fraction Two-Phase Pressure Drop Model

In order to develop a pressure drop model based on the kinetic energy of the flow the two-phase data is correlated to the single-phase data through a model based on quality. A least squares curve fit was made through each quality line in Figures 7.24 through 7.29. The ratio, β, between a pseudo void fraction value and the homogenous void fraction value was found for each quality which would bring the least curve fit for a given quality in line with the least squares curve fit of the single-phase data. Equation 7.8 was used to calculate the value of β from the slope of the single-phase (m_{sp}) and the slope of the two-phase (m_{tp}) least squares curve fits on the pressure drop versus kinetic energy plots.

$$b = \frac{r_l\left(1-\frac{m_{tp}}{m_{sp}}\right)}{\frac{m_{tp}}{m_{sp}}a_{\hom}\left(r_v - r_l\right)} + \frac{m_{sp}}{m_{tp}} \tag{7.8}$$

The 10° and 20° C β values are plotted versus quality for the chevron plate, the 1:1 aspect ratio bumpy plate, and the 2:1 aspect ratio bumpy plate in Figures 7.30 through 7.32, respectively. The β values at 10° and 20° C are close in value, but not identical. The saturation temperature may influence the void fraction, which could explain the differences between the β values at 10° and 20° C. An exponential curve fit was made for each β versus quality plot and can be seen along with the curve fit equations in Figures 7.30 through 7.32. The void fraction should be 0 at a quality of 0 because there is no vapor in the flow. The void fraction at a quality of 1 should be 1 because the flow is all vapor. Therefore, β was forced to 0 at a quality of 0 and β was forced through 1 at a quality of 1. The pseudo void fraction is computed using equation 7.9.

$$a_p = b\,a_{\hom}, \text{ where } b = 1 - e^{(ax^b)} \tag{7.9}$$

The values of the constants a and b are given in Table 7.1.

Table 7.1 β Curve Fit Constants for Chevron and Bumpy Plate Geometries

Geometry	a	b
Chevron Plate	-6.1023	0.5365
1:1 Aspect Ratio Bumpy Plate	-6.3606	0.5207
2:1 Aspect Ratio Bumpy Plate	-5.448	0.4781

The values of the constants are close in value for all three geometries, as seen in table 7.1. It should be noted that the pseudo void fraction values may not reflect the actual void fraction values. The pseudo void fraction was created in order to allow for prediction of the two-phase pressure drop.

The slip ratio, which is defined as the ratio between the vapor and the liquid velocities was calculated from the α_p values obtained. Equation 7.10 was used to calculate the slip ratio, S.

$$S = \frac{v_v}{v_l} = \frac{1 - a_p}{\left(\frac{1-x}{x}\right)\frac{r_v}{r_l}a_p} \tag{7.10}$$

Plots of the slip ratio versus quality are depicted in Figures 7.33 through 7.35 for the chevron, the 1:1 aspect ratio bumpy, and the 2:1 aspect ratio bumpy plates, respectively. In all of the plots, the slip ratio is approximately 2 until a quality of 0.7 is reached. There is a lot of scatter after a quality of 0.7 because small differences in void fraction make large differences in the slip ratio at higher qualities. The 10^o and 20^o C slip ratios seem to agree until a quality of 0.7 is reached.

The pseudo void fraction curve fits made for each heat exchanger geometry are used to predict the two-phase pressure drop of the heat exchangers. Figures 7.36 through 7.41 contain plots of the predicted pressure drop calculated from the pseudo void fraction versus the measured pressure drop (minus the gravitational head) for the chevron plate at 10^o C and 20^o C, the 1:1 aspect ratio bumpy plate at 10^o C and 20^o C, and the 2:1 aspect ratio bumpy plate at 10^o C and 20^o C, respectively. The data seems to fall along the 45^o line and largely falls within the 15% error lines for all of the plots. The pressure model seems to systematically under-predict the pressure drop below measured values of approximately 10 kPa. This under-prediction may be due to the fact that the gravitational head, which was subtracted from the measured pressure drop was an approximation.

7.3 Summary of Uncertainties

The uncertainties of calculated quantities in this thesis were computed using EES. The uncertainties in some of the measurements and computed quantities presented in this thesis are presented in Table 7.2 for representative minimum, maximum, and median flow ranges.

Table 7.2 Uncertainties of Measurements and Calculated Values

		Uncertainties				
G (kg/m^2-s)	Condition	Mass Flow Rate	Mass Flux	Re	Friction Factor	KE
35	liquid	2.2%	2.4%	4.3%	31.1%	4.9%
138	liquid	0.7%	1.2%	3.7%	4.7%	2.3%
303.5	liquid	0.4%	1.0%	3.6%	4.1%	2.1%
16.5	vapor	2.2%	2.4%	4.3%	6.6%	5.5%
26.8	vapor	1.6%	1.9%	4.0%	5.8%	4.6%
46.2	vapor	1.1%	1.5%	3.8%	5.5%	4.2%

The uncertainty in the inlet quality was found to be minimum at a quality of 0.9 (±1.0%), and maximum at a quality of 0.1 (±5.2%).

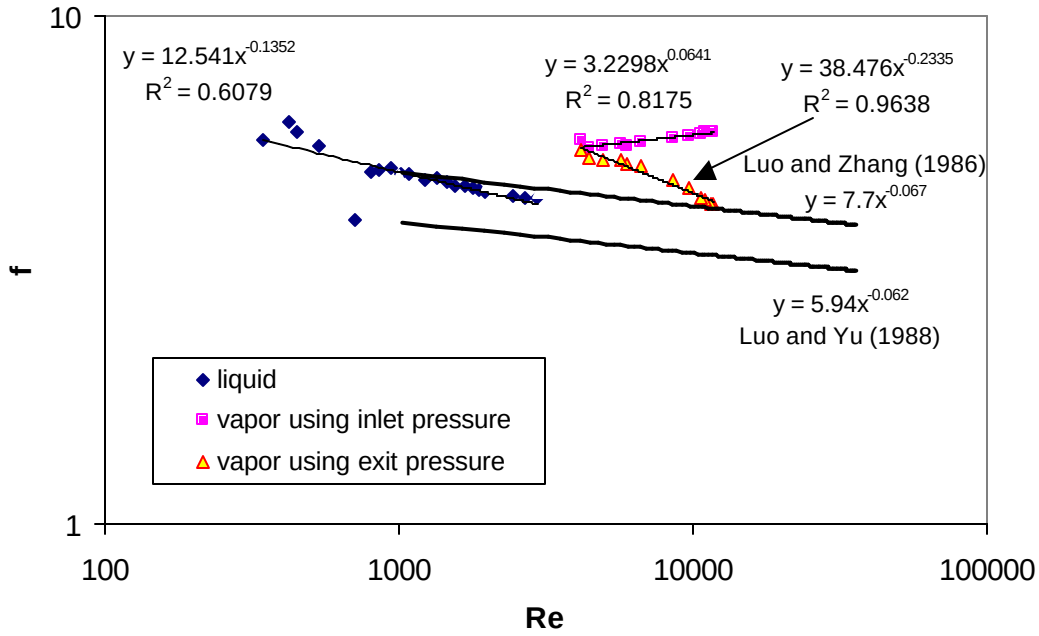

Figure 7.1 Single-Phase Darcy Friction Factor Versus Reynolds Number for Chevron Plate at 10° C Inlet (Adiabatic, Upward Flow, R134a)

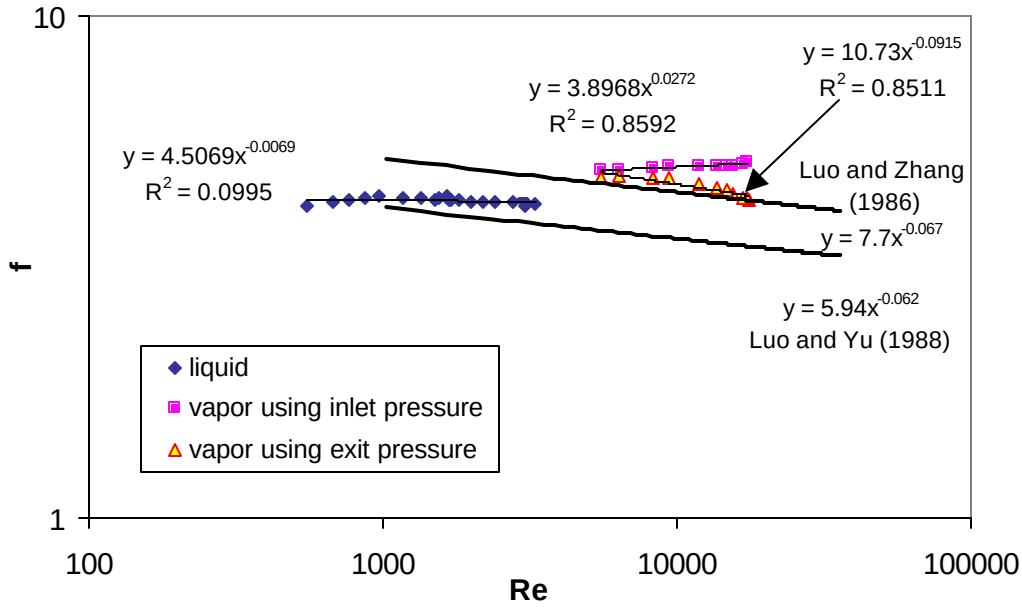

Figure 7.2 Single-Phase Darcy Friction Factor Versus Reynolds Number for Chevron Plate at 20° C Inlet (Adiabatic, Upward Flow, R134a)

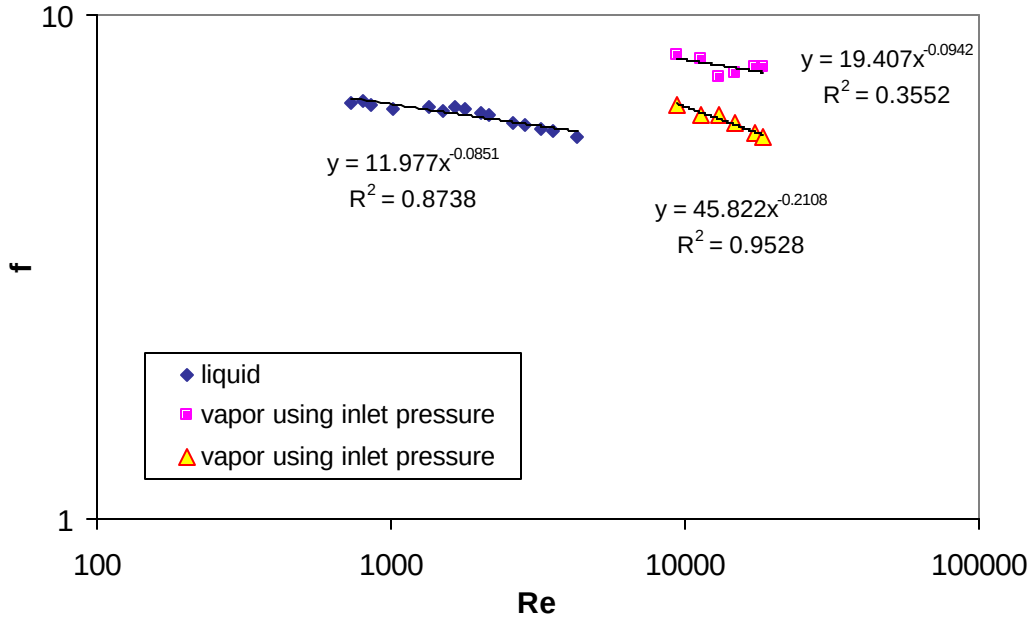

Figure 7.3 Single-Phase Darcy Friction Factor Versus Reynolds Number for 1:1 Aspect Ratio Bumpy Plate at 10° C Inlet (Adiabatic, Upward Flow, R134a)

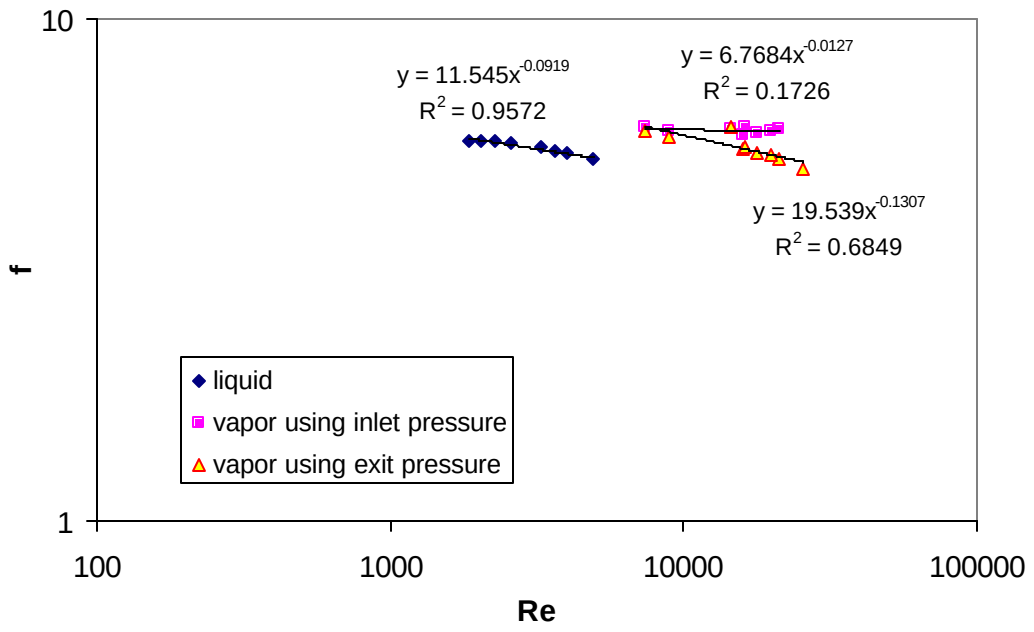

Figure 7.4 Single-Phase Darcy Friction Factor Versus Reynolds Number for 1:1 Aspect Ratio Bumpy Plate at 20° C Inlet (Adiabatic, Upward Flow, R134a)

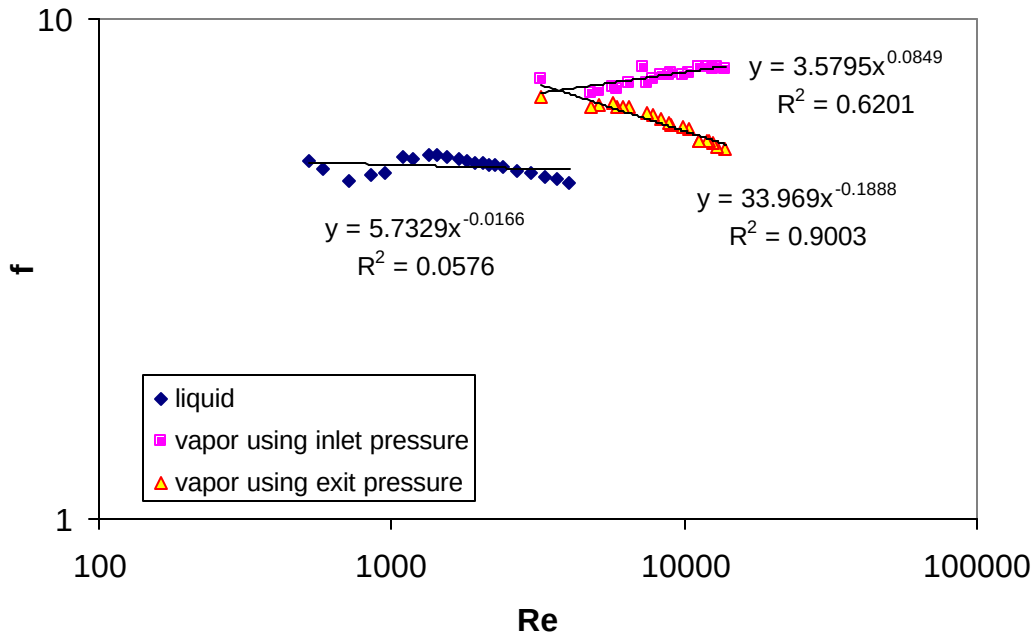

Figure 7.5 Single-Phase Darcy Friction Factor Versus Reynolds Number for 2:1 Aspect Ratio Bumpy Plate at 10° C Inlet (Adiabatic, Upward Flow, R134a)

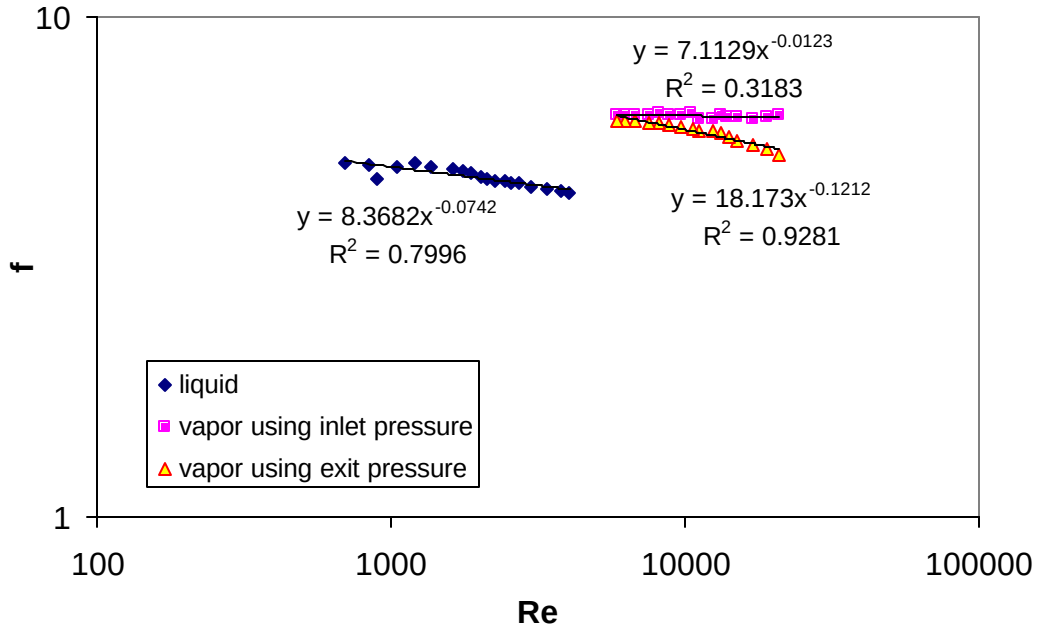

Figure 7.6 Single-Phase Darcy Friction Factor Versus Reynolds Number for 2:1 Aspect Ratio Bumpy Plate at 20° C Inlet (Adiabatic, Upward Flow, R134a)

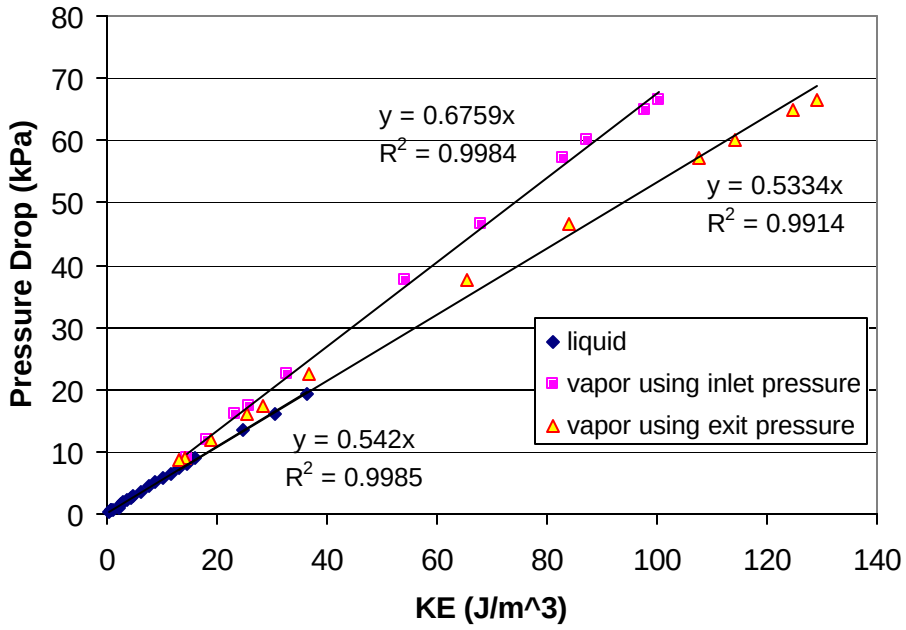

Figure 7.7 Single-Phase Pressure Drop Versus Kinetic Energy Per Unit Volume for Chevron Plate at 10° C Inlet (Adiabatic, Upward Flow, R134a)

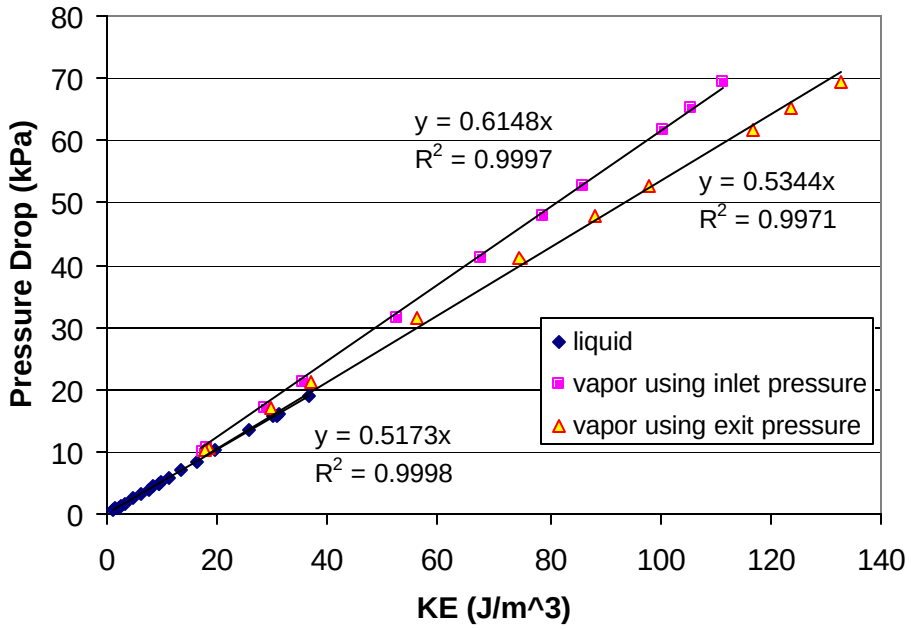

Figure 7.8 Single-Phase Pressure Drop Versus Kinetic Energy Per Unit Volume for Chevron Plate at 20° C Inlet (Adiabatic, Upward Flow, R134a)

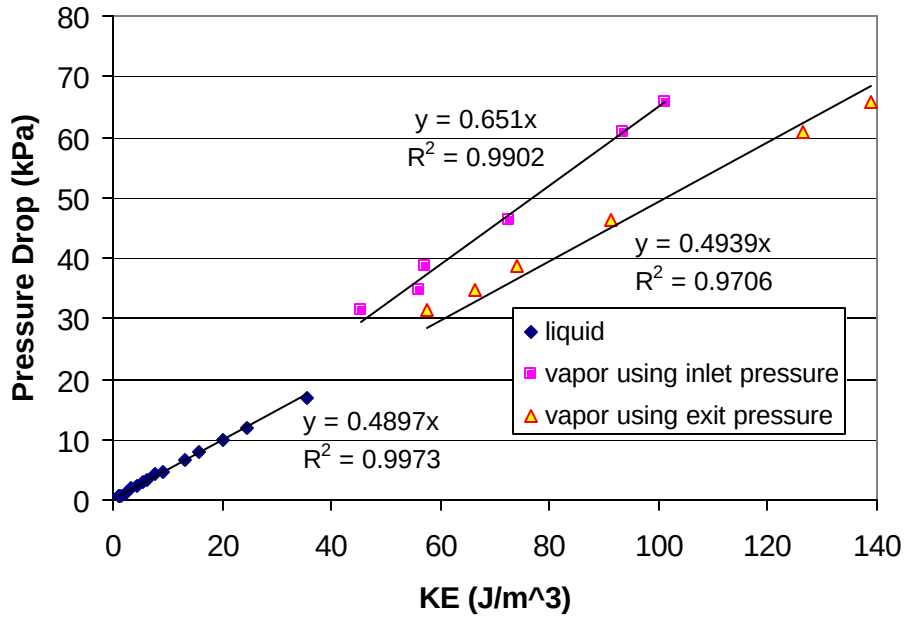

Figure 7.9 Single-Phase Pressure Drop Versus Kinetic Energy Per Unit Volume for 1:1 Aspect Ratio Bumpy Plate at 10° C Inlet (Adiabatic, Upward Flow, R134a)

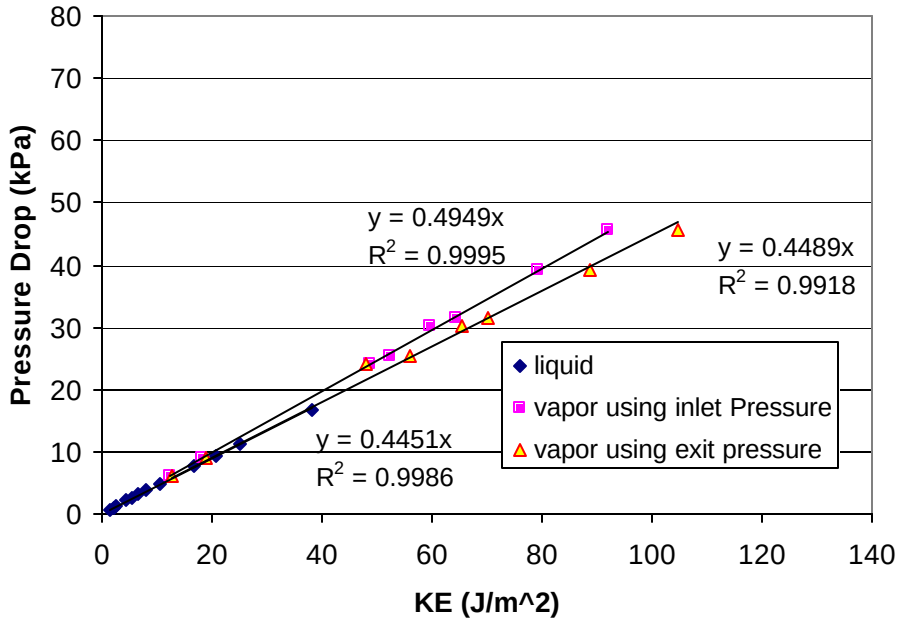

Figure 7.10 Single-Phase Pressure Drop Versus Kinetic Energy Per Unit Volume for 1:1 Aspect Ratio Bumpy Plate at 20° C Inlet (Adiabatic, Upward Flow, R134a)

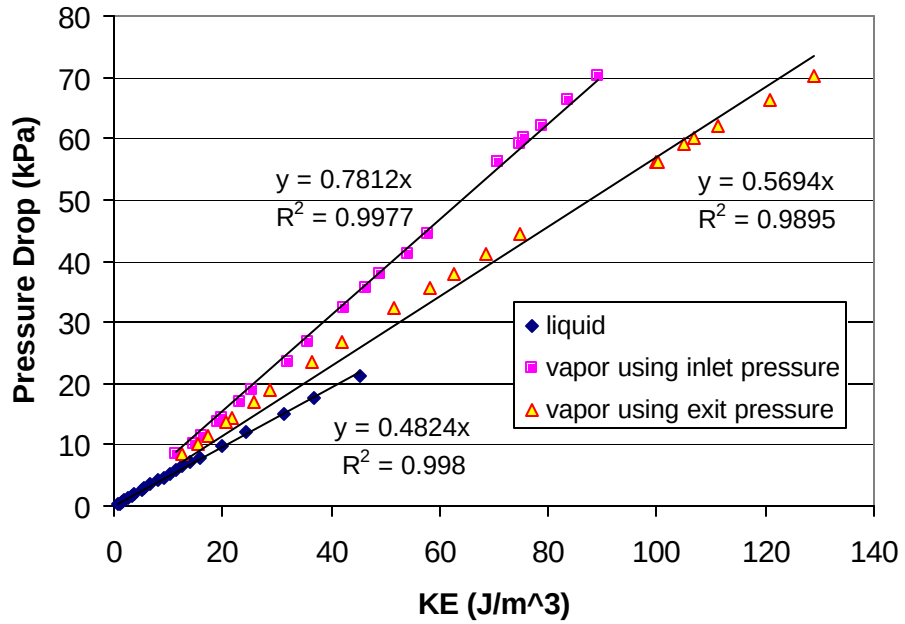

Figure 7.11 Single-Phase Pressure Drop Versus Kinetic Energy Per Unit Volume for 2:1 Aspect Ratio Bumpy Plate at 10° C Inlet (Adiabatic, Upward Flow, R134a)

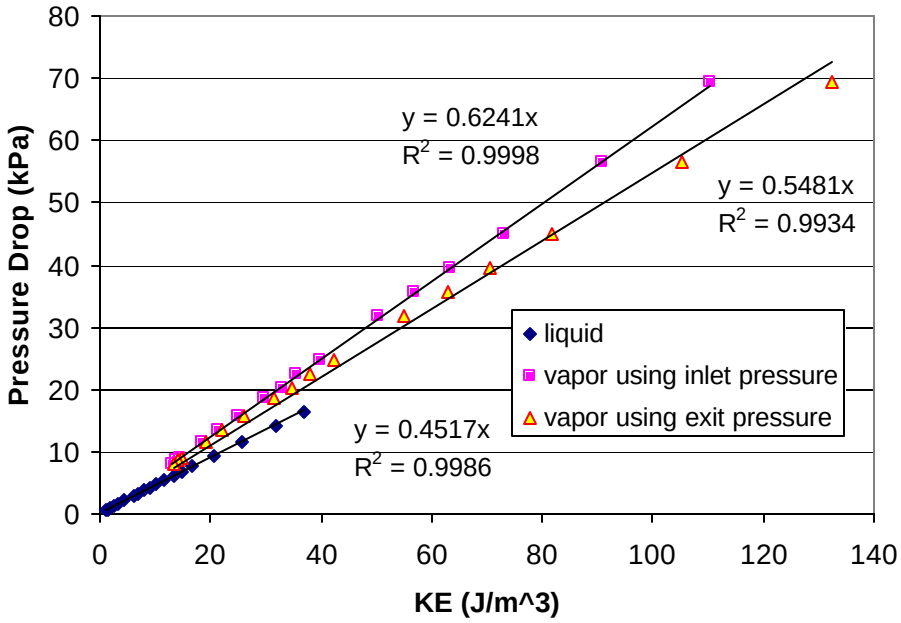

Figure 7.12 Single-Phase Pressure Drop Versus Kinetic Energy Per Unit Volume for 2:1 Aspect Ratio Bumpy Plate at 20° C Inlet (Adiabatic, Upward Flow, R134a)

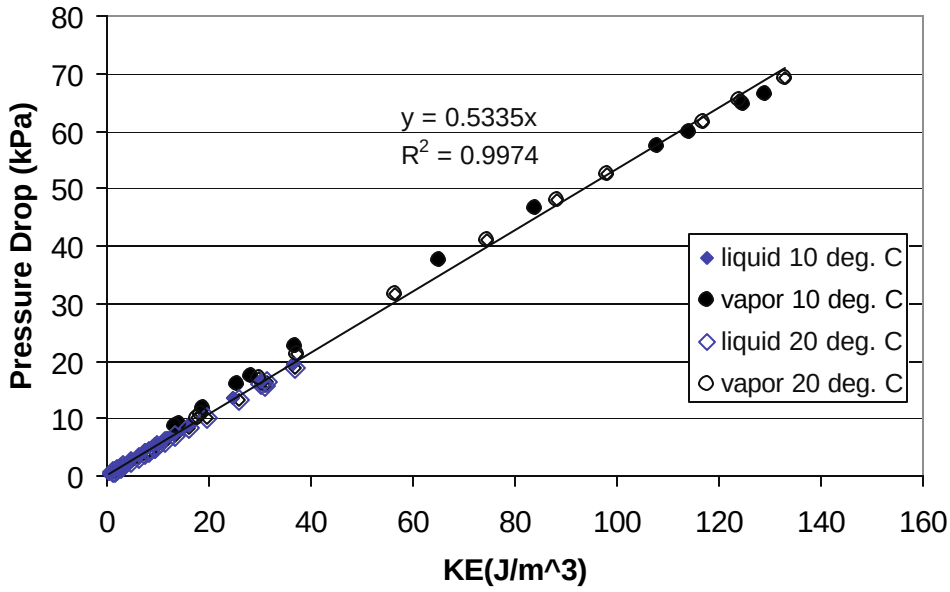

Figure 7.13 Single-Phase Pressure Drop Versus Kinetic Energy Per Unit Volume for Chevron Plate, Using Exit Density for Kinetic Energy (Adiabatic, Upward Flow, R134a)

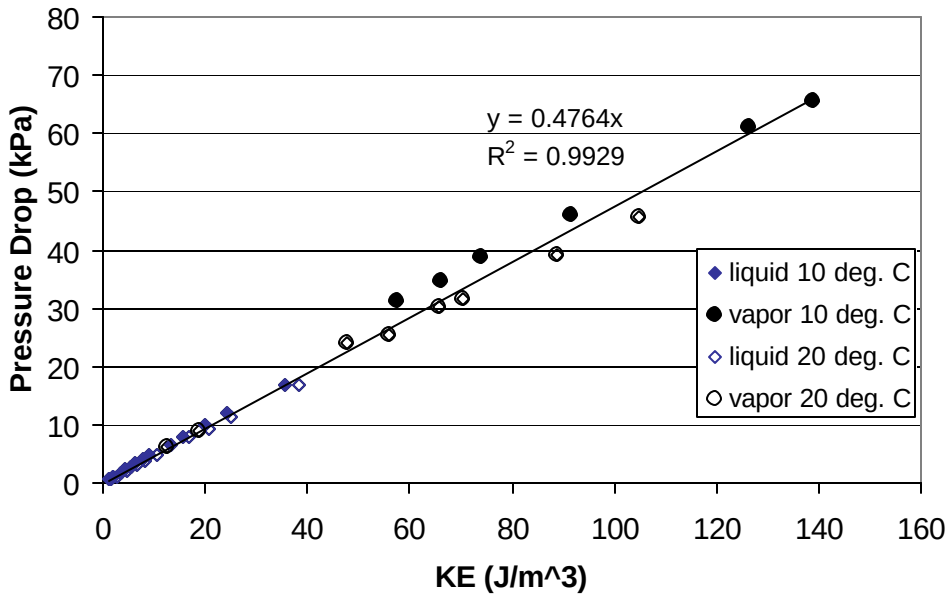

Figure 7.14 Single-Phase Pressure Drop Versus Kinetic Energy Per Unit Volume for 1:1 Aspect Ratio Bumpy Plate, Using Exit Density for Kinetic Energy (Adiabatic, Upward Flow, R134a)

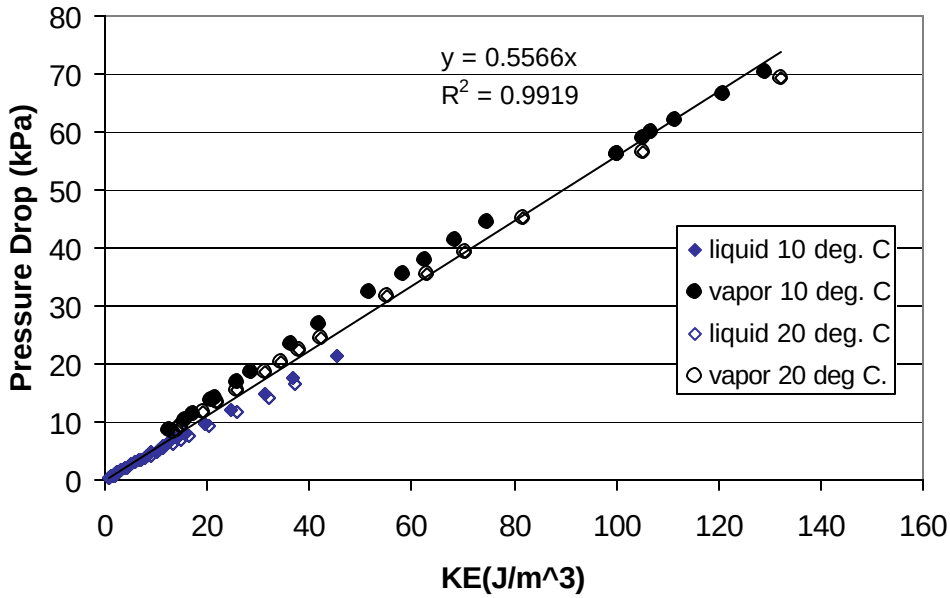

Figure 7.15 Single-Phase Pressure Drop Versus Kinetic Energy Per Unit Volume for 2:1 Aspect Ratio Bumpy Plate, Using Exit Density for Kinetic Energy (Adiabatic, Upward Flow, R134a)

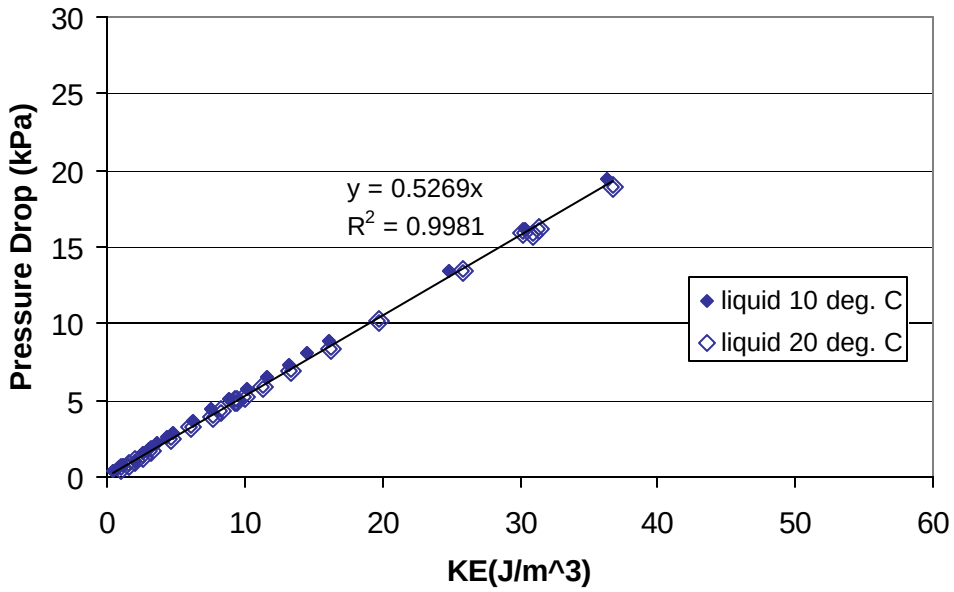

Figure 7.16 Single-Phase Liquid Pressure Drop Versus Kinetic Energy Per Unit Volume for Chevron Plate (Adiabatic, Upward Flow, R134a)

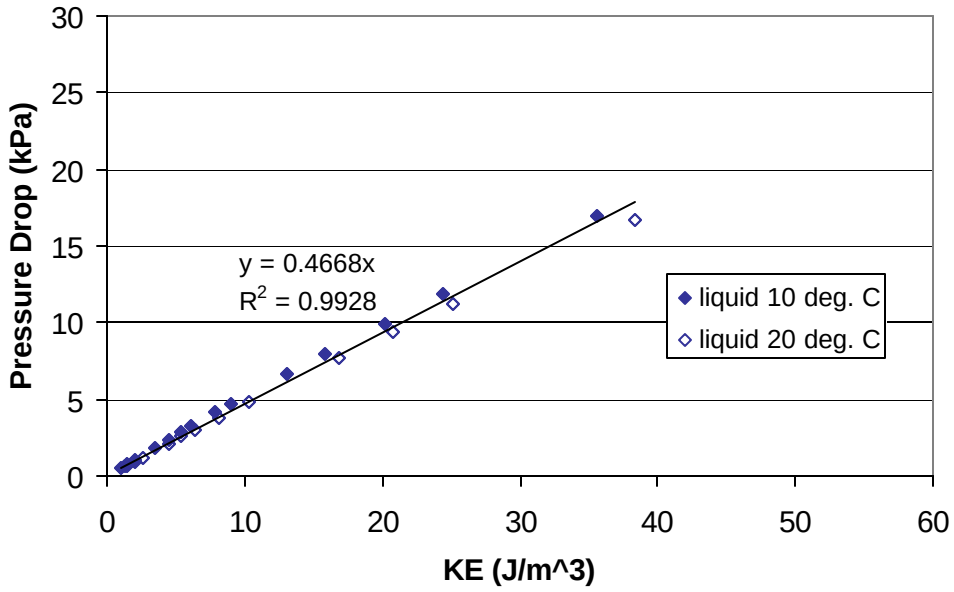

Figure 7.17 Single-Phase Liquid Pressure Drop Versus Kinetic Energy Per Unit Volume for 1:1 Aspect Ratio Bumpy Plate (Adiabatic, Upward Flow, R134a)

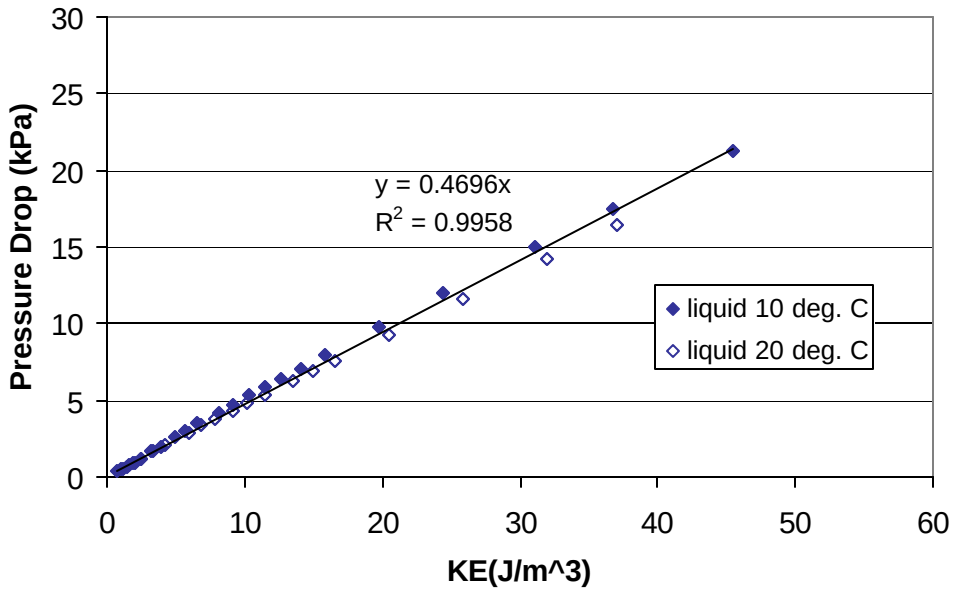

Figure 7.18 Single-Phase Liquid Pressure Drop Versus Kinetic Energy Per Unit Volume for 2:1 Aspect Ratio Bumpy Plate (Adiabatic, Upward Flow, R134a)

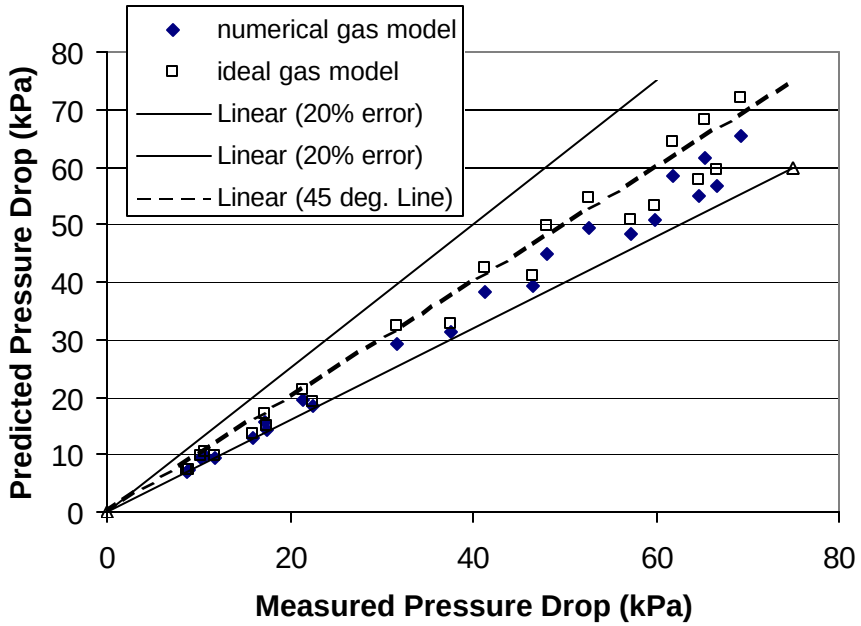

Figure 7.19 Predicted Vapor Pressure Drop Versus Measured Vapor Pressure Drop for Chevron Plate, Using Exit Density for Kinetic Energy (Adiabatic, Upward Flow, R134a)

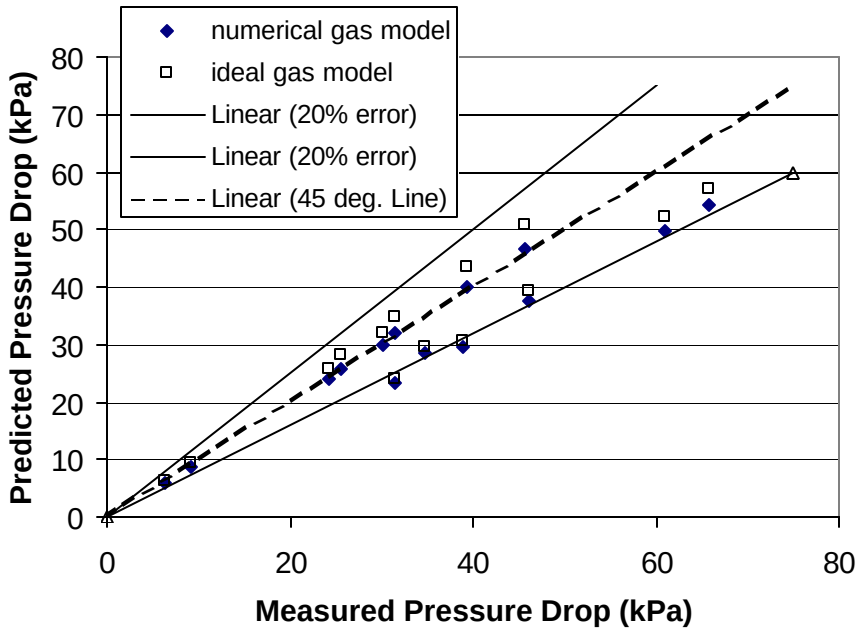

Figure 7.20 Predicted Vapor Pressure Drop Versus Measured Vapor Pressure Drop for 1:1 Aspect Ratio Bumpy Plate, Using Exit Density for Kinetic Energy (Adiabatic, Upward Flow, R134a)

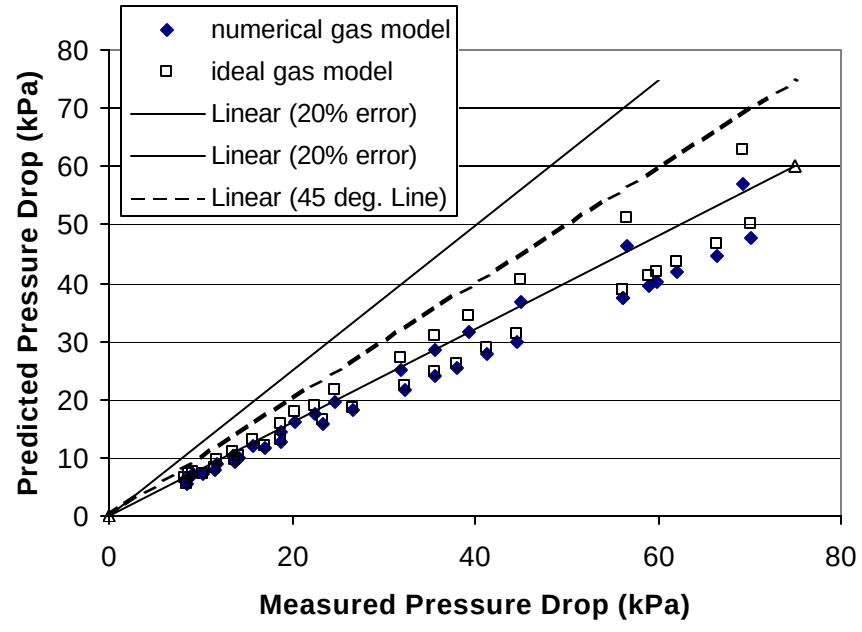

Figure 7.21 Predicted Vapor Pressure Drop Versus Measured Vapor Pressure Drop for 2:1 Aspect Ratio Bumpy Plate, Using Exit Density for Kinetic Energy (Adiabatic, Upward Flow, R134a)

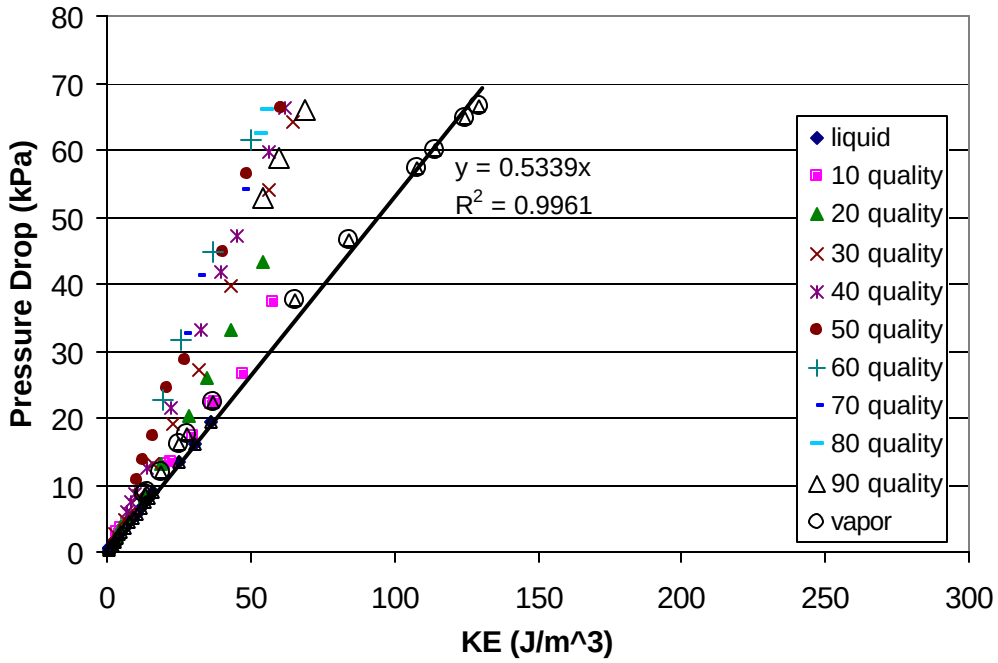

Figure 7.22 Pressure Drop Versus Kinetic Energy Per Unit Volume for Chevron Plate at 10° C Inlet, Using the Wallis Two-Phase Pressure Drop Prediction (Adiabatic, Upward Flow, R134a)

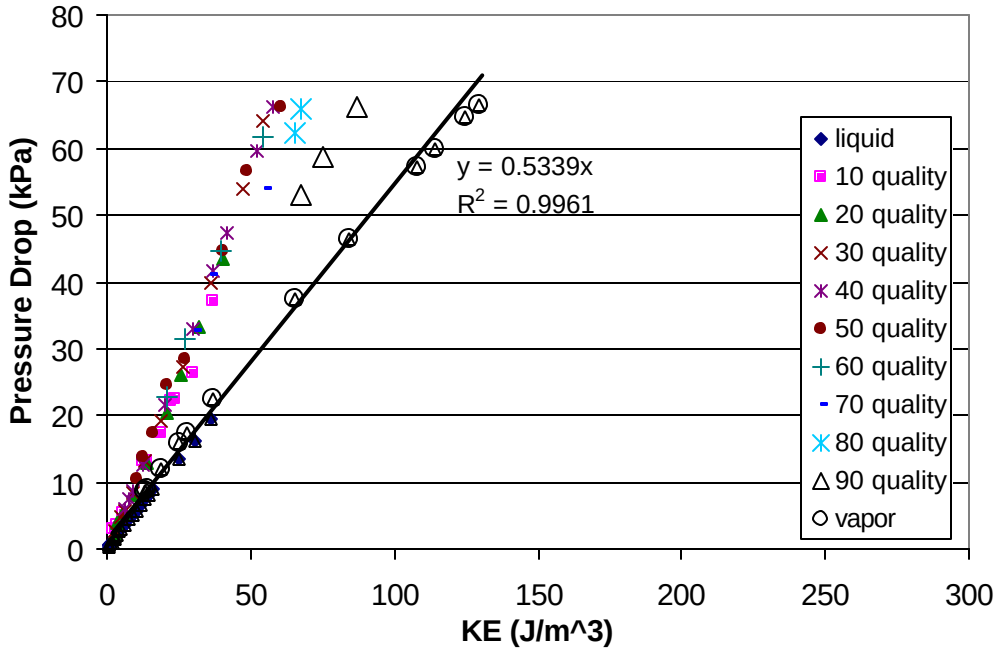

Figure 7.23 Pressure Drop Versus Kinetic Energy Per Unit Volume for Chevron Plate at 10° C Inlet, Using the Carey Void Fraction Prediction (Adiabatic, Upward Flow, R134a)

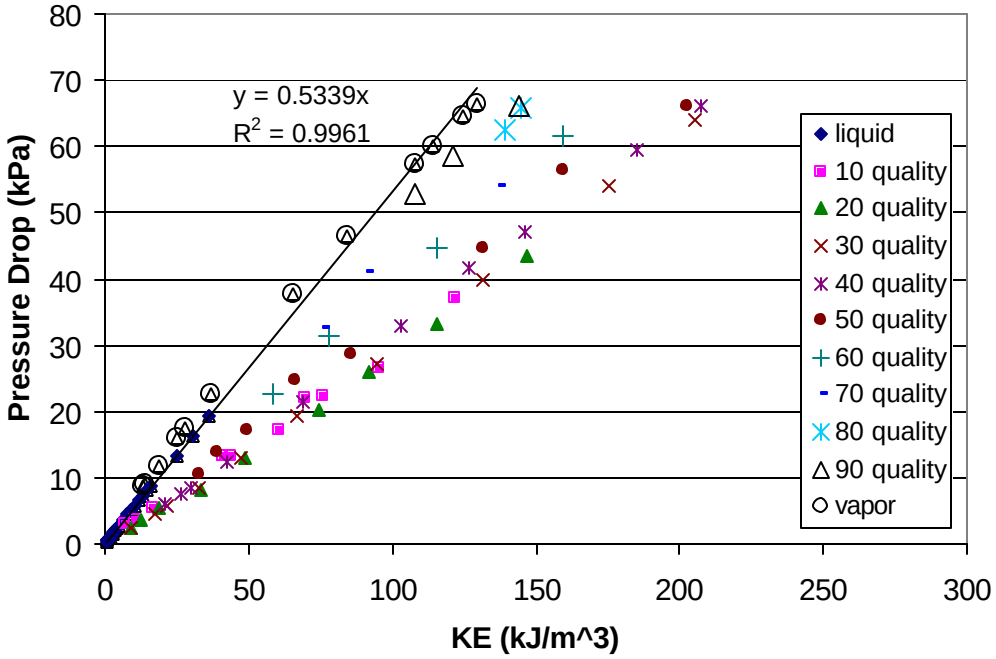

Figure 7.24 Pressure Drop Versus Kinetic Energy Per Unit Volume for Chevron Plate at 10° C Inlet, Using the Homogenous Void Fraction Prediction (Adiabatic, Upward Flow, R134a)

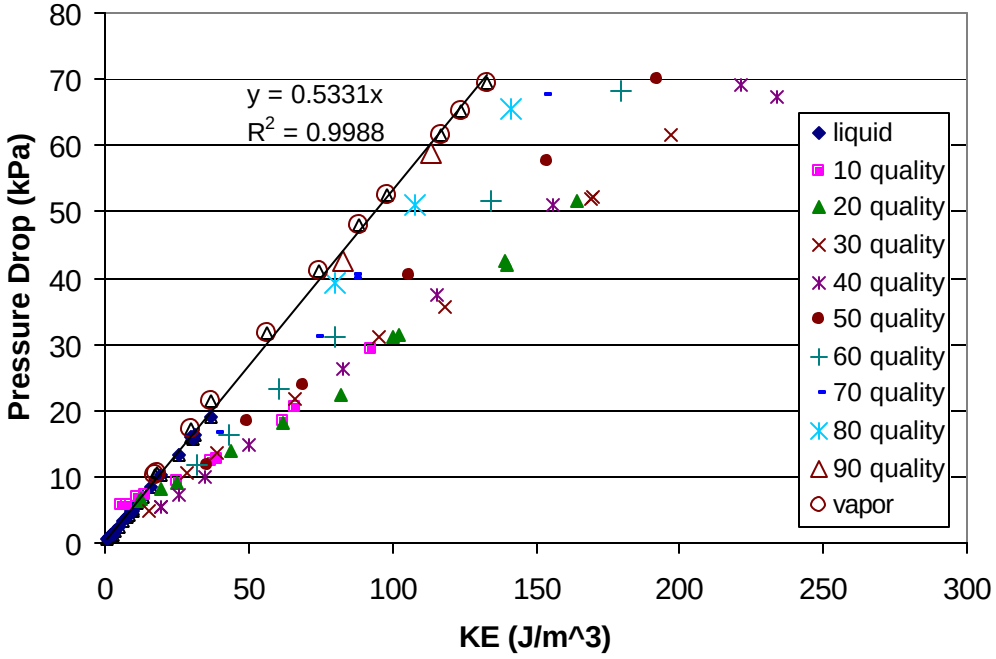

Figure 7.25 Pressure Drop Versus Kinetic Energy Per Unit Volume for Chevron Plate at 20° C Inlet, Using the Homogenous Void Fraction Prediction (Adiabatic, Upward Flow, R134a)

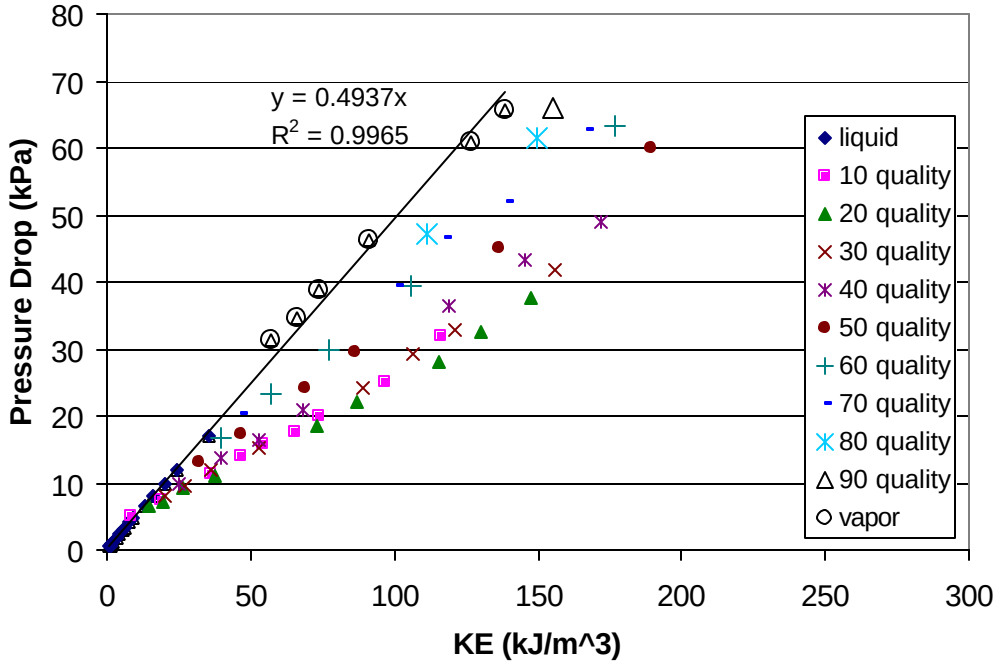

Figure 7.26 Pressure Drop Versus Kinetic Energy Per Unit Volume for 1:1 Aspect Ratio Bumpy Plate at 10° C Inlet, Using the Homogenous Void Fraction Prediction (Adiabatic, Upward Flow, R134a)

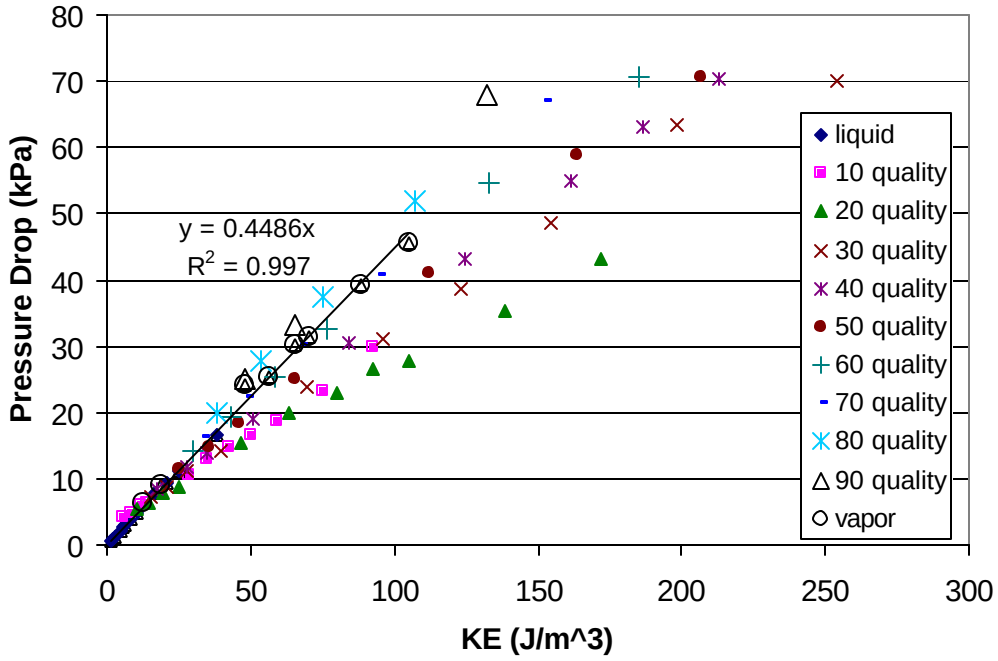

Figure 7.27 Pressure Drop Versus Kinetic Energy Per Unit Volume for 1:1 Aspect Ratio Bumpy Plate at 20° C Inlet, Using the Homogenous Void Fraction Prediction (Adiabatic, Upward Flow, R134a)

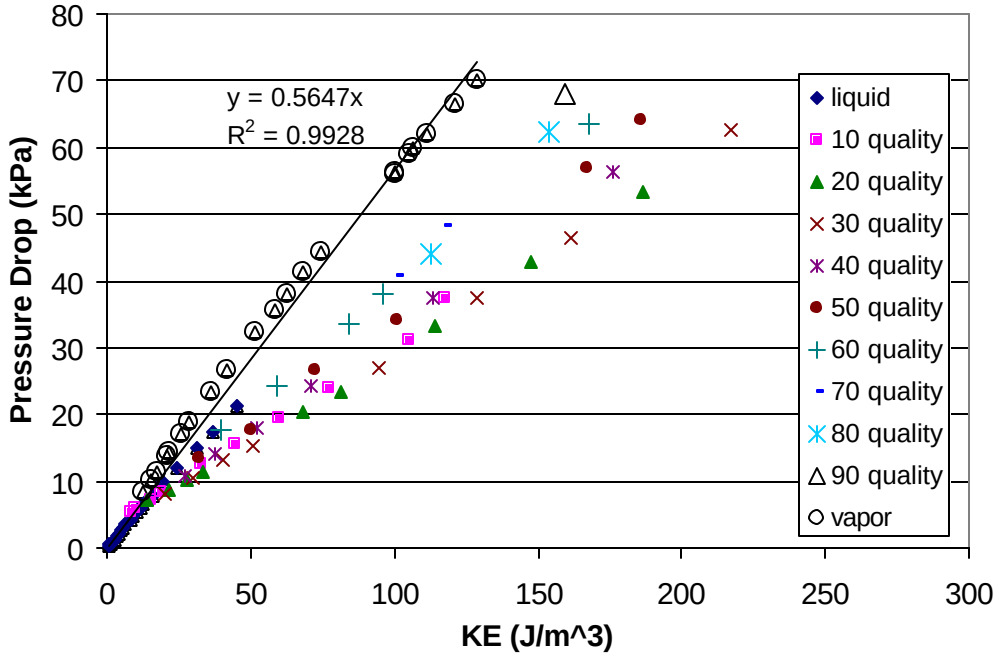

Figure 7.28 Pressure Drop Versus Kinetic Energy Per Unit Volume for 2:1 Aspect Ratio Bumpy Plate at 10° C Inlet, Using the Homogenous Void Fraction Prediction (Adiabatic, Upward Flow, R134a)

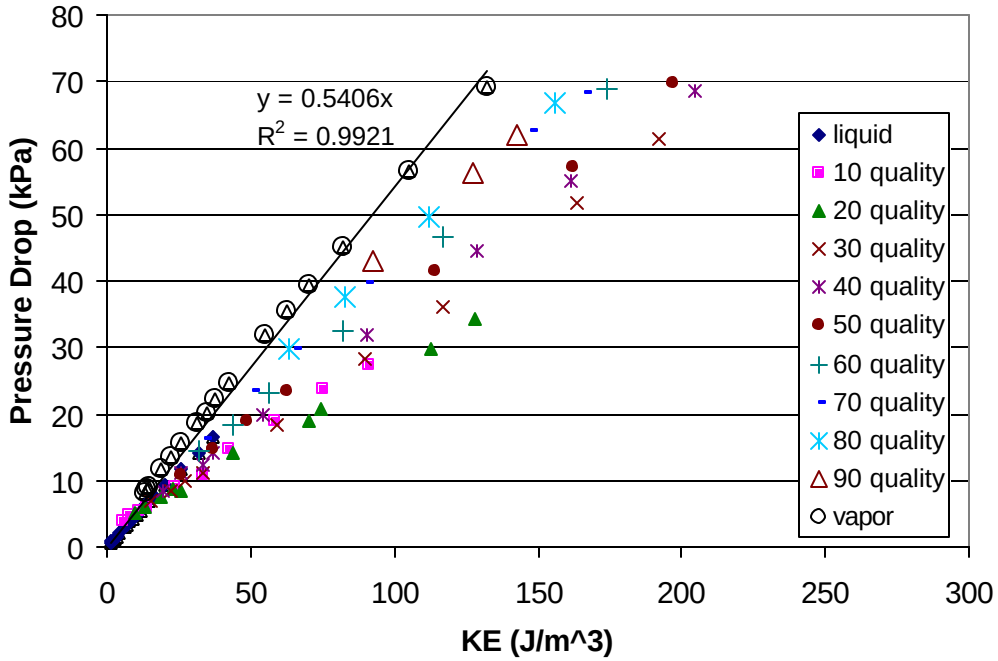

Figure 7.29 Pressure Drop Versus Kinetic Energy Per Unit Volume for 2:1 Aspect Ratio Bumpy Plate at 20° C Inlet, Using the Homogenous Void Fraction Prediction (Adiabatic, Upward Flow, R134a)

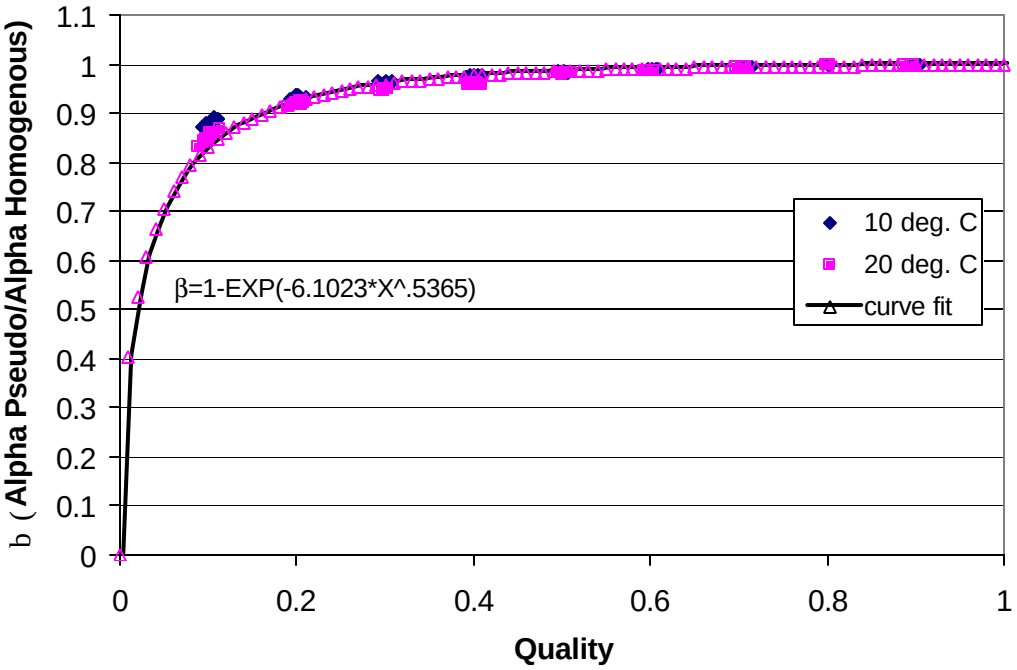

Figure 7.30 Alpha Pseudo/Alpha Homogenous Versus Quality for Chevron Plate (Adiabatic, Upward Flow, R134a)

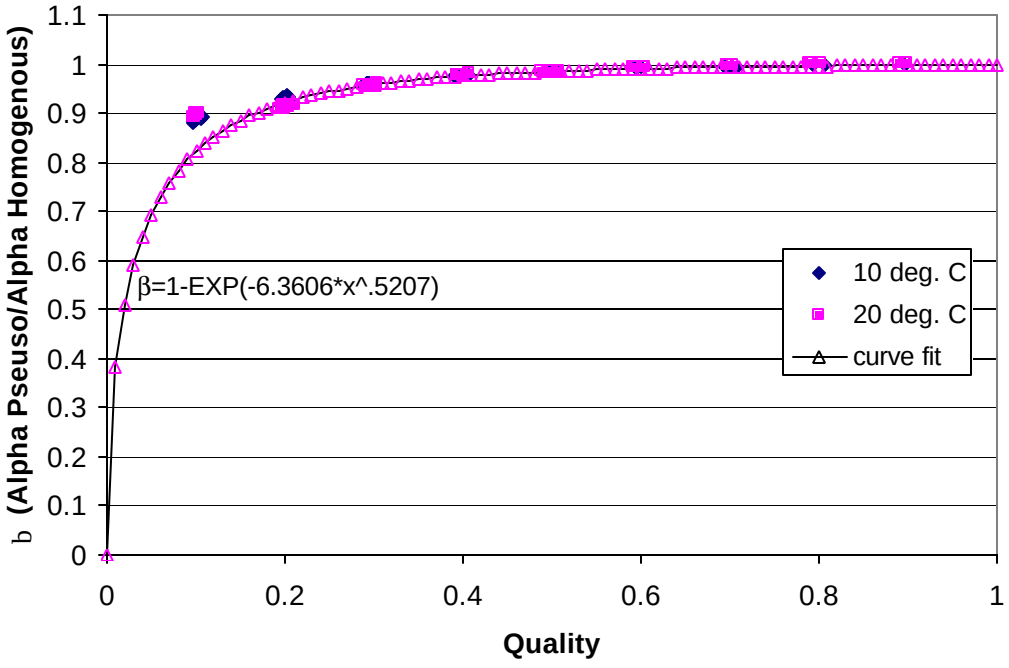

Figure 7.31 Alpha Pseudo/Alpha Homogenous Versus Quality for 1:1 Aspect Ratio Dimpled Plate (Adiabatic, Upward Flow, R134a)

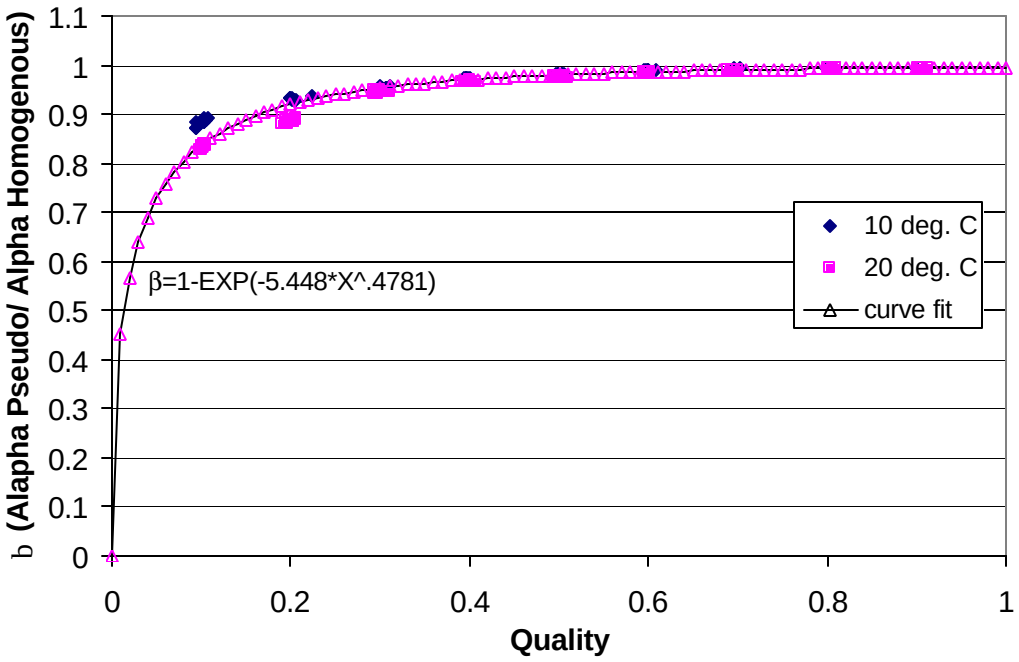

Figure 7.32 Alpha Pseudo/Alpha Homogenous Versus Quality for 2:1 Aspect Ratio Dimpled Plate (Adiabatic, Upward Flow, R134a)

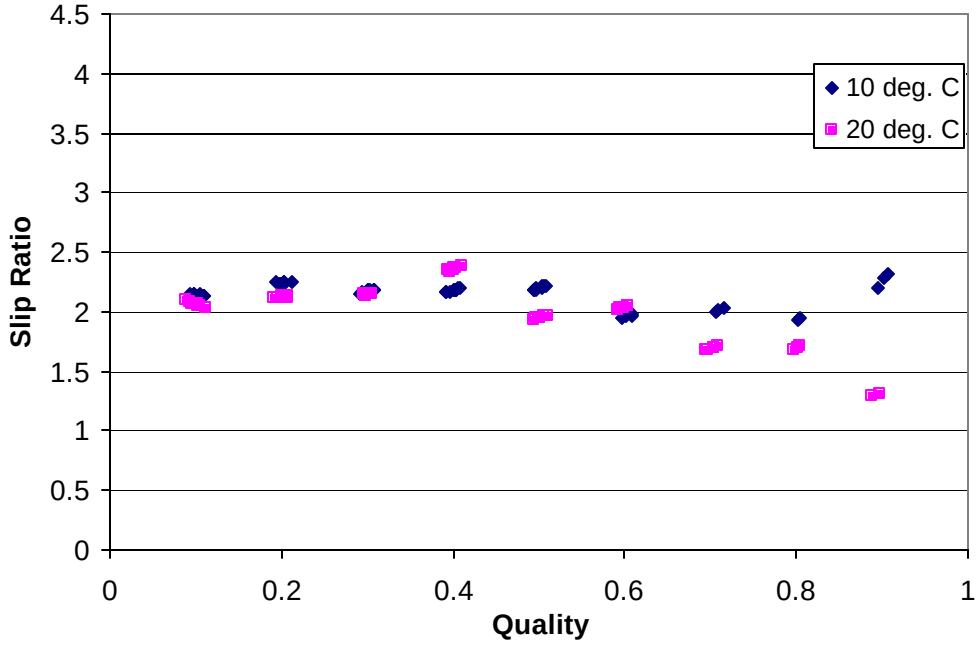

Figure 7.33 Slip Ratio Versus Quality for Chevron Plate (Adiabatic, Upward Flow, R134a)

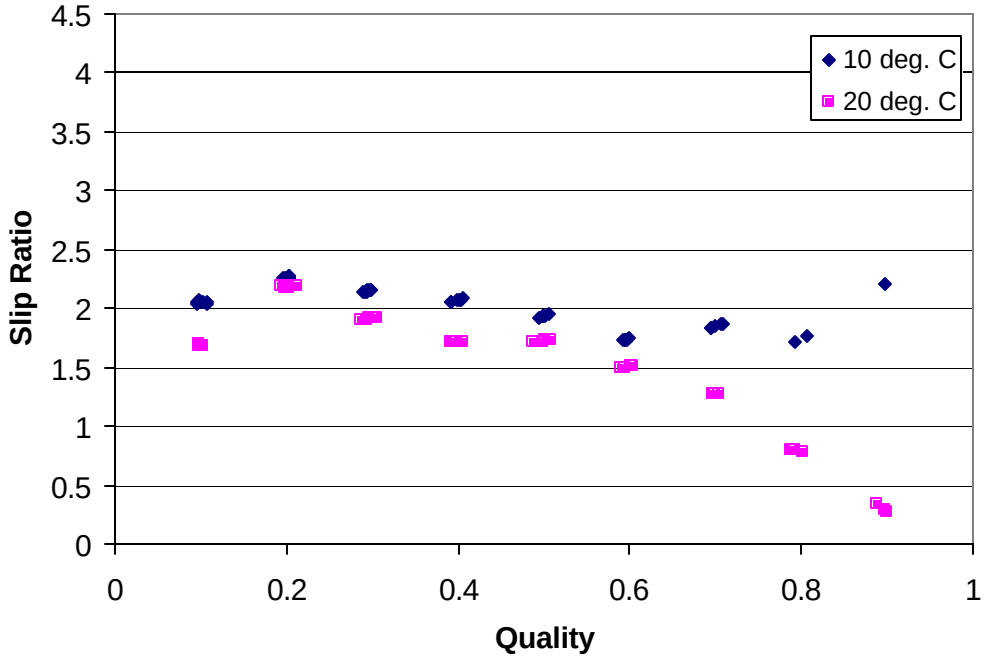

Figure 7.34 Slip Ratio Versus Quality for 1:1 Aspect Ratio Dimpled Plate (Adiabatic, Upward Flow, R134a)

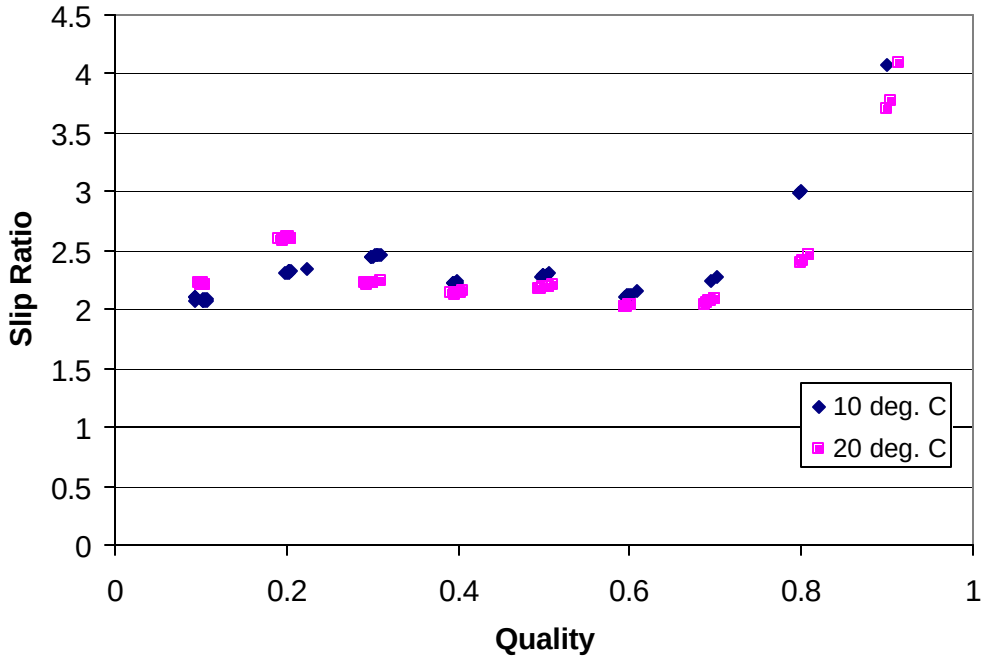

Figure 7.35 Slip Ratio Versus Quality for 2:1 Aspect Ratio Dimpled Plate (Adiabatic, Upward Flow, R134a)

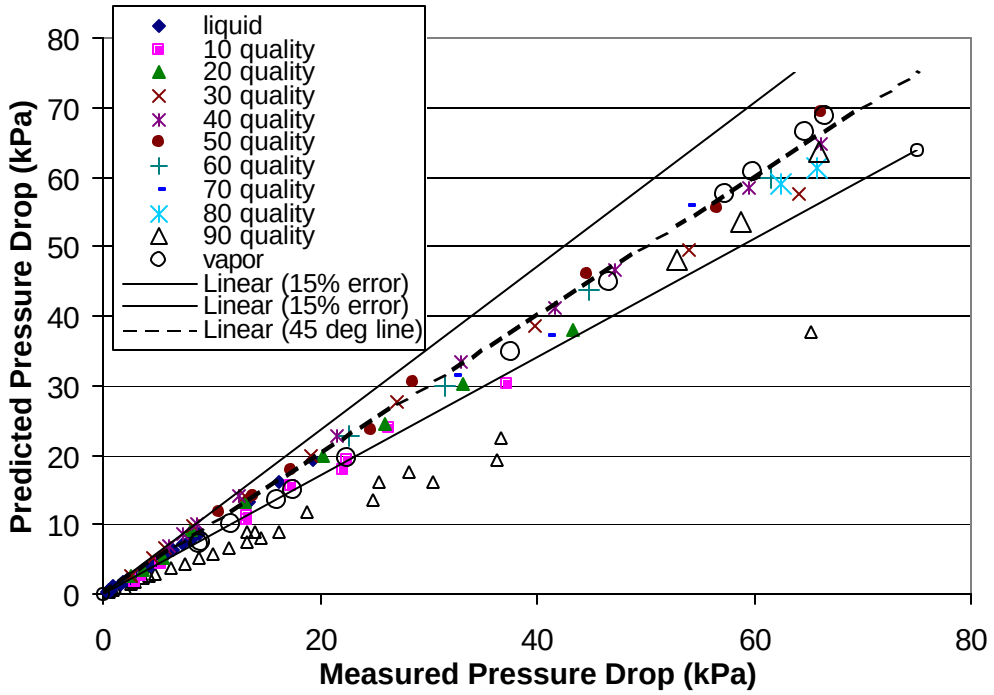

Figure 7.36 Predicted Pressure Drop Versus Measured Pressure Drop for Chevron Plate at 10° C Inlet Temperature (Adiabatic, Upward Flow, R134a)

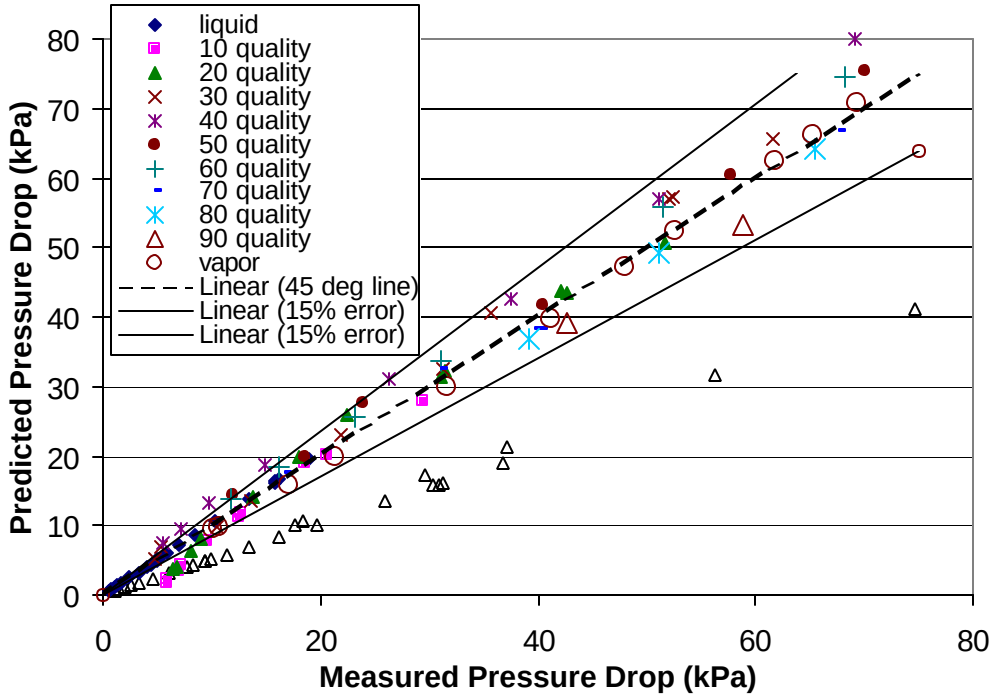

Figure 7.37 Predicted Pressure Drop Versus Measured Pressure Drop for Chevron Plate at 20° C Inlet Temperature (Adiabatic, Upward Flow, R134a)

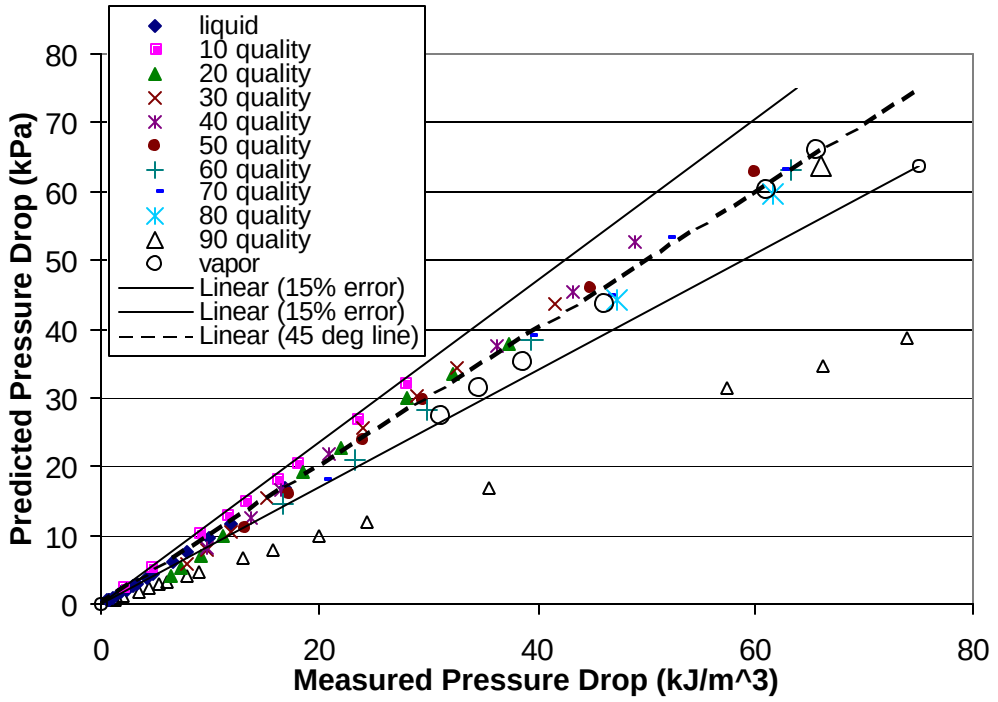

Figure 7.38 Predicted Pressure Drop Versus Measured Pressure Drop for 1:1 Aspect Ratio Dimpled Plate at 10° C Inlet Temperature (Adiabatic, Upward Flow, R134a)

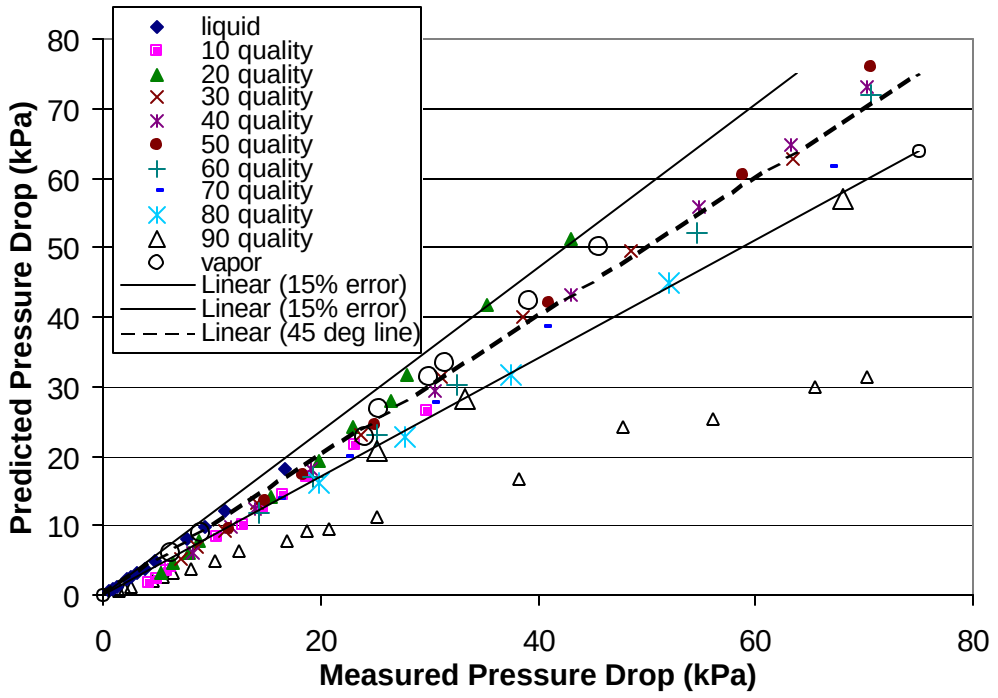

Figure 7.39 Predicted Pressure Drop Versus Measured Pressure Drop for 1:1 Aspect Ratio Dimpled Plate at 20° C Inlet Temperature (Adiabatic, Upward Flow, R134a)

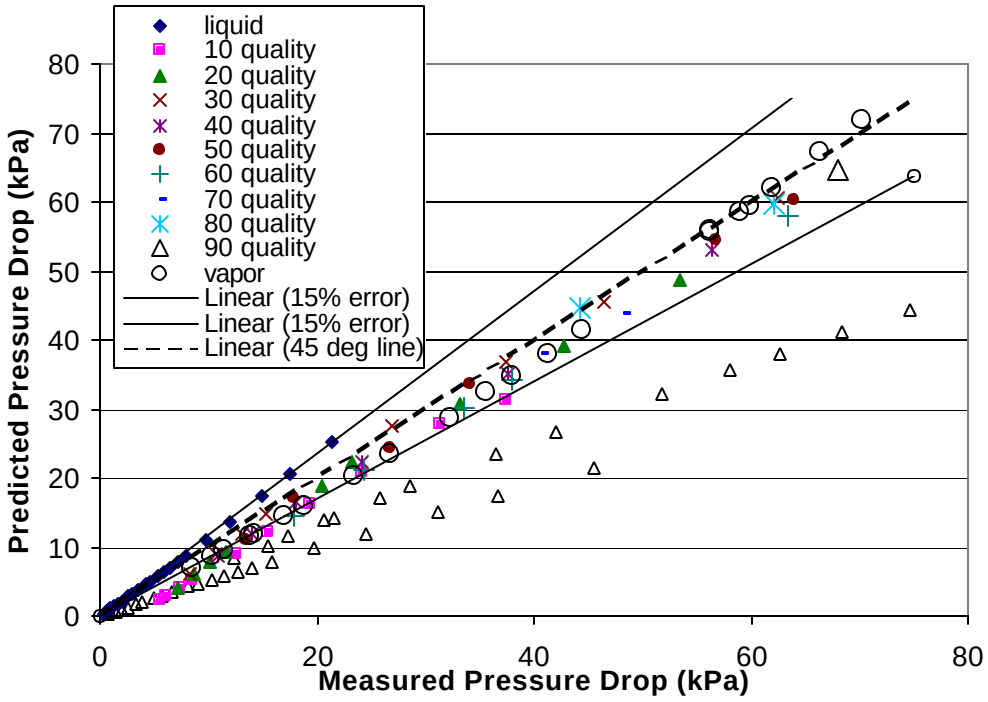

Figure 7.40 Predicted Pressure Drop Versus Measured Pressure Drop for 2:1 Aspect Ratio Dimpled Plate at 10° C Inlet Temperature (Adiabatic, Upward Flow, R134a)

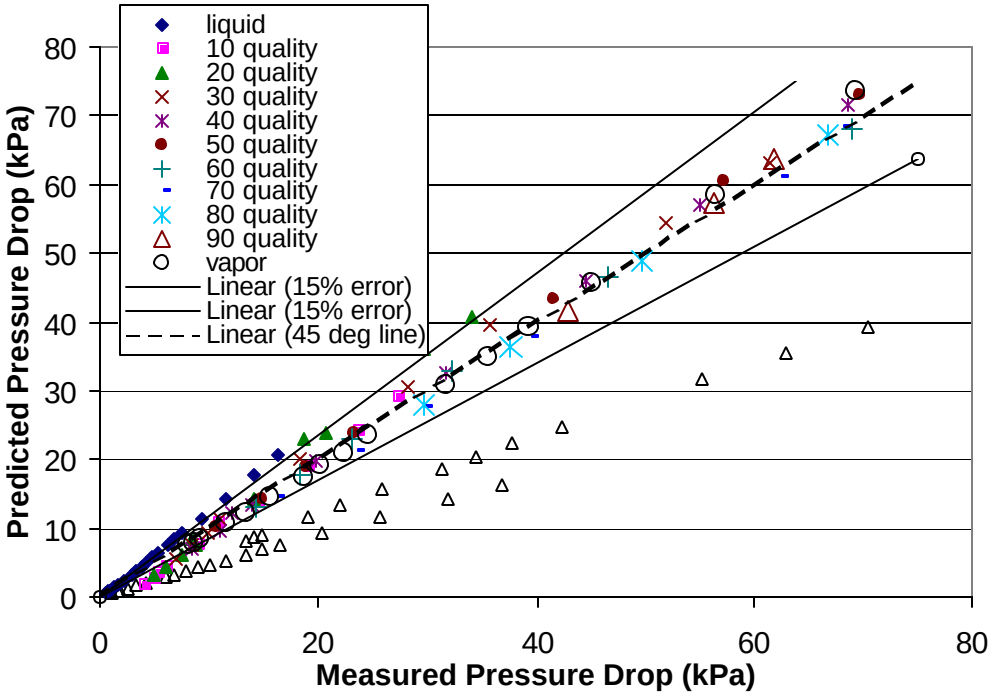

Figure 7.41 Predicted Pressure Drop Versus Measured Pressure Drop for 2:1 Aspect Ratio Dimpled Plate at 20° C Inlet Temperature (Adiabatic, Upward Flow, R134a)

Chapter 8: Conclusion

The evaporator test loop development is now complete. The addition of a liquid refrigerant sub-cooler at the pump inlet solved the pump cavitation problems. The refrigerant-to- refrigerant chiller systems for the sub-cooler and the condenser provide increased control of loop temperature and quality. Through the utilization of the building chilled water, the vapor cooler operates more effectively and does not use any of the capacity of the chillers located in the room. The loop now has the capability to test both flat plate and round tube test sections. Finally, all of the loop instrumentation is now calibrated.

Chevron plate, 1:1 aspect ratio bumpy plate, and 2:1 aspect ratio bumpy plate heat exchangers were constructed in both brass and clear PVC utilizing Pro-E based CNC technology. This technology proves to be very effective in producing new test sections with complicated geometries in a short period of time.

The pressure drop characteristics of the chevron plate, 1:1 aspect ratio bumpy plate, and 2:1 aspect ratio bumpy plate heat exchangers were investigated. The chevron plate was found to have the highest two-phase pressure drop. The 1:1 aspect ratio bumpy plate was found to have the lowest two-phase pressure drop. The 2:1 aspect ratio bumpy plate was found to have two-phase pressure drop values between that of the chevron and the 1:1 aspect ratio bumpy plate. These observations were confirmed on a mass flux and mass flow basis, but the trends were more evident on a mass flow basis.

The two-phase flow characteristics of all three test sections were investigated through flow visualization. Four flow regimes were observed in the heat exchangers: bubbly flow, rough annular flow, smooth annular flow, and mist flow. Annular flow was defined as having a vapor core and liquid boundary layers on all surfaces. The flow regime present was found to depend on quality, mass flux, and plate geometry. Flow regime maps were made for all three geometries on a mass flux versus quality basis. The chevron geometry was found to make flow regime transitions at the lowest mass flux and quality levels. The 1:1 aspect ratio bumpy plate makes flow regime transitions at the highest mass fluxes and qualities. The 2:1 aspect ratio bumpy plate transitions at mass flux and quality levels between that of the chevron and 1:1 aspect ratio bumpy plates. The transition of the chevron plate to the annular flow regimes at the lowest qualities and mass fluxes along with the fact that it has the greatest surface area to volume ratio may indicate that it will have the highest heat transfer associated with it. Heat transfer experiments must be conducted in order to verify this prediction.

Kinetic energy per unit volume was used to characterize the pressure drop of the three flat plate geometries. The kinetic energy per unit volume of the flow was found to have a very strong linear relationship with pressure drop in single-phase flow and two-phase flow at constant qualities. The friction factor versus Reynolds number relation does not seem to be as strong. Therefore, it is concluded that inertial effects, and not viscous effects, dominate the pressure drop in flat plates for both single and two-phase flow.

The vapor pressure drop was found to be dominated by the exit pressure. An ideal gas model and a numerical model based on kinetic energy were used to predict pressure drop from the inlet conditions, a more convenient pressure to find, in single-phase vapor flow. Both models are found to predict the pressure drop within

approximately 20%. In order to further develop the models, viscous effects should also be considered. The Wallis, Carey, and homogenous void fraction models were utilized in order to compute the kinetic energy per unit volume of the two-phase flow in order to correlate it with the single-phase flow.

The Wallis and Carey models under-predict pressure drop, whereas, the homogenous model was found to over-predict pressure drop. This indicates that the Wallis and Carey models under-predict void fraction and the homogenous model over-predicts void fraction. A pseudo void fraction model was developed so that the single-phase and two-phase pressure drop versus kinetic energy data lies along the same line. From the pseudo void fraction models and the slope of the single-phase pressure drop versus kinetic energy line the pressure drop for two-phase flow can be predicted. The model was found to predict the two-phase data within approximately 15%. Experimental void fraction measurements should be found in order to determine whether two-phase interactions play a role in flat plate pressure drop.

Bibliography

Focke, W W. Zachariades, and I.J. Olivier. 1985. “Effect of the Corrugation Inclination Angle on the Thermodydraulic Performance of Plate Heat Exchangers.” *International Journal of Heat & Mass Transfer,* Vol. 28, No. 8, pp. 1469-1479.

Kedzierski, Mark A. 1997. “Effect of Inclination on the Performance of a Compact Brazed Plate Condenser and Evaporator.” *Heat Transfer Engineering,* Vol. 18, No. 3, pp. 25-38.

Lockhart, R.W., and R. C. Martinelli. 1949. "Proposed correlation of data for isothermal two-phase, two-component flow in pipes." *Chemical Engineering Progress*, Vol. 45, No. 1, pp. 39-48.

Luo, Di-an, and Yunlin Yu. 1988. “Heat Transfer, Pressure Drop and Flow Visualization in Two Corrugated Ducts of Different Corrugation Patterns.” *American Society of Mechanical Engineers, Heat Transfer Division, (Publication) HTD,* Vol. 96, pp. 483-488.

Luo, Di-an, and Li Zhang. 1986. “Pressure Drop and Flow Visualization in a Corrugated Duct.” Paper presented at the Annual Meeting of Chinese Engineering Thermophysics, (in Chinese).

Mandrusiak, G.D., V.P. Carey. 1988. “Pressure Drop Characteristics of Two-Phase Flow in a Vertical Channel with Offset Strip Fins” *Experimental Thermal and Fluid Science,* Vol. 1, pp. 41-50.

Manglik, R. M. 1996. “Plate Heat Exchangers for Process Industry Applications: Enhanced Thermal-Hydraulic Characteristics of Chevron Plates.” *Process, Enhanced and Multiphase Heat Transfer*. New York: Begell House, pp. 267-276.

Muley, A., and R.M. Manglik.1999. “Experimental Study of Turbulent Flow Heat Transfer and Pressure Drop in a Plate Heat Exchanger With Chevron Plates.” *Transactions of the ASME Journal of Heat transfer*, Vol. 121, pp.110-117.

Raju, K S N. Bansal, and Jagdish Chand. 1981. “Plate Heat Exchangers and Their Performance Low Reynolds Number Flow Heat Exchangers,” Washington, DC: Hemisphere Publishing Corp., pp. 899-912.

Shah, R. K, and W. W. Focke. 1988. “Plate Heat Exchangers and Their Design Theory.” *Heat Transfer Equipments Design*. Washington, DC: Hemisphere Publishing Corp. pp. 227-254.

Talik, A C. Swanson, L W. Fletcher, and L.S. Anand. 1995. “Heat Transfer and Pressure Drop Characteristics of a Plate Heat Exchanger.” *ASME/JSME Thermal Engineering Joint Conference – Proceedings,* Vol. 4, pp 321-329.

Thonon, B., R. Vidil, and C. Marvillet. 1995. “Recent Research and Developments in Plate Heat Exchangers.” *Journal of Enhanced Heat Transfer,* Vol. 2, pp. 149-155.

Tran, C.C. 2000. “A Study of Refrigerant Void Fraction and Pressure Drop in Return Bends and Development of a New Two-Phase Experimental Apparatus.” M.S. Thesis, University of Illinois.

Wallis, G. B. 1969. *One-Dimensional Two-Phase Flow*. New York: McGraw-Hill, pp. 51-54.

Wang, L K., B. Sunden, and Q.S. Yang. 1999. “Pressure Drop Analysis of Steam Condensation in a Plate Heat Exchanger.” *Heat Transfer Engineering*, Vol. 20, No.1, pp. 71-77.

Yan, Y.-Y., and T.–F. Lin. 1999. “Evaporation Heat Transfer and Pressure Drop of Refrigerant R-134a in a Plate Heat Exchanger.” *Journal of Heat Transfer-Transactions of the ASME,* Vol. 121, No. 1 pp. 118-127.

Yan, Y.-Y., Hsiang-Chao Lio, and Tsing-Fa Lin. 1999. “Condensation Heat Transfer and Pressure Drop of Refrigerant R-134a in a Plate Heat Exchanger.” *International Journal of Heat & Mass Transfer,* Vol. 42, pp. 993-1006.

Appendix A

Table A.1 Chevron Pressure Drop Data at 10° C Inlet (Adiabatic, Upward Flow, R134a)

Avg. Inlet x	Avg. G (kg/m^2-s)	Avg. Pressure Drop (kPa)	Inlet Pressure (kPa)
liquid	35.16	4.77	saturation
liquid	43.37	4.99	saturation
liquid	46.44	5.04	saturation
liquid	54.57	5.23	saturation
liquid	72.59	5.44	saturation
liquid	81.81	6.01	saturation
liquid	87.43	6.26	saturation
liquid	95.93	6.64	saturation
liquid	104.57	7.00	saturation
liquid	110.76	7.30	saturation
liquid	125.74	8.06	saturation
liquid	138.57	8.87	saturation
liquid	149.69	9.50	saturation
liquid	160.17	10.16	saturation
liquid	171.29	10.93	saturation
liquid	183.06	11.81	saturation
liquid	192.11	12.49	saturation
liquid	202.23	13.28	saturation
liquid	250.85	17.87	saturation
liquid	277.45	20.64	saturation
liquid	303.69	23.87	saturation
0.105	194.68	41.72	saturation
0.097	180.31	30.91	saturation
0.093	158.54	26.50	saturation
0.105	157.00	26.94	saturation
0.102	142.48	21.73	saturation
0.098	124.08	17.75	saturation
0.110	114.06	17.72	saturation
0.110	114.06	17.72	saturation
0.098	77.73	9.84	saturation
0.106	57.95	7.99	saturation
0.105	47.59	7.33	saturation
0.199	158.89	47.84	saturation
0.200	142.32	37.71	saturation
0.200	128.21	30.54	saturation
0.203	115.33	24.77	saturation

Table A.1 (Continued)

Avg. Inlet x	Avg. G (kg/m^2-s)	Avg. Pressure Drop (kPa)	Inlet Pressure (kPa)
0.197	95.44	17.47	saturation
0.203	78.59	12.53	saturation
0.211	58.41	9.91	saturation
0.193	50.04	8.20	saturation
0.204	41.04	6.96	saturation
0.301	150.72	68.64	saturation
0.292	142.90	58.45	saturation
0.309	123.01	44.28	saturation
0.294	108.27	31.63	saturation
0.298	91.52	23.66	saturation
0.301	77.17	17.52	saturation
0.300	64.34	12.82	saturation
0.308	51.68	10.13	saturation
0.303	46.75	9.10	saturation
0.308	33.22	6.98	saturation
0.404	130.85	70.64	saturation
0.401	125.30	64.08	saturation
0.396	113.83	51.67	saturation
0.409	105.24	46.17	saturation
0.403	96.50	37.48	saturation
0.406	79.69	26.00	saturation
0.404	63.70	16.92	saturation
0.401	53.68	13.02	saturation
0.391	51.02	11.86	saturation
0.391	45.74	10.50	saturation
0.495	117.20	70.71	saturation
0.502	104.70	61.04	saturation
0.497	97.02	49.16	saturation
0.505	79.24	33.06	saturation
0.495	70.90	29.07	saturation
0.507	60.92	21.75	saturation
0.497	55.16	18.22	saturation
0.503	50.07	15.07	saturation
0.607	94.70	66.08	saturation
0.602	82.72	49.25	saturation
0.598	69.52	35.98	saturation
0.608	60.39	27.12	saturation
0.716	81.86	58.45	saturation

Table A.1 (Continued)

Avg. Inlet x	Avg. G (kg/m^2-s)	Avg. Pressure Drop (kPa)	Inlet Pressure (kPa)
0.709	68.15	45.67	saturation
0.706	63.25	36.98	saturation
0.801	78.38	70.33	saturation
0.804	76.99	66.95	saturation
0.896	73.94	70.57	saturation
0.903	68.14	63.20	saturation
0.906	64.73	57.46	saturation
vapor	46.22	66.57	248.15
vapor	45.58	64.78	247.50
vapor	43.09	59.97	238.89
vapor	42.01	57.35	237.16
vapor	38.05	46.62	235.65
vapor	33.93	37.62	230.52
vapor	26.42	22.56	229.69
vapor	23.40	17.54	228.89
vapor	22.33	16.61	229.59
vapor	19.25	11.90	234.25
vapor	17.20	9.03	244.75
vapor	16.45	8.82	230.13

Table A.2 Chevron Pressure Drop Data at 20^{o} C Inlet (Adiabatic, Upward Flow, R134a)

Avg. Inlet x	Avg. G (kg/m^2-s)	Avg. Pressure Drop (kPa)	Inlet Pressure (kPa)
liquid	300.89	23.18	saturation
liquid	276.08	20.12	saturation
liquid	272.93	20.19	saturation
liquid	277.79	20.52	saturation
liquid	252.56	17.69	saturation
liquid	220.24	14.52	saturation
liquid	199.71	12.72	saturation
liquid	181.25	11.24	saturation
liquid	166.79	10.20	saturation
liquid	156.53	9.50	saturation
liquid	151.62	9.27	saturation
liquid	152.54	9.24	saturation
liquid	137.00	8.28	saturation

Table A.2 (Continued)

Avg. Inlet x	Avg. G (kg/m^2-s)	Avg. Pressure Drop (kPa)	Inlet Pressure (kPa)
liquid	142.50	8.65	saturation
liquid	122.99	7.54	saturation
liquid	106.43	6.73	saturation
liquid	89.06	6.02	saturation
liquid	79.18	5.65	saturation
liquid	70.37	5.36	saturation
liquid	61.80	5.11	saturation
liquid	50.63	4.84	saturation
0.102	201.19	30.17	saturation
0.094	176.80	21.37	saturation
0.112	159.81	19.25	saturation
0.089	135.91	13.40	saturation
0.105	130.22	13.54	saturation
0.098	108.31	10.33	saturation
0.100	80.17	7.94	saturation
0.102	70.11	7.71	saturation
0.104	59.18	6.60	saturation
0.094	50.68	6.67	saturation
0.204	194.28	52.16	saturation
0.204	180.60	43.10	saturation
0.202	182.04	42.49	saturation
0.200	156.14	31.47	saturation
0.203	156.50	31.93	saturation
0.197	143.10	22.82	saturation
0.207	122.08	18.53	saturation
0.208	103.04	14.23	saturation
0.200	79.25	9.47	saturation
0.200	70.43	8.47	saturation
0.191	58.15	7.19	saturation
0.205	53.93	6.91	saturation
0.298	177.36	61.92	saturation
0.303	164.91	52.66	saturation
0.304	164.02	52.32	saturation
0.304	139.35	36.05	saturation
0.302	125.88	31.50	saturation
0.303	105.82	22.15	saturation
0.300	82.39	13.96	saturation
0.295	70.69	10.82	saturation

Table A.2 (Continued)

Avg. Inlet x	Avg. G (kg/m^2-s)	Avg. Pressure Drop (kPa)	Inlet Pressure (kPa)
0.299	58.48	5.73	saturation
0.298	51.86	5.04	saturation
0.397	167.98	67.66	saturation
0.401	162.10	69.38	saturation
0.397	139.13	51.33	saturation
0.398	121.20	37.73	saturation
0.404	102.98	26.48	saturation
0.399	81.47	15.08	saturation
0.401	68.17	10.06	saturation
0.394	58.91	7.42	saturation
0.409	50.65	5.78	saturation
0.500	61.79	12.12	saturation
0.506	71.75	18.71	saturation
0.497	85.15	24.14	saturation
0.495	104.30	40.59	saturation
0.502	122.81	57.89	saturation
0.512	134.42	70.30	saturation
0.603	120.21	68.42	saturation
0.594	106.31	51.68	saturation
0.603	82.95	31.25	saturation
0.597	73.08	23.42	saturation
0.592	62.48	16.41	saturation
0.598	53.87	11.87	saturation
0.709	54.47	16.84	saturation
0.705	73.87	31.31	saturation
0.704	79.78	39.88	saturation
0.698	80.14	40.50	saturation
0.696	103.72	67.83	saturation
0.798	93.42	65.66	saturation
0.804	82.44	51.16	saturation
0.802	71.99	39.27	saturation
0.897	79.43	58.92	saturation
0.887	69.47	42.79	saturation
vapor	71.83	69.38	486.51
vapor	71.38	65.42	504.38
vapor	68.93	61.80	496.00
vapor	63.69	52.68	494.01
vapor	61.23	48.10	499.30

Table A.2 (Continued)

Avg. Inlet x	Avg. G (kg/m^2-s)	Avg. Pressure Drop (kPa)	Inlet Pressure (kPa)
vapor	56.68	41.22	497.89
vapor	48.84	31.70	482.23
vapor	38.96	21.42	457.79
vapor	33.94	17.21	434.62
vapor	25.95	10.74	407.82
vapor	22.46	10.19	326.85

Table A.3 1:1 Aspect Ratio Bumpy Plate Pressure Drop Data at 10^{o} C Inlet (Adiabatic, Upward Flow, R134a)

Avg. Inlet x	Avg. G (kg/m^2-s)	Avg. Pressure Drop (kPa)	Inlet Pressure (kPa)
liquid	300.65	21.38	saturation
liquid	248.52	16.35	saturation
liquid	225.75	14.37	saturation
liquid	199.90	12.37	saturation
liquid	182.20	11.10	saturation
liquid	150.75	9.15	saturation
liquid	140.89	8.58	saturation
liquid	124.64	7.75	saturation
liquid	116.11	7.33	saturation
liquid	105.90	6.81	saturation
liquid	93.55	6.31	saturation
liquid	71.44	5.52	saturation
liquid	59.93	5.21	saturation
liquid	56.60	5.13	saturation
liquid	50.84	5.00	saturation
0.097	199.53	32.69	saturation
0.098	182.90	25.59	saturation
0.096	161.56	20.69	saturation
0.102	149.08	18.33	saturation
0.097	137.94	16.48	saturation
0.099	127.60	14.80	saturation
0.108	108.95	12.09	saturation
0.097	81.53	8.16	saturation
0.106	52.48	5.62	saturation
0.203	159.86	37.93	saturation
0.198	152.93	32.79	saturation

Table A.3 (Continued)

Avg. Inlet x	Avg. G (kg/m^2-s)	Avg. Pressure Drop (kPa)	Inlet Pressure (kPa)
0.203	143.17	28.54	saturation
0.201	125.59	22.49	saturation
0.202	115.37	18.87	saturation
0.204	82.78	11.51	saturation
0.196	71.11	9.50	saturation
0.203	60.29	7.62	saturation
0.204	52.55	6.78	saturation
0.291	137.83	41.88	saturation
0.291	123.18	33.02	saturation
0.294	115.25	29.34	saturation
0.295	105.94	24.41	saturation
0.299	82.02	15.48	saturation
0.288	69.21	12.25	saturation
0.299	58.76	9.90	saturation
0.293	51.61	8.18	saturation
0.391	124.58	49.04	saturation
0.399	114.54	43.42	saturation
0.403	103.90	36.54	saturation
0.401	80.35	21.10	saturation
0.392	71.76	16.67	saturation
0.403	61.47	13.99	saturation
0.406	49.22	9.94	saturation
0.494	114.99	60.13	saturation
0.498	99.13	45.10	saturation
0.500	80.51	29.77	saturation
0.502	72.28	24.27	saturation
0.499	59.88	17.40	saturation
0.505	49.52	13.32	saturation
0.596	101.04	63.40	saturation
0.599	80.56	39.60	saturation
0.593	70.10	30.08	saturation
0.594	60.59	23.46	saturation
0.593	50.92	16.94	saturation
0.695	91.19	62.65	saturation
0.707	83.73	52.07	saturation
0.694	78.13	46.70	saturation
0.708	72.56	39.42	saturation
0.700	50.68	20.47	saturation

Table A.3 (Continued)

Avg. Inlet x	Avg. G (kg/m^2-s)	Avg. Pressure Drop (kPa)	Inlet Pressure (kPa)
0.806	80.41	61.69	saturation
0.792	71.23	47.26	saturation
0.898	77.21	66.08	saturation
vapor	49.29	65.77	257.12
vapor	46.18	61.01	246.38
vapor	39.76	46.19	235.99
vapor	34.95	34.74	236.43
vapor	30.45	38.84	178.66
vapor	25.13	31.38	154.25

Table A.4 1:1 Aspect Ratio Bumpy Plate Pressure Drop Data at 20^{o} C Inlet Temperature (Adiabatic, Upward Flow, R134a)

Avg. Inlet x	Avg. G (kg/m^2-s)	Avg. Pressure Drop (kPa)	Inlet Pressure (kPa)
liquid	307.15	20.99	saturation
liquid	248.90	15.55	saturation
liquid	226.36	13.69	saturation
liquid	203.76	12.06	saturation
liquid	159.64	9.16	saturation
liquid	141.31	8.15	saturation
liquid	125.97	7.36	saturation
liquid	115.46	6.88	saturation
liquid	105.50	6.42	saturation
liquid	79.80	5.50	saturation
liquid	71.73	5.25	saturation
liquid	59.12	4.90	saturation
0.100	202.61	30.63	saturation
0.101	183.34	24.05	saturation
0.102	161.59	19.57	saturation
0.100	150.69	17.43	saturation
0.099	139.50	15.51	saturation
0.101	125.42	13.67	saturation
0.100	114.08	11.37	saturation
0.103	79.53	7.13	saturation
0.097	73.76	6.79	saturation
0.101	60.89	5.77	saturation
0.098	52.19	5.13	saturation

Table A.4 (Continued)

Avg. Inlet x	Avg. G (kg/m^2-s)	Avg. Pressure Drop (kPa)	Inlet Pressure (kPa)
0.198	203.65	43.57	saturation
0.204	181.38	35.84	saturation
0.201	159.82	28.33	saturation
0.198	151.18	26.97	saturation
0.201	140.01	23.45	saturation
0.202	124.53	20.28	saturation
0.204	107.00	15.98	saturation
0.194	80.83	9.29	saturation
0.199	70.44	8.27	saturation
0.199	61.20	6.84	saturation
0.212	50.19	5.74	saturation
0.303	198.23	70.48	saturation
0.288	180.69	63.72	saturation
0.294	159.96	48.91	saturation
0.300	142.53	38.99	saturation
0.300	126.70	31.42	saturation
0.304	107.89	24.03	saturation
0.302	82.52	14.55	saturation
0.301	69.19	11.46	saturation
0.302	59.79	9.02	saturation
0.297	52.16	7.44	saturation
0.394	160.50	70.48	saturation
0.406	148.99	63.48	saturation
0.397	140.96	55.06	saturation
0.394	125.66	43.37	saturation
0.395	104.27	30.80	saturation
0.400	81.50	19.33	saturation
0.392	68.31	14.26	saturation
0.392	61.11	11.99	saturation
0.394	48.39	8.59	saturation
0.500	140.85	70.74	saturation
0.498	126.94	58.98	saturation
0.507	106.01	41.15	saturation
0.499	82.81	25.17	saturation
0.488	70.55	18.58	saturation
0.499	61.67	15.07	saturation
0.502	51.87	11.69	saturation

Table A.4 (Continued)

Avg. Inlet x	Avg. G (kg/m^2-s)	Avg. Pressure Drop (kPa)	Inlet Pressure (kPa)
0.602	121.98	70.71	saturation
0.602	104.94	54.77	saturation
0.604	81.18	32.79	saturation
0.594	71.89	25.44	saturation
0.594	62.15	19.52	saturation
0.591	52.22	14.49	saturation
0.697	103.32	67.16	saturation
0.699	83.41	40.84	saturation
0.697	71.30	30.45	saturation
0.697	60.74	22.55	saturation
0.703	50.37	16.38	saturation
0.793	82.61	52.18	saturation
0.791	70.11	37.69	saturation
0.803	59.45	27.86	saturation
0.788	50.80	20.04	saturation
0.899	85.09	68.09	saturation
0.897	61.73	33.39	saturation
0.889	53.56	25.31	saturation
vapor	59.20	45.73	410.37
vapor	55.46	39.25	415.93
vapor	49.87	31.54	415.38
vapor	44.89	25.49	414.54
vapor	45.38	30.11	374.58
vapor	40.74	24.20	371.76
vapor	25.15	9.14	375.63
vapor	20.73	6.26	378.02

Table A.5 2:1 Aspect Ratio Bumpy Plate Pressure Drop Data at 10^{o} C Inlet Temperature (Adiabatic, Upward Flow, R134a)

Avg. Inlet x	Avg. G (kg/m^2-s)	Avg. Pressure Drop (kPa)	Inlet Pressure (kPa)
liquid	339.69	25.75	saturation
liquid	305.09	21.91	saturation
liquid	280.95	19.40	saturation
liquid	248.94	16.37	saturation
liquid	223.55	14.18	saturation
liquid	199.93	12.33	saturation

Table A.5 (Continued)

Avg. Inlet x	Avg. G (kg/m^2-s)	Avg. Pressure Drop (kPa)	Inlet Pressure (kPa)
liquid	188.74	11.53	saturation
liquid	179.25	10.88	saturation
liquid	170.66	10.30	saturation
liquid	161.95	9.74	saturation
liquid	151.59	9.12	saturation
liquid	143.01	8.64	saturation
liquid	128.98	7.89	saturation
liquid	119.80	7.44	saturation
liquid	112.43	7.08	saturation
liquid	98.73	6.44	saturation
liquid	91.25	6.15	saturation
liquid	79.53	5.65	saturation
liquid	70.84	5.38	saturation
liquid	59.84	5.09	saturation
liquid	49.02	4.90	saturation
liquid	43.52	4.81	saturation
0.094	201.55	38.10	saturation
0.104	183.87	31.87	saturation
0.107	157.01	24.68	saturation
0.102	141.74	19.95	saturation
0.103	122.54	16.08	saturation
0.104	105.21	13.15	saturation
0.094	82.95	9.08	saturation
0.102	71.95	7.94	saturation
0.094	60.75	6.80	saturation
0.106	52.08	6.07	saturation
0.198	178.28	53.74	saturation
0.202	159.08	43.06	saturation
0.200	142.57	33.53	saturation
0.203	120.54	23.60	saturation
0.225	105.60	20.73	saturation
0.204	78.60	11.87	saturation
0.204	71.58	10.51	saturation
0.205	63.07	8.98	saturation
0.202	51.44	7.53	saturation
0.311	153.65	62.79	saturation
0.300	137.45	46.76	saturation

Table A.5 (Continued)

Avg. Inlet x	Avg. G (kg/m^2-s)	Avg. Pressure Drop (kPa)	Inlet Pressure (kPa)
0.299	124.49	37.57	saturation
0.302	107.73	27.07	saturation
0.298	80.24	15.55	saturation
0.306	70.79	13.29	saturation
0.306	61.61	10.86	saturation
0.307	50.53	8.46	saturation
0.397	124.03	56.55	saturation
0.395	102.30	37.75	saturation
0.398	81.87	24.32	saturation
0.396	70.92	18.18	saturation
0.394	60.50	14.19	saturation
0.400	51.59	11.07	saturation
0.507	112.06	64.13	saturation
0.503	107.74	57.01	saturation
0.502	86.17	34.16	saturation
0.496	74.33	26.94	saturation
0.498	62.15	17.96	saturation
0.500	50.18	13.57	saturation
0.597	98.44	63.51	saturation
0.595	77.22	38.11	saturation
0.601	72.37	33.73	saturation
0.600	61.31	24.38	saturation
0.609	50.31	17.91	saturation
0.696	78.10	48.36	saturation
0.702	72.54	40.76	saturation
0.800	81.71	62.27	saturation
0.798	71.78	44.28	saturation
0.899	77.87	68.17	saturation
vapor	44.44	70.23	238.98
vapor	41.69	66.44	225.22
vapor	40.12	61.99	221.70
vapor	38.66	59.95	214.78
vapor	38.20	59.02	212.64
vapor	35.91	56.16	199.27
vapor	35.85	56.25	198.58
vapor	33.05	44.51	205.97
vapor	31.86	41.24	205.07

Table A.5 (Continued)

Avg. Inlet x	Avg. G (kg/m^2-s)	Avg. Pressure Drop (kPa)	Inlet Pressure (kPa)
vapor	28.69	38.00	183.71
vapor	28.26	35.65	187.75
vapor	26.48	32.29	182.53
vapor	24.96	26.75	190.40
vapor	23.97	23.39	196.88
vapor	20.74	18.82	184.94
vapor	19.78	17.01	184.16
vapor	18.79	14.26	193.87
vapor	18.43	13.81	194.87
vapor	16.34	11.49	181.26
vapor	15.28	10.28	176.35
vapor	10.39	8.54	106.54

Table A.6 2:1 Aspect Ratio Bumpy Plate Pressure Drop Data at 20^{o} C Inlet Temperature (Adiabatic, Upward Flow, R134a)

Avg. Inlet x	Avg. G (kg/m^2-s)	Avg. Pressure Drop (kPa)	Inlet Pressure (kPa)
liquid	302.02	20.71	saturation
liquid	280.51	18.55	saturation
liquid	252.05	15.92	saturation
liquid	224.25	13.61	saturation
liquid	201.60	11.89	saturation
liquid	191.67	11.20	saturation
liquid	182.13	10.55	saturation
liquid	168.34	9.68	saturation
liquid	158.30	9.10	saturation
liquid	149.51	8.61	saturation
liquid	139.17	8.09	saturation
liquid	129.87	7.64	saturation
liquid	121.32	7.24	saturation
liquid	102.43	6.42	saturation
liquid	89.16	5.94	saturation
liquid	78.17	5.53	saturation
liquid	66.91	5.16	saturation
liquid	62.37	5.10	saturation
liquid	52.10	4.87	saturation

Table A.6 (Continued)

Avg. Inlet x	Avg. G (kg/m^2-s)	Avg. Pressure Drop (kPa)	Inlet Pressure (kPa)
0.100	201.39	28.30	saturation
0.101	182.79	24.46	saturation
0.103	160.51	19.85	saturation
0.098	140.37	15.42	saturation
0.101	122.62	11.65	saturation
0.103	102.71	9.81	saturation
0.106	77.79	6.83	saturation
0.100	70.95	6.22	saturation
0.101	59.28	5.70	saturation
0.105	48.80	4.79	saturation
0.195	177.69	34.69	saturation
0.206	163.47	30.32	saturation
0.191	138.55	21.30	saturation
0.206	130.39	19.26	saturation
0.197	105.51	14.56	saturation
0.198	81.20	9.00	saturation
0.196	76.86	9.25	saturation
0.203	68.05	7.97	saturation
0.201	58.43	6.59	saturation
0.204	48.72	5.45	saturation
0.294	176.32	61.66	saturation
0.300	162.67	52.11	saturation
0.301	139.00	36.26	saturation
0.296	123.86	28.60	saturation
0.300	100.50	18.74	saturation
0.295	76.68	11.43	saturation
0.297	69.15	10.24	saturation
0.292	62.62	8.83	saturation
0.310	51.47	7.22	saturation
0.400	156.28	68.89	saturation
0.397	141.18	55.19	saturation
0.404	126.18	44.73	saturation
0.396	108.09	31.99	saturation
0.402	84.21	20.18	saturation
0.398	69.86	14.26	saturation
0.392	67.01	12.46	saturation
0.406	58.33	11.34	saturation
0.396	50.80	8.73	saturation

Table A.6 (Continued)

Avg. Inlet x	Avg. G (kg/m^2-s)	Avg. Pressure Drop (kPa)	Inlet Pressure (kPa)
0.497	138.15	69.92	saturation
0.494	126.97	57.46	saturation
0.504	107.24	41.83	saturation
0.507	80.31	23.64	saturation
0.511	71.21	19.15	saturation
0.506	62.35	15.06	saturation
0.498	52.94	10.91	saturation
0.597	118.78	69.13	saturation
0.595	99.86	46.66	saturation
0.602	84.16	32.60	saturation
0.595	70.90	23.28	saturation
0.600	62.17	18.60	saturation
0.602	53.44	14.58	saturation
0.689	108.62	68.46	saturation
0.699	102.02	62.60	saturation
0.694	81.90	39.70	saturation
0.699	70.12	29.90	saturation
0.689	62.51	23.68	saturation
0.693	51.48	16.30	saturation
0.801	97.88	66.93	saturation
0.809	83.93	49.75	saturation
0.809	72.96	37.75	saturation
0.802	64.64	29.85	saturation
0.901	88.73	61.99	saturation
0.904	84.25	56.32	saturation
0.914	72.20	42.99	saturation
vapor	69.61	69.31	464.85
vapor	63.67	56.58	470.74
vapor	57.53	45.09	477.26
vapor	50.09	39.45	425.19
vapor	46.85	35.66	414.34
vapor	44.27	31.83	416.99
vapor	41.84	24.65	466.20
vapor	37.57	20.33	456.43
vapor	35.31	22.45	381.87
vapor	32.39	18.75	383.00
vapor	29.67	15.68	384.28
vapor	27.15	13.45	377.87

Table A.6 (Continued)

Avg. Inlet x	Avg. G (kg/m^2-s)	Avg. Pressure Drop (kPa)	Inlet Pressure (kPa)
vapor	25.31	11.70	376.80
vapor	22.54	9.21	379.01
vapor	20.97	8.72	350.24
vapor	19.69	8.21	328.81

Appendix B

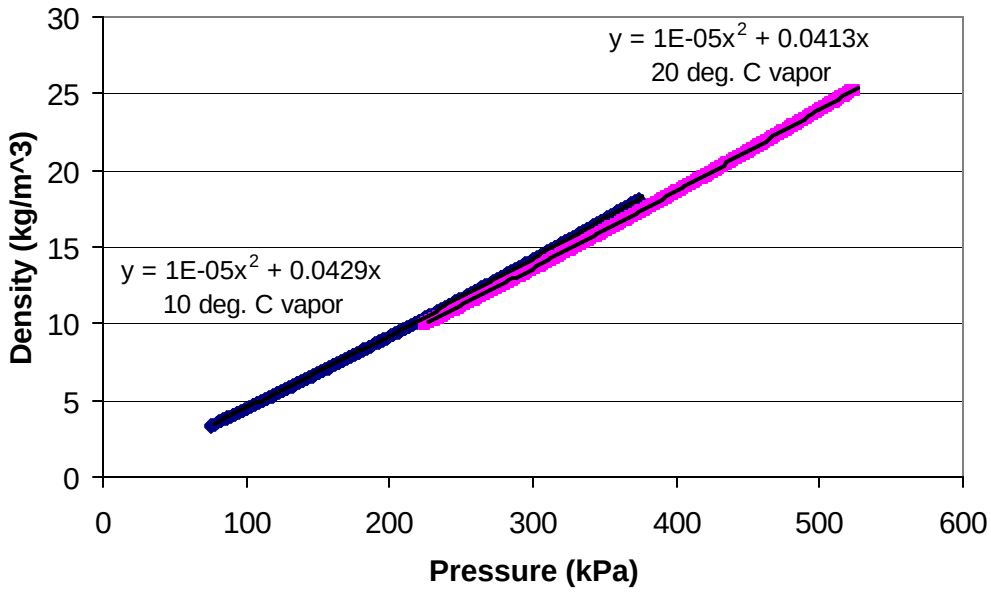

Figure B.1 Vapor Density Versus Pressure for R134a

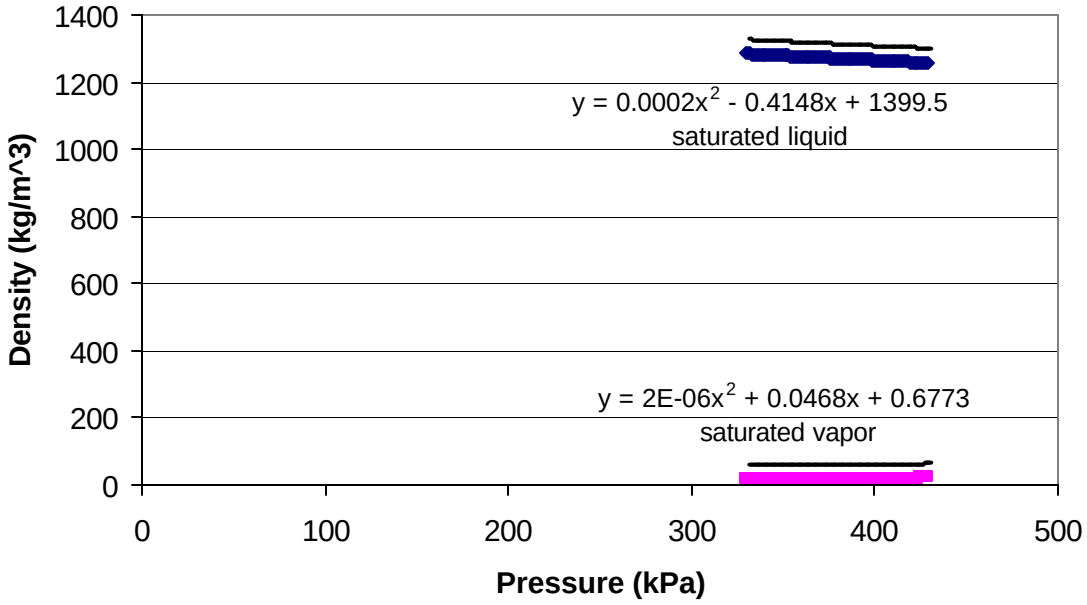

Figure B.2 Density Versus Pressure for R134a 10^{o} C Inlet Data

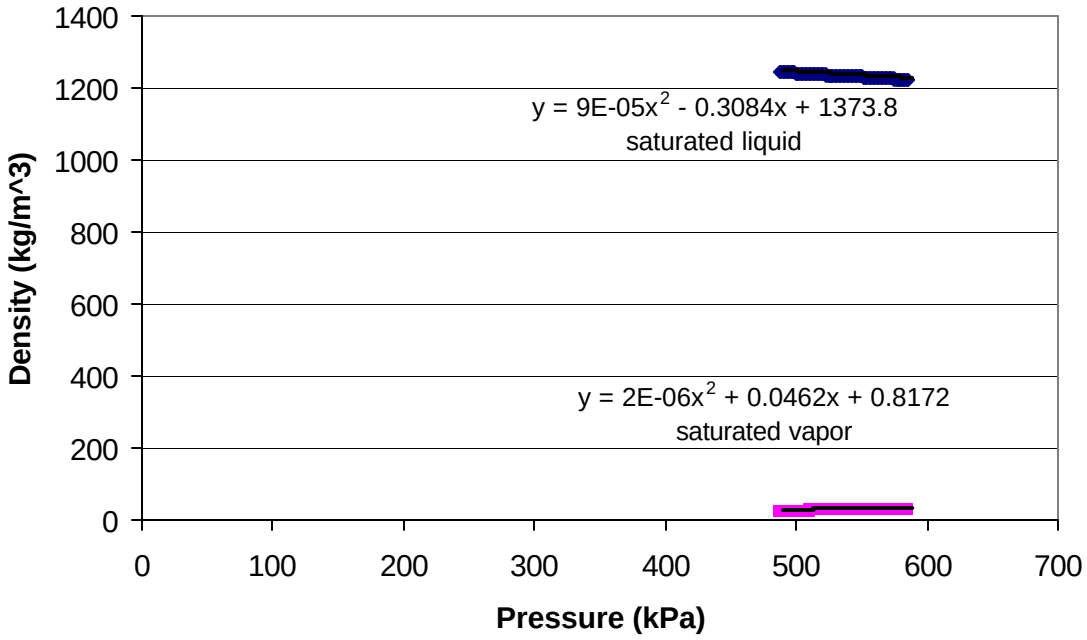

Figure B.3 Density Versus Pressure for R134a 20° C Inlet Data